Beyond General Relativity: New Structure and Stability Predictions from Modified Gravity and High-Density Interaction Models

by

Michael Gammon

A thesis
presented to the University of Waterloo
in fulfillment of the
thesis requirement for the degree of
Master of Science
in
Physics

Waterloo, Ontario, Canada, 2022

Author's Declaration

This thesis consists of material all of which I authored or co-authored: see Statement of Contributions included in the thesis. This is a true copy of the thesis, including any required final revisions, as accepted by my examiners.

I understand that my thesis may be made electronically available to the public.

Statement of Contributions

Much of the content in Section 1.2 was originally written as a project for PHYS 781 (to which Dr. Afshordi made valuable comments and suggestions).

The research presented in Chapter 2 has been published [1] in *Physical Review D* and was co-authored along with Chen Zhang and Robert Mann. Parts of my introduction to this subject in Chapter 1 are inspired by this work, and parts of Chapter 2 directly pull from a manuscript typed by Dr. Zhang.

The research presented in Chapter 3 was done under the supervision of Robert Mann. I was the main author of this content, to which Dr. Mann made invaluable contributions.

Abstract

In this thesis a number of topics are explored in an attempt to further understand gravitation and highly dense matter on a fundamental level. The notion of "quark stars" (QS), hypothetical compact stars composed of quark matter (QM), are introduced. We apply a novel, unified, interacting QM equation of state to the Einstein-Maxwell equations in an attempt to model the stellar structure of a quark star with non-negligible confining effects from the strong interaction, and a net charge. Paired with charge distribution models from the literature, we find some general trends in how charge and the strong interaction affect stellar structure of QS, and also identify a new exotic quark star which can have a finite mass & radius with zero centre pressure. The stability of these configurations is also examined, and we find that in general, maximum mass and stability points are no longer coincident on the mass-radius curves. Following this, we discuss higher curvature gravity theories (HCTs), in which stress-energy is in general proportional to a sum of powers of the curvature tensor. We work out slowly rotating black hole solutions to the new four dimensional Gauss-Bonnet scalar-tensor gravity theory, and investigate physical properties like horizon structure, innermost stable time-like orbits (which predict accretion disk structure), and null orbits (defining the photon sphere and black hole shadow). We find that this theory makes very similar predictions to general relativity in most regimes, but limits the allowed parameter space for black holes. The findings in both of these projects can in principle be used to constrain parameters of the theories against observation.

Acknowledgements

I would first like to acknowledge the contributions made to this project by Dr. Robert Mann and Dr. Chen Zhang, without whom this thesis wouldn't be possible. This research was supported in part by the Natural Sciences and Engineering Research Council of Canada, and has been granted an Ontario Graduate Scholarship (OGS) award.

I would like to acknowledge the contribution that my families (both biological and chosen) have made in their unwavering love and support. I would also like to recognize the way CJ Duck and Justice Chester influenced me creatively before their passing - invisible traces of it are scattered throughout this document, and everything else I do. Finally I'd like to thank my friends from the Sweetwater server, and our cats Bug & Larry for helping keep me sane through an incredibly challenging two years.

Dedication

dedicated to my parents

Table of Contents

List of Figures

Chapter 1

Introduction

In the early 1900s, physicist Albert Einstein presented a new relativistic theory of gravitation [2, 3, 4], which would eventually come to replace Isaac Newton's classical theory of gravity as the widely accepted model. General relativity (GR) proposes two things: that gravity, rather than being an instantaneous force between massive objects, is actually the curvature of a manifold we call spacetime, and that disturbances through spacetime travel at the speed of light. While most natural forces are described by fields *on* a spacetime, gravity is different in that it is fundamentally a feature of *spacetime itself* as energy induces curvature.

While Newton's theory worked very well in practical terrestrial cases (and accurately described most astronomical observations), there were small inconsistencies in the orbits of particular planets that could not be accounted for [5]. Einstein's new general theory of relativity successfully explained these inconsistencies, and suggested new observable phenomena such as the gravitational lensing of light [3], time dilation in the presence of strong gravitational fields [3], and gravitational waves [6] - all of which have since been confirmed experimentally [7, 8, 9]. The set of equations [4] governing the relationship between spacetime and stress-energy are:

$$G_{\mu\nu} = R_{\mu\nu} - \frac{1}{2}Rg_{\mu\nu} \tag{1.1}$$

$$G_{\mu\nu} + \Lambda g_{\mu\nu} = \kappa T_{\mu\nu} \tag{1.2}$$

where $G_{\mu\nu}$ is the Einstein curvature tensor, $g_{\mu\nu}$ is the metric tensor describing the geometry of spacetime, Λ is the cosmological constant, and $T_{\mu\nu}$ is the so-called stress-energy tensor. This set of expressions is among the most famous in all of science and mathematics - from these two elegant equations, a wellspring of astrophysical knowledge has emerged.

Following the first observations of highly energetic compact objects (such as quasars in the late 1950s, and pulsars in the late 1960s), it was necessary to invoke Einstein's theory to explain the structure and formation of highly dense stars which could potentially fit the data [10]. By the mid-1960s, our modern theories of gravitational collapse, compact stars, singularities and black holes were in development. Besides the incredible range and predictive power of GR, the theory is also infamous in regards to its beauty and elegance - "After one has learned the theory, one cannot help feeling that one has gained some deep insights into how nature works" [10]. While this thesis assumes the reader has a basic familiarity with the mathematical formalism and postulates of General Relativity, we use section 1.1 to review the fundamentals of particular branches of the theory that are relevant to the work done in this thesis. This includes a discussion of the Einstein-Hilbert action, a review some of the conceptually simplest black hole solutions, as well as a derivation of basic geodesic equations which are used to predict physical phenomena like the size of a black hole's accretion disk, or the geometry of its shadow.

As science continues to progress in a post-GR world, novel predictions are often born out of pushing the theory to its extreme limits or making interesting modifications and generalizations. The most extreme example of the former lies in the theory's prediction of its own demise on the smallest scales of nature (birthing the field of quantum gravity - even Einstein himself was already thinking about this in his first paper on gravitational waves! [6]). At slightly less extreme densities physicists have also mathematically modelled different kinds of astrophysical structures that could precede black holes. Following the discovery of the neutron in the early 1930s, physicists began speculating about the existence of neutron stars - an (at the time) hypothetical object more dense and compact than a white dwarf, containing mostly neutrons as constituent particles. Baade & Zwicky first proposed their existence in 1934 as a possible end stage for an old, massive star that undergoes a supernova explosion [11]. These authors suggested that neutrons produced on the surface of an ordinary star will fall towards the centre, since the radiation pressure on such particles will be negligible when compared to gravitational attraction. They thought this could imply an inner remnant of dense neutrons left behind after a supernova explosion. Later that decade, Oppenheimer and Volkoff (also Tolman, independently) derived the relativistic equations that describe the balance of forces and stellar structure in static, spherically symmetric stars [12, 13]. Those equations were used in the first theoretical predictions of the stability conditions and stellar structure of these hypothetical objects, and are the well-known Tolman–Oppenheimer–Volkoff (TOV) equations still widely used today.

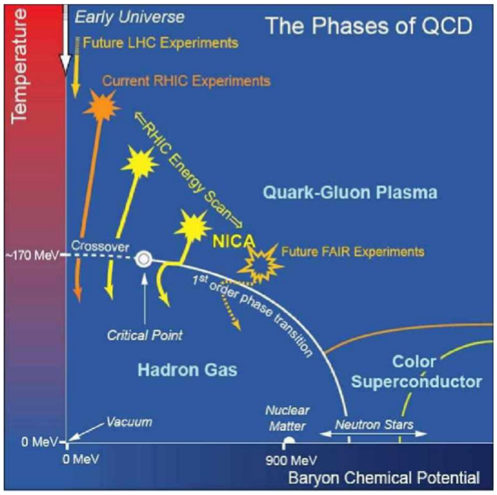

Figure 1.1: *"The phase diagram of strongly interacting QCD matter as it was presented in the USA NSAC Long range plan in autumn 2007 with the NICA domain added. Phase boundaries, critical endpoint, and conjectured dynamical trajectories for an expansion stage are plotted as well"* [14]. For reference, observed neutron stars typically have temperatures on the order of *keV* [15].

The original predictions on an upper limit of the mass of a neutron star made by Oppenheimer & Volkoff were quite low ($\sim 0.7 M_\odot$), largely due to the simple non-interacting matter equation of state (EOS) used in the calculations. Even at the time this was concerning, since this limit is lower than the Chandrasekhar mass limit for white dwarfs [16], and would prevent the formation of neutron stars out of ordinary stars. The fact that we have since observed neutron stars with masses greater than the so-called Oppenheimer-Volkoff mass limit is considered direct evidence of strong repulsive nuclear forces at such densities. We now know that accounting for the influence of nuclear forces in the EOS is crucial for an accurate description of these systems. While the community has not yet agreed upon the correct EOS for neutron stars, much observational and theoretical progress has been made. More current estimates for the upper mass limit for neutron stars are usually on the order of $\sim 2M_\odot$ [17, 18] when nuclear interaction and general relativistic effects are accounted for. It is interesting to note that beyond this upper limit it is assumed that gravitational collapse into a black hole will occur, although the lightest observed black hole (which was found last year! [19]) is still $\sim 3M_\odot$. In the mass range between (and slightly overlapping) the upper bound on neutron stars and the lower bound on observed black holes, hypothetical objects such as quark stars (QS) [1] have been postulated to exist. The overwhelming pressures relevant in these systems could cause nuclear particles to undergo a phase transition into a quark-based form of matter, although to date no quark stars have been observed.

In general we lack an empirical understanding of cold matter at densities higher than nuclear [20], conditions that can't be recreated in laboratories on Earth. The NICA and FAIR experiments look to probe densities in this regime at extremely high temperatures (see figure 1.1), but the heaviest compact stellar objects are significantly cooler, a region of parameter space that is still very much a mystery. Instead, theorizing what stars composed of such matter would look like - their stellar structure, stability, typical charge/mass, etc. could provide astronomers with observational "tip-offs" to look for when interpreting data. Observation of an exotic quark matter star (should one exist) would allow us to indirectly probe the behaviour of bulk systems composed of this new phase of matter on timescales much longer than those relevant to collisions [21] - something virtually unachievable in a terrestrial setting. Unfortunately this exciting feature is also the greatest difficulty when forming such theories. Without access to empirical information as a sanity-check on calculations, the parameters of the theory (namely the strong interaction model and interaction strength) must be chosen with extreme care.

The latter point of interest – interesting modifications and generalizations – is a large and interesting theoretical field, partially motivated by GR's singularity problem (ie. geodesic incompleteness), coupled with the fact that the base theory is incredibly successful to begin with. Early attempts of this can be seen in the writings of Weyl [22] or Eddington [23], and this search continues through to present day. A common class of generalizations to General Relativity are referred to as higher curvature theories (HCTs), in which we assume that a sum of powers of the curvature tensor will be proportional to stress-energy. Although the differential equations hidden within equation (1.2) are highly non-linear in terms of the metric, the relation between spacetime curvature and energy in GR *is* assumed to be linear. Logically this linear relationship is not required, and it is conceivable that the empirical success of Einstein's theory could be improved upon by modifying the left-hand-side of this equation to contain a sum of powers of the curvature tensor.

These HCTs play important roles in many different areas of physics - they appear in many proposals for quantum gravity [24] and may be necessary to account for observational evidence of dark matter, early-time inflation, or late-time acceleration [25]. Lovelock theories [26] are the best-known examples of HCTs. However, until recently, their equations only had non-trivial solutions in spacetime dimensions larger than 4 [27] (ie. not the world we live in), so their physical significance had been unclear. Recently, a new class of HCTs have been proposed that do allow for higher-order gravity in four dimensions and satisfy reasonable physical requirements such as positive energy excitations on constant curvature backgrounds. Such higher curvature theories are referred to as "generalized quasi-topological gravities", or GQTGs [27]. The original HCT was cubic in curvature [26, 28]; it was soon followed by a class quartic in curvature [24]. Most recently a procedure was found for constructing physically reasonable HCTs to any desired power of curvature [27].

Amidst uncountable higher curvature gravity theories, the quadratic Lovelock, or so-called "Einstein-Gauss-Bonnet" theory has been considered with special interest thanks to features like 2nd order equations of motion and adherence to appropriate symmetry and conservation properties. For a long time it was thought that the Gauss-Bonnet (GB) action term could not contribute to a system's gravitational dynamics in $D \leq 4$ (since it becomes a total derivative in such cases), and hence the GB contribution is often referred to as a "topological term" of no relevance. Furthermore, a new 3+1-dimensional gravity theory which possesses diffeomorphism invariance, metricity, and second order equations of motion would be a violation of the Lovelock theorem [26] and thus should only be possible by introducing an additional field into the theory besides the metric tensor.

In 2020, Glavan & Lin [29] claimed to have bypassed the Lovelock theorem via the following re-scaling of the Gauss-Bonnet coupling constant:

$$(D-4)\alpha \to \alpha, \tag{1.3}$$

and then considering the $D \to 4$ limit of exact solutions to Einstein-Gauss-Bonnet gravity. This approach allowed for non-vanishing contributions from the GB action term in $D = 4$. In doing so, a number of 4-dimensional metrics can be obtained (for spherical black holes [29, 30, 31, 32, 33], cosmological solutions [29, 34, 35], star-like solutions [36, 37], radiating solutions [38], collapsing solutions [39], etc.) carrying imprints of higher curvature corrections inherited from their $D > 4$ counterparts.

Unfortunately the existence of limiting solutions does not actually imply the existence of a 4D theory, and a number of objections in this vein quickly appeared [40, 41, 42]. However, the conclusion that there ultimately was no four-dimensional Gauss-Bonnet theory of gravity proved to be premature when it was shown that a $D \to 4$ limit of the action (1.3) could be taken [43, 44], generalizing a previous procedure for taking the $D \to 2$ limit of GR [45]. It is also possible to employ a Kaluza-Klein-like procedure [46], compactifying D-dimensional Gauss-Bonnet gravity on a $(D-4)$-dimensional maximally symmetric space and then re-scaling the coupling constant according to equation (1.3). The resulting 4D scalar-tensor theory is a special case of the Horndeski theory [47], which surprisingly has spherical black hole solutions whose metric functions match those from the naïve $D \to 4$ limiting solutions derived by Glavan & Lin [29]. Such solutions can be obtained without ever referencing a higher dimensional spacetime [43].

This theory, referred to as 4D Gauss-Bonnet gravity, provides an interesting phenomenological competitor to GR [48]. Despite much exploration of the theory [49], there has been relatively little work investigating rotating black hole solutions. Attempts have been made using the naïve re-scaling of the 4DGB coupling constant [50] or a Newman-Janis approach [32, 51, 52], neither of which produce valid solutions to this theory in general (the latter case not satisfying the positive energy condition). In [37] an analytic form of the slowly rotating metric function $p(r)$ was derived for the scalar-tensor 4DGB theory in asymptotically flat spacetime, but a detailed study of the geodesics of particles surrounding such black holes (particularly in de Sitter and anti-de Sitter spacetimes) has yet to be completed.

In the rest of this thesis we will outline the methods used and results obtained from two separate projects which stand on the shoulders of GR - the first of which looks at the structure and stability of extremely compact, charged "quark" stars governed by Einstein's field equations coupled with a modern, interacting equation of state. The second project delves into the aforementioned rotating black hole solutions in the novel 4D scalar-tensor Gauss-Bonnet theory of gravity. The goal of this work is to search for new physics near the limits of Einstein's famous theory, and make new astrophysical predictions which in principle could help constrain the parameters of our current nuclear interaction models or the coupling strength of the 4DGB action term.

In chapter 1.1 we provide a review of the basic theory and predictions of General Relativity, starting from the Einstein-Hilbert action (and omitting the mathematical preliminaries, as it is assumed the reader already has a basic understanding of these). Following this, we delve into the simplest black hole solutions to Einstein's theory as a way to motivate some of the decisions made later in this thesis (such as choosing metric function solutions to the 4DGB theory which agree with those from static Einsteinian black holes in the appropriate limits). We conclude this section with an overview of the geodesic equations, and discuss the physical implications of such solutions such as the innermost stable orbits for massive particles (related to accretion disk size), the location of the photon ring, and the geometry of the black hole shadow.

In chapter 1.2 we outline the basic arguments for the absence of net charge in classical stars, and generalize some of these arguments to work within the relativistic framework of compact stars. We also discuss the discrepancy between the local (Newtonian) balancing of forces on a charged particle and the solutions to the global relativistic structure equations. In the literature authors often point to this discrepancy as evidence that charged compact stars are simply an intermediate state between classical stars and black holes. We probe this idea further and question whether current observed mass-radius pairs would be consistent with a charged neutron star if they were re-derived without the assumption of zero net charge.

In chapter 1.3 we introduce the idea of a new high-density form of baryonic matter - "quark matter" (QM). If such a state is indeed possible at relatively low temperatures, we hypothesize the existence of exotic "quark stars" (QS) where some or all of the constituent mass is described in terms of deconfined quark degrees of freedom. Due to the attractive nature of the strong interaction, such objects could potentially hold net charge more stably than neutron stars, making the existence of charged quark stars an interesting open question. With this, we outline the structure equations for a massive body with a net charge (ie. the charged TOV equations [13, 12]), and a unified interacting equation of state that includes effects from perturbative QCD and colour superconductivity. The stellar stability equations are also written down. All equations in this section are then cast in dimensionless form, so the stellar structure and stability are easily studied independent of empirical parameters.

In chapter 1.4 we introduce the idea of modified/higher curvature gravity theories and their basic history. Starting from Lovelock's theorem, we discuss how the Einstein-Hilbert action leads to the most general equations of motion in four dimensions (which meet Lovelock's four requirements) unless additional fields besides the metric are introduced. This strongly motivates the introduction of a 4D scalar-tensor version of the Gauss-Bonnet gravity theory, derived by Hennigar et al. in 2020 [43].

Finally, in chapters 2 & 3 we share the methods and results of two relevant research projects completed during this thesis. The former examines the stellar structure and stability of charged interacting quark stars, while the latter finds slowly rotating black hole solutions in four dimensional Gauss-Bonnet gravity.

1.1 Formalism of General Relativity

While the goal of this thesis is not to give a complete mathematical primer for general relativity, for completeness we will briefly introduce the objects from Riemannian geometry which are used in this thesis. We adopt the sign conventions of Carroll (2003) [53] $(-,+,+,+)$, and work in natural units ($G = c = 1$) unless stated otherwise. The geometric and causal structure of spacetime is described by the metric tensor $g_{\mu\nu}$, and ds^2

denotes the line element corresponding to the metric. ∇ represents the affine connection, also known as the covariant derivative when applied to a tensor. The Riemann curvature tensor represents tidal forces on a rigid body along a geodesic, and in a coordinate basis it can be written as

$$R^{\rho}{}_{\sigma\mu\nu} = \partial_\mu \Gamma^{\rho}_{\nu\sigma} - \partial_\nu \Gamma^{\rho}_{\mu\sigma} + \Gamma^{\rho}_{\mu\lambda}\Gamma^{\lambda}_{\nu\sigma} - \Gamma^{\rho}_{\nu\lambda}\Gamma^{\lambda}_{\mu\sigma} \tag{1.4}$$

where

$$\Gamma^{\sigma}_{\mu\nu} = \frac{1}{2} g^{\sigma\rho} \left(\frac{\partial g_{\rho\mu}}{\partial x^\nu} + \frac{\partial g_{\rho\nu}}{\partial x^\mu} - \frac{\partial g_{\mu\nu}}{\partial x^\rho} \right) = \frac{1}{2} g^{\sigma\rho} \left(g_{\rho\mu,\nu} + g_{\rho\nu,k\mu} - g_{\mu\nu,\rho} \right) \tag{1.5}$$

are the Christoffel symbols, with commas on the rightmost side of equation (1.5) representing partial derivatives (and in general, semicolons representing covariant derivatives/vertical bars represent divergences). The Ricci tensor (appearing in equation (1.1)) is a symmetric 2-tensor field which can be calculated from the Riemann tensor as follows:

$$R_{\mu\nu} = R_{\sigma\mu\nu}{}^{\sigma}. \tag{1.6}$$

The Weyl curvature tensor is an object similar to the Riemann tensor in that it also describes tidal forces acting on a body along geodesics. It is defined as the trace-free part of the Riemann tensor, ie:

$$C_{\mu\nu\rho\sigma} := R_{\mu\nu\rho\sigma} - \frac{2}{D-2} \left(g_{\mu[\rho} R_{\sigma]\nu} - g_{\nu[\rho} R_{\sigma]\mu} \right) + \frac{2}{(D-1)(D-2)} R g_{\mu[\rho} g_{\sigma]\nu} \tag{1.7}$$

(where square and round brackets denote antisymmetric and symmetric tensor parts, respectively) and is defined such that every contraction between indices gives zero. The simplest curvature invariant of a Riemannian manifold is the Ricci scalar (or scalar curvature), which assigns a real number to each point on the manifold relating to its intrinsic geometry at that point. In GR this is also the Lagrangian density for the Einstein-Hilbert action (see section 1.1.1), and is defined as the trace of the Ricci tensor with respect to the metric:

$$R = g^{\mu\nu} R_{\mu\nu}. \tag{1.8}$$

Finally, we define the Kretschmann scalar K, which is often useful for determining whether metric singularities are real or follow from the choice of coordinates. In principle the scalar curvature can also be used for this purpose, although for vacuum solutions $R_{\mu\nu}$ is trivially zero everywhere. In terms of the Riemann tensor:

$$K = R_{\mu\nu\sigma\rho} R^{\mu\nu\sigma\rho}. \tag{1.9}$$

1.1.1 The Einstein-Hilbert Action and Gravitational Field Equations

One way of arriving at Einstein's field equations (eqs. (1.1) and (1.2)) is via a Langrangian formulation through the principle of least action. In the case of standard general relativity, this process begins by considering how the Einstein-Hilbert (EH) action reacts to small variations of the metric. The EH action is written [53]:

$$S_{EH} = \int \sqrt{-g} R \, d^D x \tag{1.10}$$

in vacuum, where $D = 4$ is the action corresponding to four dimensional spacetime. If the non-vacuum field equations are desired, we instead consider an action of the form

$$S = \frac{1}{16\pi} S_{EH} + S_M \tag{1.11}$$

where the gravitational action term now has a normalization factor preceding it (keeping in mind our choice of natural units), and the second term is the action for matter fields. Variation of this second action yields the complete Einstein equation [53], namely

$$R_{\mu\nu} - \frac{1}{2} R g_{\mu\nu} = 8\pi T_{\mu\nu} \tag{1.12}$$

where again $T_{\mu\nu}$ is the energy momentum tensor, which can be set to zero in vacuum.

The field equations in this form suggested a non-static universe, which troubled Einstein. To remedy this he considered the inclusion of a "cosmological constant" Λ which would permit (unstable) steady-state solutions by counterbalancing gravitation [54]:

$$R_{\mu\nu} - \frac{1}{2} R g_{\mu\nu} + \Lambda g_{\mu\nu} = 8\pi G T_{\mu\nu}. \tag{1.13}$$

After Hubble published evidence of cosmological expansion in 1929 [55], Einstein famously retracted the constant, calling it "the biggest blunder in [his] career". However, cosmological data [56] continues to imply that our universe really does have a small positive cosmological constant, just not for the reason that Einstein had thought. This effectively gives the vacuum an intrinsic energy density and pressure - a positive cosmological constant Λ could propel the accelerated expansion of the universe that we observe. Unfortunately there are still major gaps in our understanding of inflationary cosmology - most quantum field theories predict a cosmological constant much larger (by as much as 120 orders of magnitude [57]) than the observed vacuum energy density. This has been referred to as "the worst theoretical prediction in the history of physics" [58]. It seems unlikely that this problem will be rectified until we reach a fully developed theory of quantum gravity.

Before moving on, it is worth mentioning for completeness that in general the "Gibbons-Hawking-York" boundary term [59] should also be added to the Einstein-Hilbert action if the underlying spacetime manifold being described possesses a boundary. If the non-boundary action term is simply the EH action on its own then the same field equations will follow whether the boundary term is considered or not, but for more general actions this is not necessarily the case. With the boundary term included, the gravitational action takes the form

$$S = \frac{1}{16\pi}\left[\int_{\mathcal{M}} \sqrt{-g}R\ d^Dx + \int_{\partial\mathcal{M}} \sqrt{-h}B\ d^3x\right] + S_M \tag{1.14}$$

where $B = 2K$ is a "surface term" chosen to extremize the action under variations of the metric which vanish on the manifold's boundary (but may have non-zero normal derivatives), and h is the induced (through a pullback) metric on the boundary $\partial\mathcal{M}$ [59]. More concretely, the constant K contained within B is the trace of the extrinsic curvature of the boundary (ie. $K = h^{\mu\nu}K_{\mu\nu}$ where $K_{\mu\nu} = \nabla_\mu \xi_\nu$ and ξ^μ is the unit tangent field of the congruence of timelike geodesics orthogonal to the boundary [10]).

1.1.2 Static and Slowly Rotating Schwarzschild Solutions

Spherically symmetric solutions to eq. (1.12) are of particular interest to astrophysicists, both due to their simplicity and their relevance to practical problems such as the gravitational field surrounding a static black hole or (to a good approximation) a star like our Sun. Moreover, exterior (empty space) solutions are typically the first priority since these regions are easier to observe directly. In 1916 (just a month after the publication of general relativity [4]), Karl Schwarzschild published [60] the first non-trivial exact solution to Einstein's equations (also found independently by Droste around the same time [61]), derived while serving in the German army during World War I. Schwarzschild died on the Russian front less than six months after publication.

Schwarzschild's solution describes the gravitational field surrounding a point-like, non-rotating, uncharged spherical mass. According to Birkhoff's theorem [62], it is the most general spherically symmetric vacuum solution to the field equations. In spherical coordinates the Schwarzschild solution takes the form

$$ds^2 = -f(r)dt^2 + \frac{1}{f(r)}dr^2 + r^2(d\theta^2 + \sin^2\theta d\phi^2) \tag{1.15}$$

where

$$f(r) = \left(1 - \frac{r_s}{r}\right) \tag{1.16}$$

and $r_s = 2M$ is the Schwarzschild radius which lies at the black hole event horizon.

Following Schwarzschild, more exact solutions were derived including the Reissner–Nordström solution [63, 64, 65, 66] for a static, spherically symmetric body with a net charge, and the Kerr solution [67] for an uncharged, rotating, axially-symmetric black hole. In general, the line element corresponding to the Kerr metric can be written [53]:

$$\begin{aligned} ds^2 = &-\left(1 - \frac{2Mr}{\rho^2}\right)\mathrm{d}t^2 - \frac{2Mar\sin^2\theta}{\rho^2}(\ \mathrm{d}t\ \mathrm{d}\phi + \mathrm{d}\phi\mathrm{d}t) \\ &+ \frac{\rho^2}{\Delta}\mathrm{d}r^2 + \rho^2\ \mathrm{d}\theta^2 + \frac{\sin^2\theta}{\rho^2}\left[\left(r^2 + a^2\right)^2 - a^2\Delta\sin^2\theta\right]\mathrm{d}\phi^2 \end{aligned} \tag{1.17}$$

where

$$\Delta(r) = r^2 - 2Mr + a^2 \tag{1.18}$$

and

$$\rho^2(r,\theta) = r^2 + a^2\cos^2\theta, \tag{1.19}$$

with a being a parameter that governs the rotation rate via $a = J/M$ (angular momentum per unit mass). Even to the untrained eye it is clear that this metric is complicated, and is indeed more difficult to work with in general. Because of this, it is often advantageous to rewrite this metric up to linear order in a, with higher order contributions suppressed. In doing so we find

$$ds^2 = -f(r)dt^2 + \frac{dr^2}{f(r)} + 2ar^2p(r)\sin^2\theta dtd\phi + r^2\left[d\theta^2 + \sin^2\theta d\phi^2\right] \tag{1.20}$$

corresponding to a slowly rotating black hole, where the $dtd\phi$ term in the metric and the Schwarzschild metric function $\left(1 - \frac{r_s}{r}\right)$ have respectively been replaced with generic functions $r^2p(r)$ and $f(r)$, both of which depend on some underlying assumptions about the spacetime.

The metric (1.20) provides us with an ansatz for finding slowly rotating black hole solutions in more general theories of gravity. In chapter 3 we consider such a slowly rotating black hole under a modified gravity theory, and this generality becomes important.

1.1.3 Predicting Physical Properties from Metric Functions and Geodesics

Solutions to the gravitational field and geodesic equations can offer a plethora of information regarding physical properties in the region surrounding a gravitational body. In this section we discuss some examples of this in the context of the Schwarzschild black hole solution from equation (1.15).

The location of the black hole event horizon surrounding a point mass occurs at the radius for which the dr^2 component of the metric (1.15) diverges. For a Schwarzschild-like metric ansatz (such as (1.20)), this is equivalent to finding the radius at which $f(r) = 0$. From equation (1.16), it is clear then that r_s represents the event horizon radius r_h where $f(r_h) = 0$.

Since black holes have a non-zero angular momentum in general, we can simply define the angular velocity of the event horizon [68] as

$$\Omega_h = -\frac{g_{t\phi}}{g_{\phi\phi}}|_{r=r_h} = -ap(r_h), \tag{1.21}$$

which clearly vanishes for the non-rotating Schwarzschild black hole.

Besides the horizon's location and angular velocity, we would also like to know the behaviour of particles on time-like and light-like geodesics in the area surrounding the black hole. These geodesics will tell us about the shape and size of the black hole's accretion disk and photon ring (respectively), which gives us some footing on which to test a theory of gravity against observation. We first make use of the fact that for a non-rotating black hole $E = f(r)\dot{t}$ and $j = r^2\dot{\phi}$ are constants of motion along the geodesics, thanks to the static and rotational Killing fields (respectively) [10]. In doing so one can derive an "effective potential" surrounding the Schwarzschild black hole, which looks like

$$V_{\text{eff}} = \frac{1}{2}\left(\frac{j^2}{r^2} + \xi\right) f(r) - \frac{1}{2}E^2 \tag{1.22}$$

where

$$\xi = \begin{cases} 1 & \text{(time-like geodesics)} \\ 0 & \text{(null geodesics).} \end{cases} \tag{1.23}$$

This simplifies the problem by reducing it back to a classical particle in a potential. For massive particles, the main quantity of interest is the innermost stable circular orbit (or ISCO). The two conditions for the existence of circular geodesics are

$$V_{\text{eff}}(r) = 0 \qquad V'_{\text{eff}}(r) = 0 \tag{1.24}$$

while the sign of $V''_{\text{eff}}(r)$ dictates the stability of such orbits. Stable orbits are described by $V''_{\text{eff}}(r) > 0$, while $V''_{\text{eff}}(r) < 0$ indicates instability. Since we are interested specifically in the *innermost* stable circular orbit, we shall require $V''_{\text{eff}}(r) = 0$. The radius at which these three relations hold will be the inner radius of the black hole accretion disk.

For massless particles, orbital instability is a given. We are interested in locating the radius at which photons have unstable *circular* orbits, dictated via

$$V_{\text{eff}}(r) = 0 \qquad V'_{\text{eff}}(r) = 0. \tag{1.25}$$

Stability analysis of the photon ring is typically carried out afterwards, via the calculation of Lyapunov exponents for the null geodesic orbits [68].

1.2 Net Charge in Astrophysical Bodies

In this section we review the basic arguments regarding whether astrophysical bodies (namely classical and compact stars) should possess a net charge or not. Furthermore, we repeat some calculations from the literature (along with a few original calculations) to argue what the expected charge-to-mass ratio in these bodies should be.

1.2.1 Charge-to-Mass Ratio for Non-Compact Stars

Traditionally, non-compact stars are assumed to be nearly charge-neutral. The basic argument for neutrality states that there must exist some maximum net charge that a gravitationally bound body can contain before similarly-charged particles from the interstellar medium (ISM) will be overwhelmed by the repulsive Coulomb force and will thus be repelled, unable to further add to the star's net charge. For a positively charged star, one would expect this condition to be met when the electrostatic force on a proton at the surface of the star is approximately balanced by the gravitational force at that same point [16], ie:

$$\frac{Qek_e}{R^2} = \frac{GMm_p}{R^2} \tag{1.26}$$

where Q is the net charge of the star, e is the elementary charge of a proton, k_e is the Coulomb constant, M is the mass of the star, m_p is the mass of the proton, and R is the star's radius.

The calculation can be trivially repeated for a negatively charged star repelling an electron. It is easy to see that the above expression can be rearranged to give a classical upper bound on the charge to mass ratio of a Newtonian star:

$$\frac{Q}{M} = \frac{Gm_p}{ek_e} \approx 7.75 \times 10^{-29} \frac{C}{kg} \approx 150 \frac{C}{M_\odot} \tag{1.27}$$

which is usually written as 100 C for a 1 $M_\odot$ star in the literature [69, 70, 71]. This relation explains what is meant by charge neutrality in astrophysics - it's not that $Q = 0$ exactly, but rather that the charge to mass ratio is very small – too small to have an appreciable effect on stellar structure. This approach is conceptually useful due to its simplicity, although it does not tell us much about how such a star obtains a net charge in the first place.

Alternatively, we can view this problem through the lens of electron trapping. In 1924 [72], Svein Rosseland wrote a paper on the electrical state of stars in which they are modelled as spheres of hot, ionized gas. It had been argued prior to his publication that a star that is constructed of strongly ionized matter could be expected to hold a net positive electric volume charge. This comes as a consequence of assuming that the lighter particles (electrons) would rise to the surface of the star due to a difference in partial pressure between the electrons and ions (largely thermal pressure in the case of a non-compact star). Some of these electrons are expected to float up with a velocity greater than the star's escape velocity, ejecting into the ISM. This process is expected to continue until the electric field created via charge separation is strong enough to prevent further escape, and

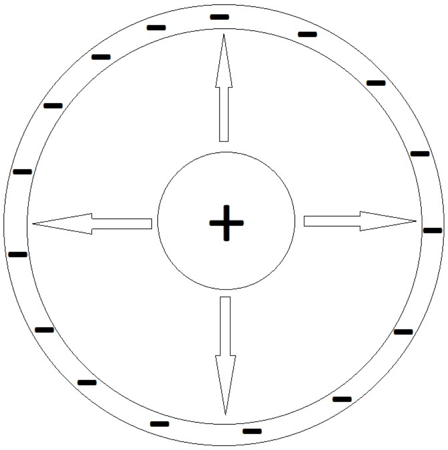

Figure 1.2: Due to a difference in partial pressure, electrons tend to float to the surface of a non-compact star and out into the ISM until the induced electric field (arrows in this diagram) is strong enough to counterbalance gravity at the surface. What is left is a star with a small net charge, an internal electric field, and a negatively charged atmosphere surrounding it.

an equilibrium configuration is attained (see figure 1.2).

Ray et al. [69] claimed that this equilibrium condition would occur when the electrostatic energy of an electron near the star's surface is on the order of its thermal energy. They found that for a star like the sun this again gives an expected charge to mass ratio of $\frac{Q}{M} \sim 100\frac{C}{M_\odot}$. More concretely, the star's gravitational energy would also be contributing to this equilibrium, ie:

$$k_B T = k_e \frac{eQ}{R} + G\frac{Mm_e}{R} \tag{1.28}$$

or, equivalently,

$$\frac{Q}{M} = \frac{1}{k_e e}(\frac{R}{M}k_B T - Gm_e). \tag{1.29}$$

When written this way it is clear that the second term (gravitational effects) will be negligible due to the small mass of the electron. Nevertheless, we compute this ratio exactly for our own sun ($R_\odot = 6.95 \times 10^8$ m, $T_\odot = 1.57 \times 10^7$ K [73]) and find that once again

$$\frac{Q}{M} \approx 100\frac{C}{M_\odot}. \tag{1.30}$$

To calculate this we follow the lead of Ray et al. [69, 70, 74] by using the sun's core temperature in the thermal energy, since the kinetic energy of such electrons are mostly a product of this higher inner temperature. Interestingly, estimating $\frac{Q}{M}$ this way matches our previous result (which was calculated for the repulsion of like charges) almost exactly.

1.2.2 Stability of Charged Non-Compact Stars

In this section we briefly discuss the stability of net charge in a classical star. Following charge ejection (see section 1.2.1), one would expect the star to be surrounded by an atmosphere which holds a slight negative charge [75]. In fact, Bally & Harrison argue that all self-gravitating systems with size greater than the Debye length will take on a slight positive charge, surrounding themselves with a negatively charged atmosphere. They call this idea the "Electrically Polarized Universe". Naïvely one might think that this configuration is highly unstable and that free negative charges from the atmosphere will quickly fall back into the star. On the contrary, since the outer surface of the star is dense with electrons, nearby electrons tend to scatter off of this surface potential rather than fall into the star (unless the approach velocity is above some threshold). To illustrate, recall the 1D case of a point charge being attracted by a large positive charge, with a smaller negative charge separating the two (see figure 1.3a), where the total electric field experienced by the test particle on the right hand side of the diagram is the sum of the fields produced by the positive charge Q1 and the negative charge Q2.

It is straightforward then to plot the electric field experienced by this test particle as a function of the distance r between the smaller negative charge and the test particle. For this simple demonstrative calculation we have set $r_q = 10$ and $\frac{Q_1}{Q_2} = -200$, and the results can be seen in figures 1.3b and 1.4. It is clear by looking at this plot that in the 1D case an incoming electron will initially be attracted by the net positive charge, but then will scatter off the small negatively charged particle unless it approaches with a sufficiently high energy to penetrate the electron potential. Of course this 1D model is an oversimplification of the general case (where we have a positively charged sphere embedded inside a negatively charged spherical shell), but due to spherical symmetry the physics works out identically. If we think of Q2 as the 1D analogue of an electron shell, we also see why the atmosphere surrounding the star will remain negatively charged. Just outside the thin scattering potential of the negative shell, there is a well of positive potential that will attract negatively charged particles into the region where they will stay indefinitely.

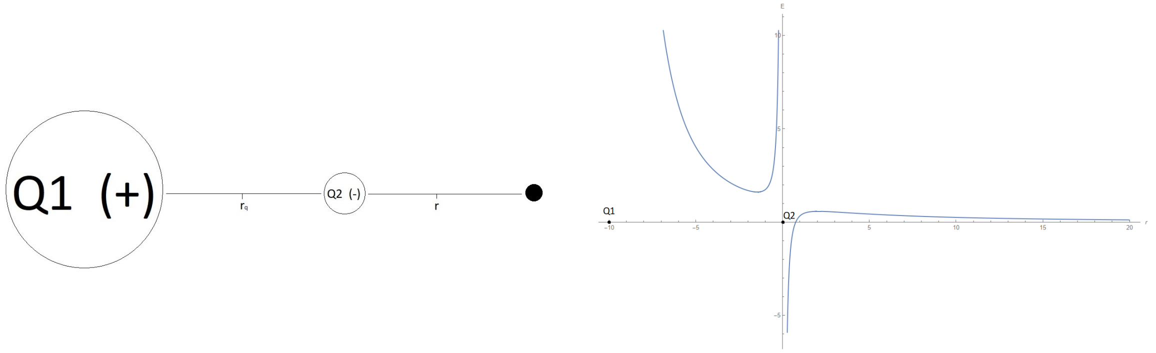

(a) The total electric field experienced by the test particle on the right is the sum of the fields produced by Q1 and Q2.

(b) Electric field experienced by the black test particle, as a function of its distance from Q2.

Figure 1.3: 1D charge screening analog.

1.2.3 Generalization of Arguments for Compact Stars

Relativistic Considerations

So far we have made all arguments under the assumption that a classical balancing of forces is an appropriate treatment for describing the interior of a star. For non-compact stars this is likely true to a good approximation, but when thinking about extremely dense objects like neutron stars or quark stars can we assume that spacetime will be flat over the object's radius? If not, the equations of motion must be solved simultaneously alongside the fully coupled problem of gravity. It turns out that in an average neutron star, the spacetime curvature is small enough to solve the matter equations for nuclear/particle physics in flat spacetime, but not the global equations for stellar structure. More specifically, the metric $g_{\mu\nu}$ changes by a factor of 2.5 over a typical neutron star's radius, which corresponds to a relative change of 10^{-19} over the spacing of nucleons in the star [16]. The general relativistic structure equations used in such cases are the well-known Tolman–Oppenheimer–Volkoff (TOV) equations [12, 13], first derived in 1939 to constrain the structure of a spherically symmetric body of isotropic material in static gravitational equilibrium. In these regimes it becomes non-trivial to disentangle the effects of the electrostatic force and gravity only on the charged particles since these forces are coupled to one another "in every respect" [71].

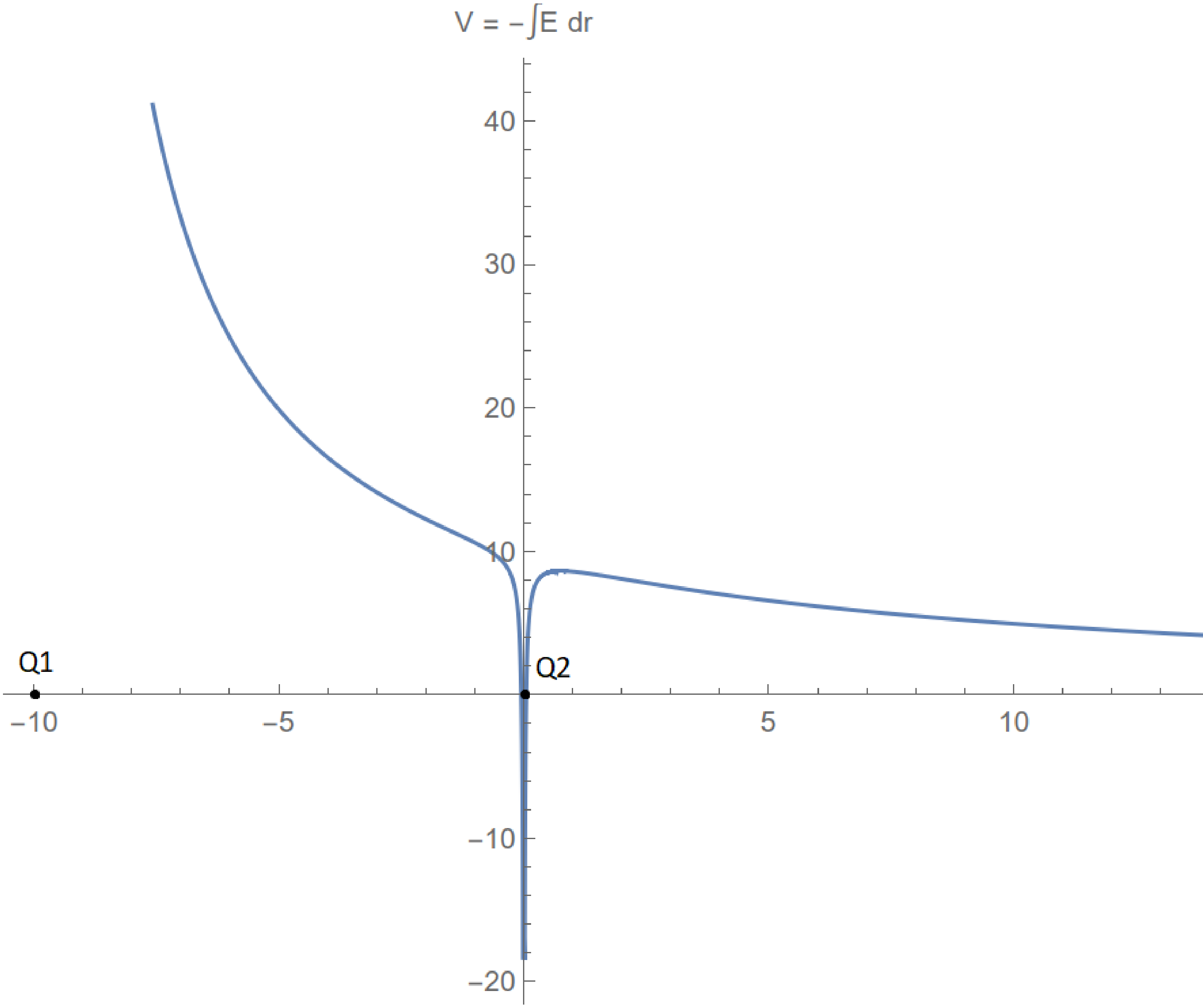

Figure 1.4: Electric potential as a function of distance from Q1.

Charge Density Proportional to Mass Density

In their 2003 paper [69], Ray et al. solved the modified (for charge) TOV equations for a neutron star with a polytropic equation of state $P = \kappa\rho^{1+1/n}$ (where the polytropic index $n = 1.5$ and $\kappa = 0.05fm^{8/3}$). The polytropic Equation of State (EOS) is used because it is "a more general approach than considering any model dependent EOS" [69]. One might notice that this EOS does not include any dependence on electromagnetic contributions. This is because the charge-to-mass ratio of the contributing particles is very large, and thus the number density of charged particles is extremely small compared to neutral particles. The authors claimed that any effect brought about by these extra charged particles should be negligible, and a charge-neutral EOS should still be valid to a good approximation.

Trapped protons were taken to be the charge carriers in the star, assuming a charge distribution model in which charge density ρ_e is proportional to mass density ρ:

$$\rho_e = f \times \epsilon \tag{1.31}$$

where $\epsilon = \rho c^2$ which is in units of $[MeV/fm^3]$. With this, f has units of $\frac{1}{[km]}[fm^3/MeV]^{1/2}$ and ρ_e has $\frac{1}{[km]}[MeV/fm^3]^{1/2}$. The mixed units here come from an integration over radius which is carried out in kilometers [71]. In geometric units this is written more simply as $\rho_e = \alpha \times \rho$ where $\alpha = f \times \frac{0.224536}{\sqrt{G}}$. With these relations, the equation of state can be analyzed for different cases of the charge fraction f and the behaviour of the system can be examined. It is important to note that Ray et al. started by *assuming* a net charge in the star (with a net positive charge distribution), and seeing how the stellar structure is impacted. This is only tangentially related to our question of whether a compact star can form with such a configuration (or whether it would be stable), but the results they find are relevant enough to our discussion to be worth considering.

Examining the results presented in figure 1.5, we immediately see that the modified (charged) TOV equations permit equilibrium solutions with a charge to mass ratio many orders of magnitude higher than the classical estimates. One will notice that for the largest shown charge fraction ($f = 0.001$), the charge-mass relation is very close to linear (in a charge scale of 10^{20} C). In other words this charge fraction can be understood by the relation $Q = \sqrt{G}M$ which implies that the gravitational and Coulomb forces are essentially balanced at the star's surface. This also implies that the charge configuration corresponding to the maximum allowed charge for a global force balance is $\rho_e \approx \sqrt{G}\rho$.

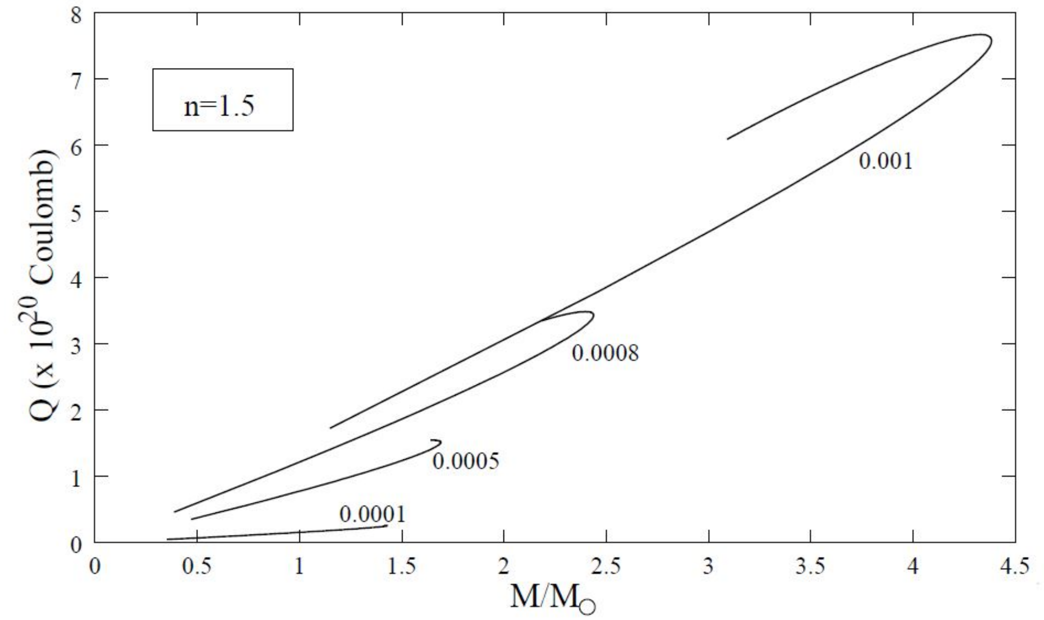

Figure 1.5: The variation of the charge with mass for different f (Ray 2003 [69]). One notices that there are indeed equilibrium conditions with very high charge to mass ratios compared to those allowed by classical approximations.

Unfortunately this global analysis done via the modified TOV equations is only enough to ensure hydrostatic equilibrium, and is not enough to guarantee stability. When one considers an individual charged particle in this system, the Coulomb force it experiences will be on the order of 10^{18} times larger than the gravitational force. This can be easily seen if we compare the net amount of charged particles in the star Z (ie. number of protons minus number of electrons - $Q = Ze$) to the net number of massive particles in the star A. In the maximum charge configuration found from solving the TOV equations, $\frac{Z}{A} \sim 10^{-18}$ and thus these individual charged particles are disproportionately affected by the Coulomb repulsion which will cause them to quickly eject from the system. This means that such stars will be highly unstable unless a mechanism exists which is able to bind a single charged particle to 10^{18} neutral particles.

The above phenomenon has additional consequences. Each ejected charged particle contributes far more to the repulsive Coulomb force of the global hydrostatic equilibrium than it does to the attractive gravitational part, and thus the star will quickly collapse into a charged black hole as protons escape and the global forces fall out of balance in favour of gravitational attraction. If this is an accurate description then we can think of charged compact stars as being in an intermediate state between a supernova collapse and a charged black hole [76].

Gaussian-Like Charge Distribution

In their 2017 thesis, Ndebele [77] repeats many of the calculations done in [69], replacing the charge density with a pseudo-Gaussian distribution, which is also a function of mass density. More specifically,

$$\rho_e = \alpha \times \rho \times \Big(\exp[-(\frac{\rho - a}{b})^2] + 1 \Big) \tag{1.32}$$

where α is a factor which tunes the intensity of the charge density. In figure 1.6 the charge density is plotted as a function of mass density for multiple combinations of the peak parameters a and b. It is easy to see that charge density is more highly concentrated around a particular mass density. The author claims that this form is meant to mimic the situation where the charged particles are pushed outward by one another due to their self-created electrostatic fields.

When solving for these new charge distribution models, the authors found that they were unable to obtain the larger mass/radius values that are typically associated with the

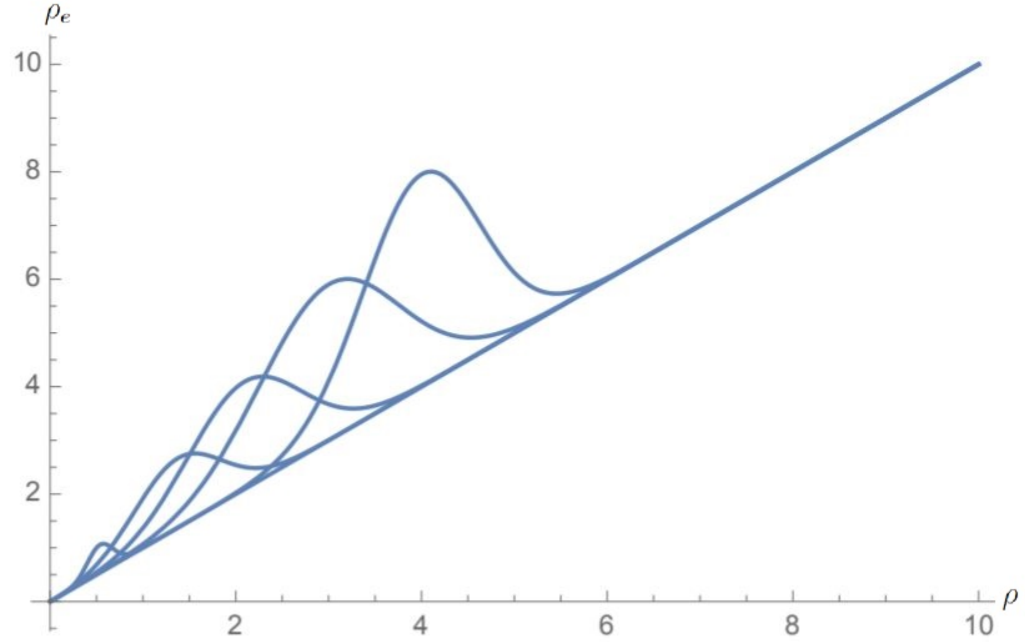

Figure 1.6: Charge density ρ_e plotted as a function of mass density ρ for different combinations of the peak parameters a and b (Ndebele 2017 [77]).

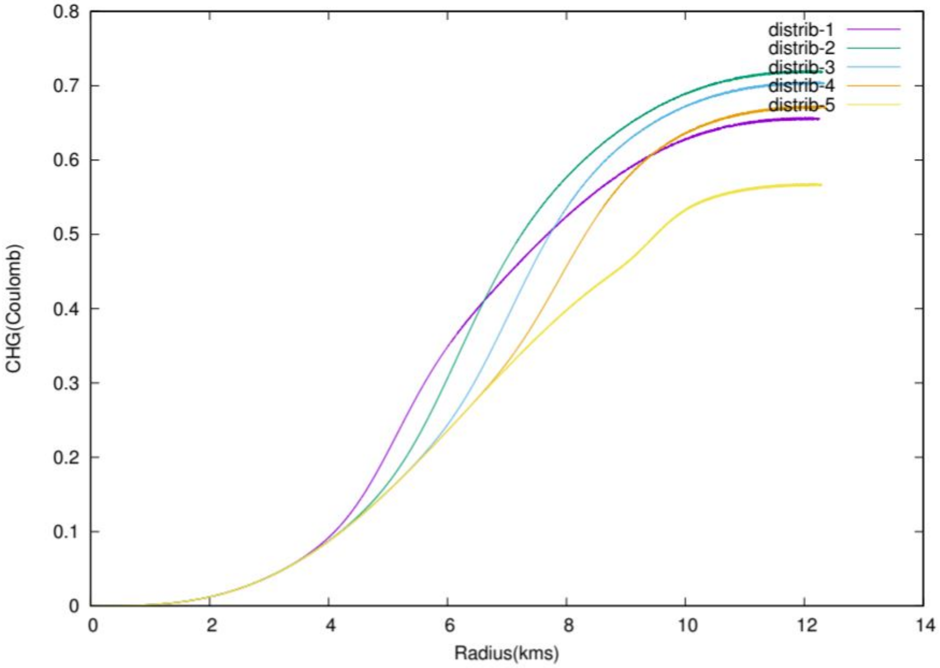

Figure 1.7: Total charge vs. radius for maximum mass ($\leq 4.3M_{\odot}$) configurations for different values of the charge fraction parameter α (Ndebele 2017 [77]).

charged solutions, nor the massive amounts of charge seen in [69]. Since in the current scenario the charged particles have been pushed outward from the centre, the central pressure of the star receives a negligible contribution from the charged particles. This central density term plays a key role in determining the maximum mass configurations of such stars, and the authors argue that a central density that does not have a significant contribution from charge is unlikely to be able to support equilibrium configurations of very high charge.

Generalization of Classical Charge Limits to Traditional Compact Stars

So far we have found that solutions to the TOV equations exist for highly charged compact stars, but there is no currently known mechanism that would keep individual charged particles bound to them. Because of this, the currently accepted view is to consider charged neutron stars as intermediate states preceding charged black holes. For them to be stable, there must be additional forces at work besides gravity and electromagnetism.

In order to generalize the arguments made in section 1.2.1, a star's thermal energy can in principle be replaced in the equations by the degeneracy pressure exerted against charge-carrying particles, which is not usually done in such treatments. We begin by considering the repulsion of like charges for a positively charged compact star.

For a star at the maximum charge limit, the sum of the energy due to repulsive electrostatic forces and the kinetic energy of the proton due to degeneracy pressure should be equal to the gravitational potential on that particle at the surface of the star:

$$k_e \frac{eQ}{R} + E_{DP} = G\frac{Mm_p}{R}. \tag{1.33}$$

Where k_e is the Coulomb constant. Rearranging this for $\frac{Q}{M}$, we find the relation

$$\frac{Q}{M} = \frac{1}{ek_e}\Big(Gm_p - E_{DP}\frac{R}{M}\Big) \tag{1.34}$$

which tells us that the charge to mass ratio in this case also depends on the mass-radius relation for the compact star, so long as degeneracy pressure is held constant. More specifically, a large mass-radius relationship will suppress the degeneracy effects and vice-versa. We notice that the effects of degeneracy pressure are to decrease $\frac{Q}{M}$, and thus the upper limit on this quantity occurs when the degeneracy pressure is negligible compared to gravitational pressure. For positively charged particles in a neutron star this is probably a good approximation since the vast majority of degeneracy effects will only apply to neutrons/electrons (more on this later). Therefore, as an upper limit when degeneracy pressure is negligible we find that this ratio gives

$$\frac{Q}{M} \approx 150\frac{C}{M_\odot} \tag{1.35}$$

which agrees with previous estimates. On the other hand we know that neutron stars must be in β-equilibrium, where the Fermi energy of the neutrons is equal to the sum of the Fermi energies of the free protons and electrons:

$$E_{Fn} = E_{Fp} + E_{Fe}. \tag{1.36}$$

The naïve (probably non-physical) upper limit on the proton degeneracy pressure would occur when $E_{Fn} = E_{Fp}$. At neutron star densities it is easy to check that the electrons would be relativistic ($E_F > mc^2$), but neutrons and protons do not meet the ultra-relativistic criteria, and thus $E_{Fn} = \frac{\pi^2\hbar^2}{2m_n}(\frac{3N}{\pi V})^{2/3}$ where $\frac{N}{V} \approx \frac{\rho}{m_p}$ and $\rho = \frac{3M}{4\pi R^3}$. Plugging this upper limit for degeneracy pressure along with estimates for the mass and radius of an uncharged neutron star from the literature ($R = 7$ km, $M = 2.3\ M_\odot$ [16]) into equation (1.34), we find

$$\frac{Q}{M} \approx 50\frac{C}{M_\odot}, \tag{1.37}$$

as an order of magnitude approximation, giving one third of the charge to mass ratio found when ignoring degeneracy pressure. In other words, strong degeneracy pressure on positively charged particles in a compact star tends to decrease the upper limit of its charge to mass ratio due to the additional outward force on the protons. With that being said, even in the non-physical limiting case these effects aren't strong enough to change $\frac{Q}{M}$ by more than by a factor of a few. Realistically, the case where degeneracy pressure on protons is negligible should be the more appropriate treatment as the degeneracy pressure due to protons is usually negligible compared to that of electrons [16].

Finally, we repeat this calculation once more from an electron trapping perspective (see section 1.2.1). In order for the ejection of free electrons to halt, the electron degeneracy energy should be equal to the sum of the electrostatic and gravitational energies on an electron at the star's surface:

$$E_{De} = \frac{ek_eQ}{R} + \frac{GMm_e}{R}. \tag{1.38}$$

Rearranging we find

$$\frac{Q}{M} = \frac{1}{k_e e}\Big(E_{De}\frac{R}{M} - Gm_e\Big). \tag{1.39}$$

We notice now that in this case, an increased contribution from degeneracy pressure allows for a larger amount of charge per unit mass, since more electrons will eject from the star before equilibrium is reached. This makes sense, keeping in mind that in general $E_{De} \neq E_{Dp}$. Doing another order of magnitude approximation using a typical mass/radius for an uncharged neutron star (and setting $E_{De} = E_{Dn}$) we find an upper limit on the charge to mass ratio of

$$\frac{Q}{M} \approx 100\frac{C}{M_\odot}. \tag{1.40}$$

Of the two approaches with non-vanishing degeneracy pressure on the charged particles this is the more realistic approximation. In systems with comparable amounts of electrons and protons, typically it is fair to assume that the proton degeneracy pressure is negligible compared to that coming from the electrons. This is mainly due to the proton mass being much larger, and thus the same Fermi momentum corresponds to a much smaller energy on these more massive particles.

Regardless of which approach is accurate, none of these calculations suggest any extreme departures from the expected values calculated on non-compact stars. However, it is important to remember that in these order of magnitude estimates that we have been using a common mass-radius relation of uncharged stars. If we plot equation (1.39) as a function of $\frac{R}{M}$ while holding degeneracy pressure constant, we notice that the charge to mass ratio increases linearly with no well-defined upper bound. This is plotted in figure 1.8a, where the red dotted line represents the Schwarzschild radius for an uncharged star ($r_s = \frac{2MG}{c^2}$) and the units are in Coulombs per solar mass. We notice that at this line $\frac{Q}{M}$ is on the order of the estimates made earlier in this section, but there is no reason to think that a star with a strong Coulomb force would collapse at the same mass-radius ratio as one without electromagnetic contributions. In fact, these equations were derived based on the balancing of forces and thus should be valid well past the dotted line. Presumably the collapse would occur at the value of $\frac{R}{M}$ for which the g_{rr} component of the Reissner–Nordström metric diverges. The radius at which this happens is well known and can be simplified into the form $\frac{Q}{M} = f(\frac{R}{M})$, but when plotted alongside equation (1.39) it is many orders of magnitude higher, to the point where they cannot be seen in the same plot. Presumably then this relation is valid for any physical mass-radius pair.

Lastly, it is worth mentioning that holding degeneracy pressure as a constant also causes a loss of generality. Even if we are comfortable making the assumption that $E_{De} = E_{Dn}$, the value of E_{Dn} is a function of M and R. Up until this point we have been using the uncharged $M - R$ estimates to calculate our constant degeneracy pressure. Working this out more carefully, the relation actually looks like this:

$$\frac{Q}{M} = \frac{1}{k_e e}\Big[\frac{\pi^2\hbar^2}{2m_p}\Big(\frac{9}{4\pi^2 m_p}\Big)^{2/3}\frac{1}{R\sqrt[3]{M}} - Gm_e\Big]. \tag{1.41}$$

This function is plotted in as a function of $\frac{1}{R\sqrt[3]{M}}$ figure 1.8b where again $\frac{Q}{M}$ is in units of $\frac{C}{M_\odot}$, and the red dotted line represents the mass-radius estimate of an uncharged neutron star which has been used many times in this section. At the dotted line we see that the

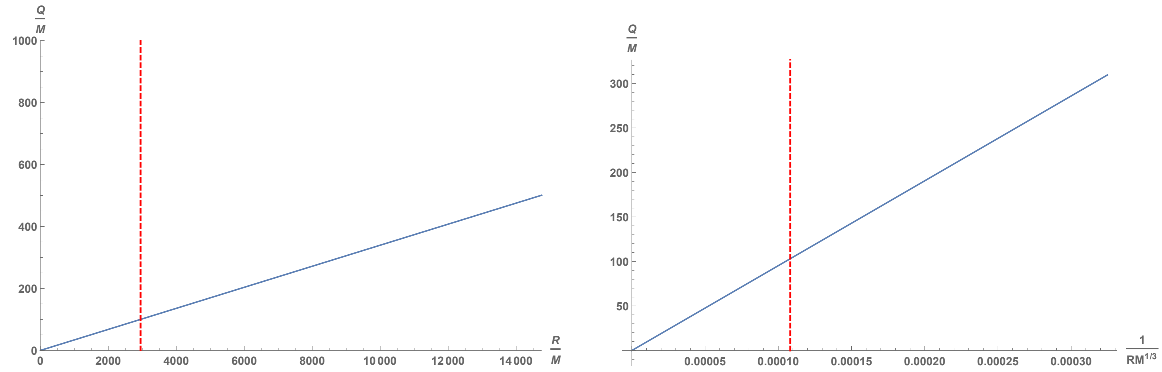

(a) Upper limit on the charge to mass ratio $\frac{C}{M_\odot}$ of a neutron star using the electron trapping model with electron degeneracy pressure held constant. The red dotted line represents the Schwarzschild radius for an uncharged star.

(b) Upper limit on the charge to mass ratio $\frac{C}{M_\odot}$ of a neutron star using the electron trapping model with electron degeneracy pressure in its more general form which depends on mass and radius (see equation (1.41)). The red dotted line represents the mass-radius estimate of an uncharged neutron star from [16].

Figure 1.8: Plots of the charge to mass ratio for models (1.39) and (1.41).

function returns an estimate on the order of the earlier calculations in this section. Again, we expect that this relation is valid past the dotted line, although it is non-trivial to solve for the Reissner–Nordström horizon radius in terms of $R\sqrt[3]{M}$. For this reason, it is unclear where exactly equation (1.41) breaks down, and further exploration is needed.

A more illuminating 3D visualization is plotted in 1.9, with $\frac{Q}{M}$ on the z-axis and R/M on the x and y axes respectively. It is easy to see upon inspection that the charge per unit mass quickly blows up around the R/M axes. When compared to published M-R pairs for observed compact stars, this model still suggests that physical stars should have very little net charge, although it begs the question: if these empirical M-R pairs were estimated with a net charge model assumed, how would the calculated stellar structure change? Since published mass-radii curves assume uncharged gravitating bodies, it should be unsurprising that those M-R pairs match with near neutral stars in the theory.

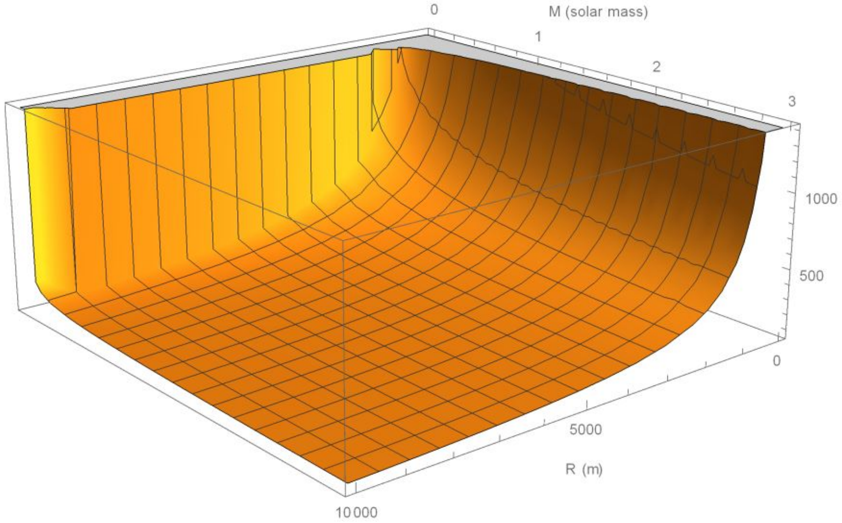

Figure 1.9: Limiting charge to mass ratio $\frac{Q}{M}$ from equation (1.41) plotted as a function of M and R.

1.3 Charged Quark Stars

1.3.1 Introduction to Quark Stars/Matter

During the first half of the 1960s, the quark model was introduced (independently) by Gell-Mann [78] and Zweig [79]. They found that particles like protons and neutrons are not fundamental, but are instead made up of smaller constituent particles called quarks. At typical terrestrial energy levels quarks interact very strongly, and are confined to their composite hadrons. Less than a decade after this discovery, Gross and Wilczek [80] showed that under quantum chromodynamics (QCD) quarks interact weakly at high energies, which allows for perturbative calculations. This idea is referred to as the "asymptotic freedom" of QCD. For a quark-gluon plasma, it suggests a new state of matter that is described via deconfined quark degrees of freedom.

At familiar energy scales (effectively zero temperature and pressure), it is often assumed that normal hadronic matter is the ground state of baryonic matter. At some critical temperature (or baryon chemical potential) this hadronic matter is thought to undergo a phase transition into a quark-gluon plasma [21]. Such an assumption then implies that quark matter is only energetically favourable in extreme conditions [81]. However, the Bodner-Witten-Terazawa hypothesis [82, 83, 84] suggests that the ground state of baryonic matter at low temperature could actually be so-called "strange quark matter" (SQM), a phase of matter made up of comparable amounts of free up (u), down (d), and strange (s) quarks, with an energy per baryon lower than even ^{56}Fe. A more recent (2018) study [81] challenged this view by showing that u, d quark matter (udQM) is more stable than SQM, and can even be more stable than normal nuclear matter at very high baryon number[1] (ie. beyond the end of the periodic table). Since the densities of inner neutron star cores are greater than those in atomic nuclei [85], such conditions are not unreasonable. A stable (or even metastable) form of quark matter would have uncountable consequences in astrophysics and cosmology - in relativistic collision experiments with heavy ions, strangelets (SQM particles) only need to exist for 10^{-8} seconds to have an appreciable effect [21].

If this is true, it is likely that nucleons inside a neutron star will undergo a phase transition into quark matter due to the extreme pressure enforcing a large baryon number. This could conceivably happen only in the star's core (forming what is referred to as a "hybrid" quark star) if QM requires high pressures to stabilize, or throughout the entire stellar body (forming a "true" quark star) if QM is absolutely stable at zero pressure. Alternatively, a mixture of both quark and nuclear matter could exist throughout the star - this we refer to as a "mixed" star [21].

Deconfined quark matter is interesting for many reasons. If such a state does exist, the very early universe likely existed briefly in this phase - the imprints of which could potentially be detected in gravitational wave observations [86]. Furthermore, besides likely existing deep in the core of neutron stars, an also conceivable that some form of quark matter is indeed the ground state of the strong interaction, in which case pulsars may actually be quark stars rather than neutron stars [16]. Inside such stars, QM should act as a colour superconductor. Since practical results for the quark matter equation of state cannot be derived from QCD, the so-called "MIT bag model" [87, 88] is typically employed as a simple means to describe QM. This model describes the internal structure of particles in terms of quark and gluon field variables. Since the field variables of a hadron's constituent quarks should be confined to the subset of points inside that hadron (unlike typical field theories which permeate all of space), the set of points on which the quark's field variables are defined is referred to as a "bag" [88]. The MIT bag model was first introduced as a means of relating hadronic masses to their constituent quarks - it is useful

---

[1] The baryon number B of an atom is identical to its mass number A, since both protons and neutrons are baryons.

for developing insights on more general properties of QM, though precise predictions of parameters (like the critical density required to trigger a phase transition) are not possible [16].

1.3.2 Charged Tolman–Oppenheimer–Volkoff Equations

The Tolman–Oppenheimer–Volkoff equations (see section 1.2.3) are a famous set of differential equations that govern the structure of static, spherically symmetric massive bodies under the laws of general relativity. For a star holding a net charge, the equations are obtained by solving the Einstein-Maxwell equations on a static, spherically symmetric metric of the form [12, 13, 16]:

$$ds^2 = -e^{2\nu}dt^2 + e^{2\Lambda}dr^2 + r^2\left(d\theta^2 + \sin^2\theta d\phi^2\right) \tag{1.42}$$

where ν and Λ are functions of (r,t) in general, and the star's interior is modelled as a perfect fluid:

$$T_{\mu\nu} = (\rho + P)u_\mu u_\nu + P g_{\mu\nu}. \tag{1.43}$$

Since we are interested in an equilibrium solution, we take the solutions to the static case including charge effects [69]. This yields the following four equations to be solved simultaneously:

$$\frac{\mathrm{d}q}{\mathrm{d}r} = 4\pi r^2 \rho_e e^{\Lambda} \tag{1.44}$$

$$\frac{\mathrm{d}m}{\mathrm{d}r} = 4\pi r^2 \rho + \frac{q}{r}\frac{\mathrm{d}q}{\mathrm{d}r} \tag{1.45}$$

$$\frac{\mathrm{d}P}{\mathrm{d}r} = -(\rho + P)\left(4\pi r P + \frac{m}{r^2} - \frac{q^2}{r^3}\right)e^{2\Lambda} + \frac{q}{4\pi r^4}\frac{\mathrm{d}q}{\mathrm{d}r} \tag{1.46}$$

$$\frac{\mathrm{d}\nu}{\mathrm{d}r} = -\frac{1}{\rho + P}\left(\frac{\mathrm{d}P}{\mathrm{d}r} - \frac{q}{4\pi r^4}\frac{\mathrm{d}q}{\mathrm{d}r}\right) \tag{1.47}$$

where $q(r)$ and $m(r)$ represent the charge and mass (respectively) contained within a radius r, $\rho_e(r)$ is the electric charge density at r, and

$$e^{-2\Lambda(r)} = 1 - \frac{2m(r)}{r} + \frac{q(r)^2}{r^2}. \tag{1.48}$$

If we rescale the charged TOV equations according to

$$\bar{m} = m\sqrt{4B_{\text{eff}}}, \quad \bar{r} = r\sqrt{4B_{\text{eff}}}, \tag{1.49}$$

and

$$\bar{q} = q\sqrt{4B_{\text{eff}}}, \quad \bar{\rho}_e = \frac{\rho_e}{4B_{\text{eff}}}, \tag{1.50}$$

eqs. (1.44) to (1.47) can be rewritten in a dimensionless form, with barred symbols replacing their unbarred counterparts. In the above re-scaling B_{eff} is the effective Bag constant, which accounts for non-perturbative contributions from the QCD vacuum. Finally, we specify boundary conditions for the charged TOV equations given an arbitrary central mass density ρ_c:

$$q(0) = m(0) = 0, \quad \rho(0) = \rho_{\text{c}}, \quad \nu(R) = -\Lambda(R), \tag{1.51}$$

where R is the star's radius (determined by enforcing $P(R) = 0$), M is the total mass of the star (ie. $m(R) = M$), and Q is the net charge ($q(R) = Q$). These equations can be solved repeatedly over a range of central densities ρ_c to fill out the $M - R$ curve for a given equation of state and charge distribution model (the latter of which will be addressed in chapter 2).

1.3.3 Equations of State

The equation of state of a system is, at its core, a relationship between energy density and pressure. As such, the compressibility of the constituent matter is reflected in the "stiffness" of the EOS - a stiffer EOS will have a higher pressure at every energy density [16]. The unusually stiff equation of state for quark stars (due to QM being relatively incompressible) theoretically allows them to sustain a greater amount of mass than neutron stars before gravitational collapse into a black hole.

The equation of state adopted by Oppenheimer and Volkoff [12] for their first neutron star model was that of a cold, ideal (non-interacting) Fermi gas of neutrons, although it is known that pure neutron matter is highly unstable. Since neutrons must obey the Pauli-exclusion principle, some of these particles in highly dense matter would have sufficient energy to β-decay into a proton, electron, and neutrino [16]. To begin with it is more interesting to describe the star in its equilibrium configuration, after such processes have ceased and the matter has reach its ground state. A more realistic (but still idealized) approach follows from instead describing compact stars as an electrically neutral, degenerate ideal gas of neutrons, protons, and electrons, the number density of each being such that the gas occupies its minimum energy state. This situation is known as β-equilibrium, where the remaining neutrons will no longer decay, and similarly, electron capture on a proton is not energetically favourable.

The specifics of these derivations vary widely depending on the end goal of the calculations (and in general the resulting EOS can be very complicated), but in asymptotic limits (or over a limited range) of parameter space, the equation often may be approximated as a power law [89]. This approximation is usually referred to as the "polytropic" equation of state [16], and takes the form

$$P = K\rho^{\gamma} \tag{1.52}$$

where P and ρ refer to pressure and energy density (respectively), K is a proportionality constant, and γ is the so-called polytropic index (PI). Note that often this is written instead as $P = K\rho^{\frac{n+1}{n}}$ where n is referred to as the PI [90].

On the other hand, compact stars made up of quark matter should have a much stiffer equation of state derived from different assumptions. The typical non-interacting quark matter equation of state [1, 16] is written

$$P = \frac{1}{3}(\rho - 4B_{\text{eff}}) \tag{1.53}$$

where P and ρ are again pressure and energy density, and B_{eff} is the effective bag constant. However, recently a new unified, interacting quark matter equation of state was derived, which includes the perturbative QCD (pQCD) correction and colour superconductivity, for both *ud*QM and SQM [91]. In this approach, all interaction models are unified via a simple reparameterization, maximally reducing the degrees of freedom. In doing so, all information regarding the interaction strength of QM is governed by a single dimensionless parameter $\bar{\lambda}$:

$$\bar{\lambda} = \frac{\lambda^2}{4B_{\text{eff}}} = \frac{\left(\xi_{2a}\Delta^2 - \xi_{2b}m_s^2\right)^2}{4B_{\text{eff}}\xi_4 a_4} \tag{1.54}$$

where Δ represents the colour superconductivity gap parameter, m_s is the contribution of the strange quark mass (if applicable), and a_4 characterizes the pQCD contribution from one-gluon exchange (where $a_4 = 1$ represents a vanishing pQCD correction). One notices that increasing pQCD effects (decreasing a_4) always maps to stronger interaction effects, whereas larger colour superconducting effects (larger Δ) or a smaller m_s only maps to a larger $\bar{\lambda}$ when $\lambda > 0$ [1]. Furthermore, the constant coefficients are

$$(\xi_4, \xi_{2a}, \xi_{2b}) = \begin{cases} (((\frac{1}{3})^{\frac{4}{3}} + (\frac{2}{3})^{\frac{4}{3}})^{-3}, 1, 0) & \text{2SC phase} \\ (3, 1, 3/4) & \text{2SC+s phase} \\ (3, 3, 3/4) & \text{CFL phase} \end{cases} \tag{1.55}$$

for the different types of considered quark matter, characterizing the possible phases of color superconductivity - interacting quark matter includes effects from strong interactions that can modify its behavior, such as one-gluon exchange or color superconductivity. One-gluon exchange induces perturbative quantum chromodynamic (pQCD) corrections to the free energy [92, 93, 94]. Furthermore, a spin-0 Cooper-pair condensate anti-symmetric in color-flavor space is expected to lower the energy [95, 96, 97], resulting in two-flavor color superconductivity, where u quarks pair with d quarks. This is conventionally termed “2SC” /“2SC+s” without/with strange quarks, or the color-flavor locking (CFL) phase in which u, d, s quarks pair with each other antisymmetrically.

Furthermore, the size of the effective bag constant B_{eff} in the above expressions is flavour-dependent. With this in mind, the dimensionless, unified, interacting quark matter equation of state can be written

$$\bar{P} = \frac{1}{3}(\bar{\rho} - 1) + \frac{4}{9\pi^2}\bar{\lambda}\left(-1 + \text{sgn}(\lambda)\sqrt{1 + \frac{3\pi^2}{\bar{\lambda}}\left(\bar{\rho} - \frac{1}{4}\right)}\right) \tag{1.56}$$

where the energy density and pressure have been rescaled into a dimensionless form according to

$$\bar{\rho} = \frac{\rho}{4B_{\text{eff}}}, \bar{P} = \frac{P}{4B_{\text{eff}}}. \tag{1.57}$$

In the limit $\bar{\lambda} \to 0$, (1.56) reduces to the non-interacting quark EOS shown in equation (1.53). From (1.56) it is also easy to show that $\partial \bar{P}/\partial \bar{\lambda} > 0$, implying that a larger $\bar{\lambda}$ corresponds to a stiffer EOS. In the extreme limit of interaction strength, equation 1.56 takes the form

$$\bar{P}\Big|_{\lambda\to\infty} = \bar{\rho} - \frac{1}{2} \tag{1.58}$$

or, equivalently, $P = \rho - 2B_{\text{eff}}$. It is easy to see that in this extreme interaction limit, the surface mass density of the quark star has decreased from $\rho_0 = 4B_{\text{eff}}$ to $\rho_0 = 2B_{\text{eff}}$. Moreover, this increases the speed of sound ($c_s^2 = \partial P/\partial \rho$) within quark matter from 1/3 to 1 (light speed) maximally [91].

1.3.4 Radial Stability

Primarily of interest are solutions to the TOV equations which are stable under radial perturbations - a problem dating back to Chandrasekhar [98] in 1964. This is modelled for charged quark stars in [1, 99] as the displacement of a fluid element from its equilibrium position r to $r + \delta r$, where the perturbation has a harmonic time dependence $e^{i\omega t}$ [100]. The first and second order rates of change of the renormalized displacement $u = r^2 e^{-\nu(r)}\delta r$ are written

$$\frac{\mathrm{d}u}{\mathrm{d}r} = \frac{\eta}{\mathcal{P}}, \tag{1.59}$$

$$\frac{\mathrm{d}\eta}{\mathrm{d}r} = -\left[\mathcal{Q} + \omega^2 \mathcal{W}\right] u \tag{1.60}$$

where

$$\mathcal{P} = e^{\Lambda+3\nu} r^{-2} \gamma P, \tag{1.61}$$

$$\mathcal{Q} = (\rho + P) r^{-2} e^{\Lambda+3\nu} \left[\nu'\left(\nu' - 4r^{-1}\right) - \left(8\pi P + r^{-4} q^2\right) e^{2\Lambda}\right], \tag{1.62}$$

$$\mathcal{W} = e^{3\Lambda+\nu} r^{-2} (\rho + P), \tag{1.63}$$

with

$$\gamma = \frac{\rho + P}{P}\frac{dP}{d\rho} \tag{1.64}$$

as the adiabatic index. We can obtain a series of eigenfrequencies ω_n^2 by solving eqs. (1.59) and (1.60) along with the boundary conditions

$$\eta(0) = 1, \qquad u(0) = \frac{r^3}{3\mathcal{P}(0)}, \qquad \frac{\mathrm{d}u}{\mathrm{d}r}\Big|_{r=R} = \eta(R) = 0 \tag{1.65}$$

using a numerical shooting method. The condition for radial stability is a non-negative fundamental mode eigenfrequency, ie. $\omega_0^2 \geq 0$. For uncharged compact stars this condition is equivalent to $\partial M/\partial \rho_c \geq 0$ - the zero fundamental eigenfrequency point coincides with the maximum mass point [16], although once charge is introduced this coincidence no longer holds [101, 102]. Similar to what was done in section 1.3.2, all variables in the above equations can simply be replaced with their rescaled unitless counterparts. The dimensionless eigenfrequencies scale like $\bar{\omega}_n = \omega_n/\sqrt{4B_{\text{eff}}}$.

Oscillation modes outside of the fundamental can also be interesting because they encode information about the internal structure and thermodynamic properties of compact stars [103, 1]. Oscillations in neutron stars can be excited "by accretion, tidal forces in close eccentric binary systems, starquakes caused by cracks in the crust, magnetic reconfiguration, during the supernova explosion, or any other dynamical instabilities" [104, 105, 106, 107, 108]. This field of study is usually referred to as neutron star seismology or astroseismology, and besides this reference will be outside the scope of this thesis.

1.4 Gauss-Bonnet Gravity

1.4.1 Introduction to Modified and Higher Curvature Gravity Theories

At the beginning of this chapter we discussed how the field equations of general relativity presume a linear relationship between curvature and stress energy, and how this is not logically necessary. The most common examples of higher curvature (gravity) theories (HCTs) are the higher order Lovelock [109, 26] theories and so-called quasi-topological gravities [110, 111], both of which are only non-trivial in $D \geq 5$ (see section 1.4.2), and both of which are characterized by a single black hole metric function determined by an algebraic equation. Recently it was noticed that both of these theories belong to a larger class of gravity theories which are now called "generalized quasi-topological gravities" (GQTGs) [27, 112].

GQTGs exist at arbitrarily high curvature orders, and are classified by the possession of non-hairy generalizations of the Schwarzschild black hole (satisfying $g_{tt}g_{rr} = -1$) and second-order equations of motion when linearized around maximally symmetric backgrounds [27]. These theories can be automatically integrated once, and from there can be further broken into two cases. The first group includes the Lovelock and quasi-topological theories where the resulting equation on the metric function is algebraic, whereas the second group's metric function depends on a second-order differential equation [68] (or, in general, a fourth-order differential equation when the background is not static and spherically symmetric). Einsteinian cubic gravity (or ECG) was the first representative of the latter group [25]. The action for GQTG theories takes the form [27]:

$$S = \frac{1}{16\pi} \int \mathrm{d}^D x \sqrt{|g|} \left[-2\Lambda + R + \sum_{n=2} \sum_{i_n} \ell^{2(n-1)} \mu_{i_n}^{(n)} \mathcal{R}_{i_n}^{(n)} \right] \tag{1.66}$$

where $\mathcal{R}_{i_n}^{(n)}$ are densities constructed from the metric and n Riemann tensors, $\mu_{i_n}^{(n)}$ are coupling constants, ℓ is some length scale, and i_n is an index running over all independent GQTG invariants of order n.

1.4.2 Lovelock's Theorem

A common way to derive the field equations in introductory GR textbooks [53] is to consider all possible symmetric (0, 2) tensors which are second order in derivatives of the metric and preserve properties like conservation of energy. More concretely, in his 1971 paper "The Einstein Tensor and Its Generalizations", David Lovelock broke this problem down to finding a tensor A^{ij} which satisfies the following four properties:

(a) $A^{ij} = A^{ji}$

(b) $A^{ij} = A^{ij}(g_{ab}; g_{ab,c}; g_{ab,cd})$

(c) $A^{ij}{}_{|j} = 0$

(d) A^{ij} is linear in second derivatives of g_{ab}

and showed that in a four dimensional spacetime, such a tensor must take the form (see also [113]):

$$A^{ij} = aG^{ij} + bg^{ij} \tag{1.67}$$

where a and b are both constants - ie. A is proportional to the Einstein tensor plus a cosmological term. As a consequence it can be concluded that Einstein's field equations are the only possible equations of motion under these conditions in four dimensions. In order to modify general relativity in 4D it becomes necessary to either add in additional fields besides the metric tensor, accept non-locality or emergence, or relax one of the above conditions on A (such as allowing higher order derivatives of the metric).

1.4.3 Naïve Rescaling of the 4D Gauss-Bonnet Coupling Constant

According to Lovelock's theorem [109], the Einstein-Hilbert action (see section 1.1) describes the most general theory of gravity in four dimensions. However, in $D \geq 5$ the most general action contains more terms [29] (higher order Lovelock invariants) which contribute non-trivially to the gravitational dynamics. The first of these terms turns out to be the Gauss-Bonnet action term:

$$S_{\mathrm{GB}} = \int \sqrt{-g}\alpha\mathcal{G}\; d^D x \tag{1.68}$$

where again α is a coupling constant, and $\mathcal{G} = R^{\mu\nu}{}_{\rho\sigma}R^{\rho\sigma}{}_{\mu\nu} - 4R^{\mu}{}_{\nu}R^{\nu}{}_{\mu} + R^2$ is the Gauss-Bonnet invariant. In $D = 4$, $\mathcal{G}$ is a total derivative and thus does not contribute to gravitational dynamics. This is perhaps most easily demonstrated by taking the trace of the Gauss-Bonnet contribution to the field equations:

$$\frac{g_{\mu\nu}}{\sqrt{-g}}\frac{\delta S_{\mathrm{GB}}}{\delta g_{\mu\nu}} = (D-4) \times \frac{\alpha}{2}\mathcal{G} \tag{1.69}$$

which clearly vanishes in $D = 4$. This is not just a feature of the trace - the GB contribution to all components of the field equations is indeed proportional to $(D-4)$ [114, 115].

In 2020 Glavan & Lin published a paper considering the $D \to 4$ limit of this theory [29], an idea which was inspired by dimensional regularization in quantum field theory, and is particularly reminiscent of the conformal trace anomaly which arises in curved spacetimes [116]. In considering this limit, a finite contribution is made to come out of the Gauss-Bonnet term which connects back to GR smoothly as $\alpha \to 0$ with no change in degrees of freedom. Not only that, the paper also shows that the limiting 4DGB theory is not equivalent to Einstein's gravity, seemingly violating the Lovelock theorem.

Following this publication, a number of articles [40, 41, 42] came out shortly after criticizing the method. Gürses et al. [40] pointed out that Glavan & Lin were implicitly asking how the Gauss-Bonnet tensor

$$\begin{aligned} H_{\mu\nu} = 2\Big[& RR_{\mu\nu} - 2R_{\mu\alpha\nu\beta}R^{\alpha\beta} + R_{\mu\alpha\beta\sigma}R_{\nu}^{\alpha\beta\sigma} - 2R_{\mu\alpha}R_{\nu}^{\alpha} \\ & -\frac{1}{4}g_{\mu\nu}\left(R_{\alpha\beta\rho\sigma}R^{\alpha\beta\rho\sigma} - 4R_{\alpha\beta}R^{\alpha\beta} + R^2\right)\Big] \end{aligned} \tag{1.70}$$

goes to zero as $D \to 4$. This can be better analyzed by rewriting $H_{\mu\nu}$ as the sum of two terms:

$$H_{\mu\nu} = 2\left(\mathcal{L}_{\mu\nu} + \mathcal{Z}_{\mu\nu}\right), \tag{1.71}$$

the first of which has no explicit dimensional dependence ($\mathcal{L}_{\mu\nu} := C_{\mu\alpha\beta\sigma}C_{\nu}{}^{\alpha\beta\sigma} - \frac{1}{4}g_{\mu\nu}C_{\alpha\beta\rho\sigma}C^{\alpha\beta\rho\sigma}$), and the second term having only terms which depend on D [40]:

$$\begin{aligned}\mathcal{Z}_{\mu\nu} := \frac{(D-4)(D-3)}{(D-1)(D-2)}\Bigg[& -\frac{2(D-1)}{(D-3)}C_{\mu\rho\nu\sigma}R^{\rho\sigma} - \frac{2(D-1)}{(D-2)}R_{\mu\rho}R^{\rho}_{\nu} + \frac{D}{(D-2)}R_{\mu\nu}R \\ & + \frac{1}{(D-2)}g_{\mu\nu}\left((D-1)R_{\rho\sigma}R^{\rho\sigma} - \frac{D+2}{4}R^2\right)\Bigg].\end{aligned} \tag{1.72}$$

All dimensional factors are kept explicit above to aid in discussing the limiting behaviour. Furthermore, the dimensional term can very simply be reduced to a new tensor which is finite in the $D \to 4$ limit:

$$\mathcal{S}_{\mu\nu} := \frac{2}{D-4}\mathcal{Z}_{\mu\nu}. \tag{1.73}$$

If we were to naïvely assume the Lanczos-Bach [117, 118] identity:

$$C_{\mu\alpha\beta\sigma}C_{\nu}{}^{\alpha\beta\sigma} = \frac{1}{4}g_{\mu\nu}C_{\alpha\beta\rho\sigma}C^{\alpha\beta\rho\sigma} \tag{1.74}$$

(which holds for any smooth metric in 4D) on (1.71), one would find that $\mathcal{L}_{\mu\nu} = 0$, and consequently

$$\lim_{D\to 4}\left(\frac{1}{D-4}H_{\mu\nu}\right) = \mathcal{S}_{\mu\nu}. \tag{1.75}$$

Unfortunately the tensor $\mathcal{S}$ (and consequently $\mathcal{H}$) does not obey the Bianchi identity, ie:

$$\nabla^{\mu}\mathcal{S}_{\mu\nu} \neq 0, \tag{1.76}$$

and thus cannot be used to describe the 4D theory unless

$$\frac{2}{D-4}\mathcal{L}_{\mu\nu} = \mathcal{T}_{\mu\nu} \quad \text{for } D \neq 4. \tag{1.77}$$

In this case, we find a discontinuity in the Gauss-Bonnet tensor at $D = 4$ since

$$\frac{1}{D-4}H_{\mu\nu} = \begin{cases} T_{\mu\nu} + \mathcal{S}_{\mu\nu}, & \text{for } D \neq 4, \\ \frac{0}{0}, & \text{for } D = 4. \end{cases} \tag{1.78}$$

meaning that

$$\lim_{D\to 4} g^{D}_{\mu\nu} \neq g^{\lim}_{\mu\nu} \tag{1.79}$$

in general, where $g^{D}_{\mu\nu}$ is a valid metric for $D > 4$, and $g^{\lim}_{\mu\nu}$ is a metric from the limiting equations above. With this, Gurses et al. [40] show that the Gauss-Bonnet tensor H is always higher dimensional, even after the normalization procedure. Stated another way, Glavan & Lin took the limit of a solution, but this is not necessarily a solution to the limiting equations (although it can be), and furthermore, doesn't tell you what those limiting equations really are.

Furthermore, Ai [41] brings up the so-called "index problem" of taking the limit of dimension in general tensor equations: "what does it mean by taking $D = 2.1$ in [the field equations] if we are concerned about indices"? Assuming the indices take the values of the spacetime in the limit will (in the case of 4DGB) cause the Gauss-Bonnet tensor to vanish identically, and besides, the indices are not continuous. They point out that physical interpretations are likely to follow from scalar equations (ie. the trace of the Einstein equation), whereas general tensor equations require embedding into a higher dimensional spacetime and the implications are less obvious.

1.4.4 4DGB Gravity as a Scalar-Tensor Theory

Although a simple rescaling of the coupling constant α is not enough for a well-defined theory, purely four dimensional Gauss-Bonnet gravity has since been obtained, both via Kaluza-Klein-like procedures (see [46, 35] for details), as well via a method first used by as a Mann and Ross [45, 43] (where the metric undergoes the conformal transformation

$g_{\mu\nu} \to e^{-2\phi} g_{\mu\nu}$, with ϕ being an additional scalar metric function). In this way we arrive at the following expression for the 4DGB action [43]:

$$S_4^G = \lim_{D\to 4} S_D^{GB} = \alpha \int d^4x\sqrt{-g}\left[\frac{1}{2}\psi\mathcal{G} - G^{\mu\nu}\nabla_\mu\psi\nabla_\nu\psi - \frac{1}{8}\left((\nabla\psi)^2\right)^2 - \frac{1}{2}(\nabla\psi)^2\Box\psi\right] \tag{1.80}$$

while making no assumptions about particular solutions to higher dimensional theories or background spacetimes.

From this the equations of motion follow, with that for the scalar being given by

$$\begin{aligned}\mathcal{E}_\phi =& -\mathcal{G} + 8G^{\mu\nu}\nabla_\nu\nabla_\mu\phi + 8R^{\mu\nu}\nabla_\mu\phi\nabla_\nu\phi - 8(\Box\phi)^2 + 8(\nabla\phi)^2\Box\phi + 16\nabla^a\phi\nabla^\nu\phi\nabla_\nu\nabla_\mu\phi \\ & + 8\nabla_\nu\nabla_\mu\phi\nabla^\nu\nabla^\mu\phi - 24\lambda^2 e^{-4\phi} - 4\lambda R e^{-2\phi} + 24\lambda e^{-2\phi}\left[(\nabla\phi)^2 - \Box\phi\right] \\ =& \, 0\end{aligned} \tag{1.81}$$

and the variation with respect to the metric yields

$$\begin{aligned}\mathcal{E}_{\mu\nu} =& \Lambda g_{\mu\nu} + G_{\mu\nu} + \alpha\left[\phi H_{\mu\nu} - 2R\left[(\nabla_\mu\phi)(\nabla_\nu\phi) + \nabla_\nu\nabla_\mu\phi\right] + 8R^\sigma_{(\mu}\nabla_{\nu)}\nabla_\sigma\phi + 8R^\sigma_{(\mu}\left(\nabla_{\nu)}\phi\right)(\nabla_\sigma\phi)\right. \\ & - 2G_{\mu\nu}\left[(\nabla\phi)^2 + 2\Box\phi\right] - 4\left[(\nabla_\mu\phi)(\nabla_\nu\phi) + \nabla_\nu\nabla_\mu\phi\right]\Box\phi - \left[g_{\mu\nu}(\nabla\phi)^2 - 4(\nabla_\mu\phi)(\nabla_\nu\phi)\right](\nabla\phi)^2 \\ & +8\left(\nabla_{(\mu}\phi\right)\left(\nabla_{\nu)}\nabla_\sigma\phi\right)\nabla^\sigma\phi - 4g_{\mu\nu}R^{\sigma\rho}\left[\nabla_\sigma\nabla_\rho\phi + (\nabla_\sigma\phi)(\nabla_\rho\phi)\right] + 2g_{\mu\nu}(\Box\phi)^2 - 2g_{\mu\nu}(\nabla_\sigma\nabla_\rho\phi)(\nabla^\sigma\nabla^\rho\phi) \\ & - 4g_{\mu\nu}(\nabla^\sigma\phi)(\nabla^\rho\phi)(\nabla_\sigma\nabla_\rho\phi) + 4(\nabla_\sigma\nabla_\nu\phi)(\nabla^\sigma\nabla_\mu\phi) + 4R_{\mu\nu\sigma\rho}\left[(\nabla^\sigma\phi)(\nabla^\rho\phi) + \nabla^\rho\nabla^\sigma\phi\right] \\ & \left.+3\lambda^2 e^{-4\phi}g_{\mu\nu} - 2\lambda e^{-2\phi}\left(G_{\mu\nu} + 2(\nabla_\mu\phi)(\nabla_\nu\phi) + 2\nabla_\nu\nabla_\mu\phi - 2g_{\mu\nu}\Box\phi + g_{\mu\nu}(\nabla\phi)^2\right)\right] \\ =& \; 0\end{aligned} \tag{1.82}$$

where H is again the Gauss-Bonnet tensor (see equation (1.70)). These field equations satisfy the following relationship

$$0 = g^{\mu\nu}\mathcal{E}_{\mu\nu} + \frac{\alpha}{2}\mathcal{E}_\phi = 4\Lambda - R - \frac{\alpha}{2}\mathcal{G} \tag{1.83}$$

which can act as a useful consistency check to see whether prior solutions generated via the Glavin/Lin method are even possible solutions to the theory. With this, it is easy to verify that the rotating metrics generated from a Newman-Janis algorithm [32, 52] are not solutions to the well-defined scalar-tensor theory.

Chapter 2

Stellar Structure and Stability of Charged Interacting Quark Stars and Their Scaling Behaviour

In this chapter, we explore the stellar structure and radial stability of charged quark stars composed of interacting quark matter in three classes of commonly used charge models. We adopt a general parametrization of the interacting quark matter equation of state that combines corrections from perturbative QCD, color superconductivity, and the strange quark mass into one parameter λ, or one dimensionless parameter $\bar{\lambda} = \lambda^2/(4B_{\mathrm{eff}})$ after rescaling via the effective bag constant B_{eff}.

We find that increasing charge tends to increase the mass and radius profiles, as well as enlarging the separation along the mass axis between the maximum mass point and the zero eigenfrequency $\omega_0^2 = 0$ of the fundamental radial oscillation mode. The sign of the separation in central density depends on the charge model; this separation also has a dependence on λ such that increasing λ (which can occur for either large color superconductivity or small strange quark mass) tends to decrease this separation size for the first and third classes of charge models monotonically. Moreover, for the second and third classes of charge models, we manage to numerically and analytically identify a new kind of stellar structure with a zero central pressure but with a finite radius and mass. All the calculations and analysis are performed in a general re-scaled form so that the results are independent of explicit values of dimensional parameters. This project has since been published in *Physical Review D* [1].

2.1 Introduction

One of the key challenges of strong interaction physics is that of understanding matter at very high densities [20], in particular at those lower temperatures expected within compact stars. Empirically it is known that matter can bind at nuclear densities to form neutron stars. However, it is theoretically possible to exceed this limit, in which case the most compact stable stars would be described in terms of deconfined quark degrees of freedom.

Taking into account color superconductivity and pQCD corrections generally yields predictions of larger masses and radii for quark stars, due to their stiff equation of state (EOS) compared to those of neutron stars and “normal” quark stars in which such interactions are neglected [119]. These interacting quark stars have been shown to have regions of parameter space which match current astrophysical constraints [120, 91] and are able to produce gravitational-wave echoes [121].

Compact stars are conventionally assumed to be (net) charge-neutral (or nearly neutral) objects, with charge-to-mass estimates bounded by the arguments in section 1.2.1. Details on the stellar structure of uncharged interacting quark stars can be found in [91]. However, for compact stars where the degeneracy pressure of the particles also balances the gravitational pull, relativistic effects and high densities must be taken into account [122]. Compact stars with a certain charge density profile can globally balance a huge net charge (of order 10^{20}C) determined from solutions to the TOV equations [69]. This large charge is well beyond the stability bound of 100 C set by the Newtonian approximation for an individual charged particle at the star surface. In this sense, as [69] argued, such a star would be short lived, since individual charged particles would rapidly be ejected from it, upon which it would collapse to a black hole.

This argument likely does not apply to quark stars since they are not composed of neutral objects but rather a gas of quarks and gluons. Considering the abundance of positively charged (up) quarks and the associated strong interaction effects, the possibility that charged quark stars exist remains an interesting open question. A number of authors have published on the topic [123, 102, 124, 101, 125, 126]. However none included the unification of pQCD corrections and colour superconductivity effects. Furthermore, their analysis and results heavily depend on ad hoc values of several empirical parameters (such as the bag constant, strange quark mass, superconducting gap, flavor composition, etc.) resulting in a loss of generality in their results.

In this project we attempt to fill these gaps using the re-scaled, unified, interacting equation of state (1.56) along with the re-scaled charged TOV equations outlined in section 1.3.2 and the radial stability equations in shown in section 1.2.2. With this, we explore the stellar structure and radial stability of charged quark stars subject to three different charge distribution models.

2.2 Charge Distribution Models

Here we outline three benchmark models for stellar charge distribution that are commonly used in the literature [69, 123, 102, 124, 101, 125].

- Model A: *charge density proportional to energy density*

  $$\rho_e = \alpha\rho\,, \tag{2.1}$$

  where α is a parameter in the range $0 \leq \alpha \leq 1$. After re-scaling using (1.49) and (1.50), we obtain the dimensionless relation

  $$\bar{\rho}_e = \alpha\bar{\rho} \tag{2.2}$$

- Model B: *charge proportional to spatial volume*

  $$q(r) = Q\left(\frac{r}{R}\right)^3 \equiv \beta r^3\,, \tag{2.3}$$

  which reads

  $$\bar{q}(\bar{r}) = \bar{\beta}\bar{r}^3. \tag{2.4}$$

  in dimensionless form, where

  $$\bar{\beta} = \frac{\beta}{4B_{\text{eff}}}. \tag{2.5}$$

- Model C: *fixed total charge*

  Fixing the total charge to be Q, this model corresponds fixing the dimensionless quantity

  $$\bar{Q} = Q\sqrt{4\,B_{\text{eff}}} \tag{2.6}$$

  using equation (1.50).

These different charge models can then be inserted into eqs. (1.44) to (1.47), and we numerically solve this set of differential equations for different values of the charge parameter (α, β, or Q depending on model) and interaction strength. We additionally carry out a stability analysis using eqs. (1.59) and (1.60) and compare the maximum mass point in each case to the critical stability point.

2.3 Results for Positive λ

Here we present the results of the stellar structure (mass, radius, central density) and the radial stability for charged interacting quark stars with a positive interaction coefficient λ. This condition corresponds to $\Delta^2/m_s^2 > \xi_{2b}/\xi_{2a}$, where again Δ is the gap parameter, m_s is the strange quark mass, and ξ_{2a}/ξ_{2b} are the constants from equation (1.55), characterizing the phases of colour superconductivity. Radial stability is dictated by the location of the dimensionless zero fundamental eigenfrequency point $\bar{\omega_0}$ from equation (1.60), which we solve for via a numerical shooting method.

2.3.1 Model A

Plots of interacting quark star mass in terms of radius $\bar{R}$ and central density $\bar{\rho}_c$ of interacting quark stars are shown in Fig. 2.1 for model A-type charge configurations, where the red dots and black squares, respectively, indicate the points of maximum mass and zero eigenfrequency of the fundamental radial oscillation mode for each case. We plot results for four different values of α.

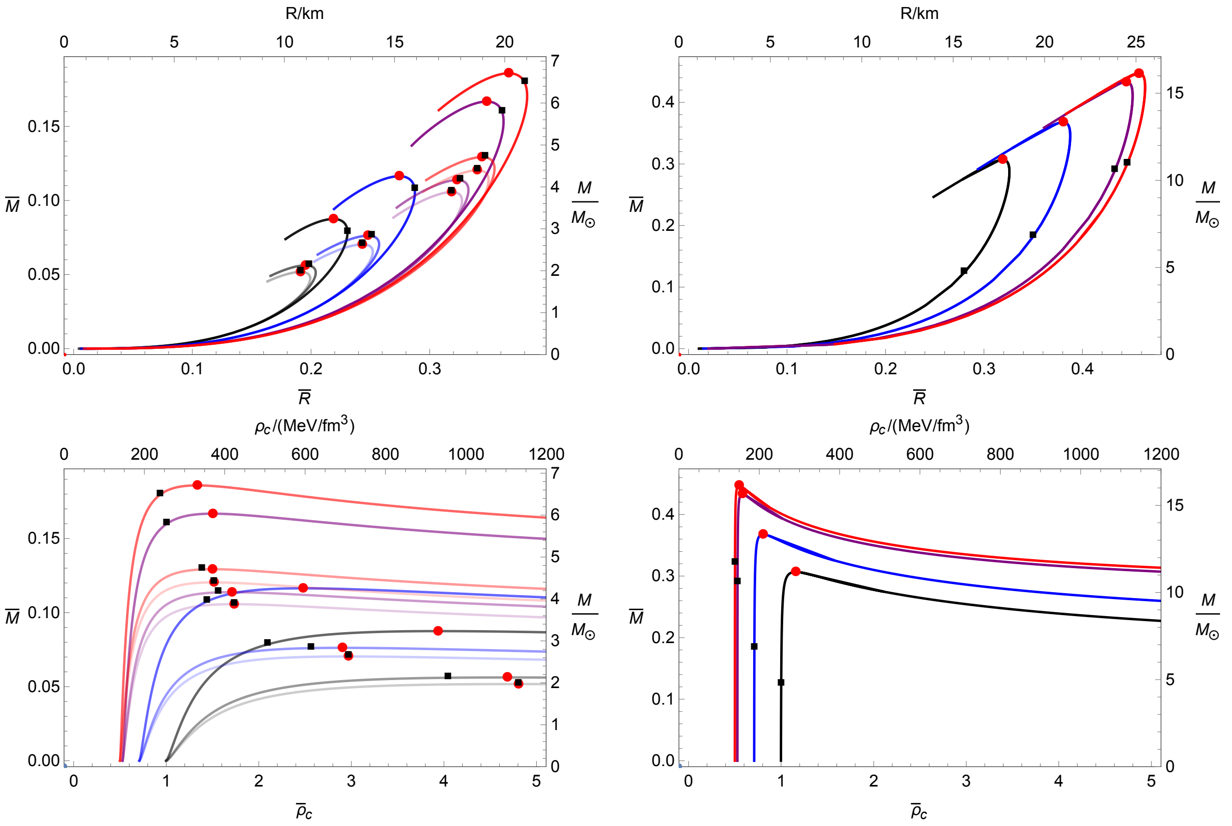

Figure 2.1: Plots of $\bar{M}$ vs. $\bar{R}$ (upper graphs) and $\bar{\rho}_c$ (lower graphs) of charged interacting quark stars in model A for (left) $\alpha = (0, 0.3, 0.7)$ and (right) $\alpha = 0.999$. The right and top axes in each plot are the corresponding dimensional parameters with $B_{\text{eff}} = 60\,\text{MeV}/\text{fm}^3$ for illustration. The black, blue, purple, and red curves respectively denote $\bar{\lambda} = (0, 0.5, 10, \infty)$ with the sign of λ being positive. Darker shades correspond to increasing values of α. The solid dots denote the maximum mass configurations, with the filled squares denoting where $\bar{\omega}_0^2 = 0$.

We see that a larger α and $\bar{\lambda}$ result in a larger mass and radius in the $\bar{M}$-$\bar{R}$ plots, and lead to a stiffer slope for the $\bar{M}$-$\bar{\rho}_c$ curves yielding a smaller central density at the maximum mass point. Note that the location of $\bar{\rho}_c$ at $\bar{M} = 0$ is predicted by eq (1.56) with the pressure P set to zero. We also see that if $\alpha \neq 0$ the maximum mass points and the $\bar{\omega}_0^2 = 0$ points are not coincident, with the latter occurring for smaller central densities. This is particularly evident in the lower two diagrams of Fig. 2.1, where we see that the stability point $\bar{\omega}_0^2 = 0$ occurs for smaller values of $\bar{\rho}_c$ than the maximum mass point, with the size of the separation in mass between these two points becoming larger with increasing α, and the separation size in density becoming smaller with increasing $\bar{\lambda}$.

2.3.2 Model B

We depict the mass/radii curves for interacting quark stars with model B-type charge configurations in Fig. 2.2. As before, both increasing $\bar{\lambda}$ and increasing charge enlarge the mass and radius of the star, and lead to a stiffer slope for the $\bar{M}$-$\bar{\rho}_c$ curves resulting in a smaller central density at the maximum mass point. However, we see here that the stability point $\bar{\omega}_0^2 = 0$ now occurs for larger values of $\bar{\rho}_c$ than the maximum mass point, with the sizes of the mass separation and the density separation between these two points both becoming larger with increasing $\bar{\beta}$. Interestingly, we find the density separation size first gets rapidly larger, then slowly becomes smaller as $\bar{\lambda}$ increases. For sufficiently large $\bar{\beta}$ and $\bar{\lambda}$ there are no stability points, and the configurations are radially unstable for all central densities, as shown in the upper two curves in the right diagrams of Fig. 2.2.

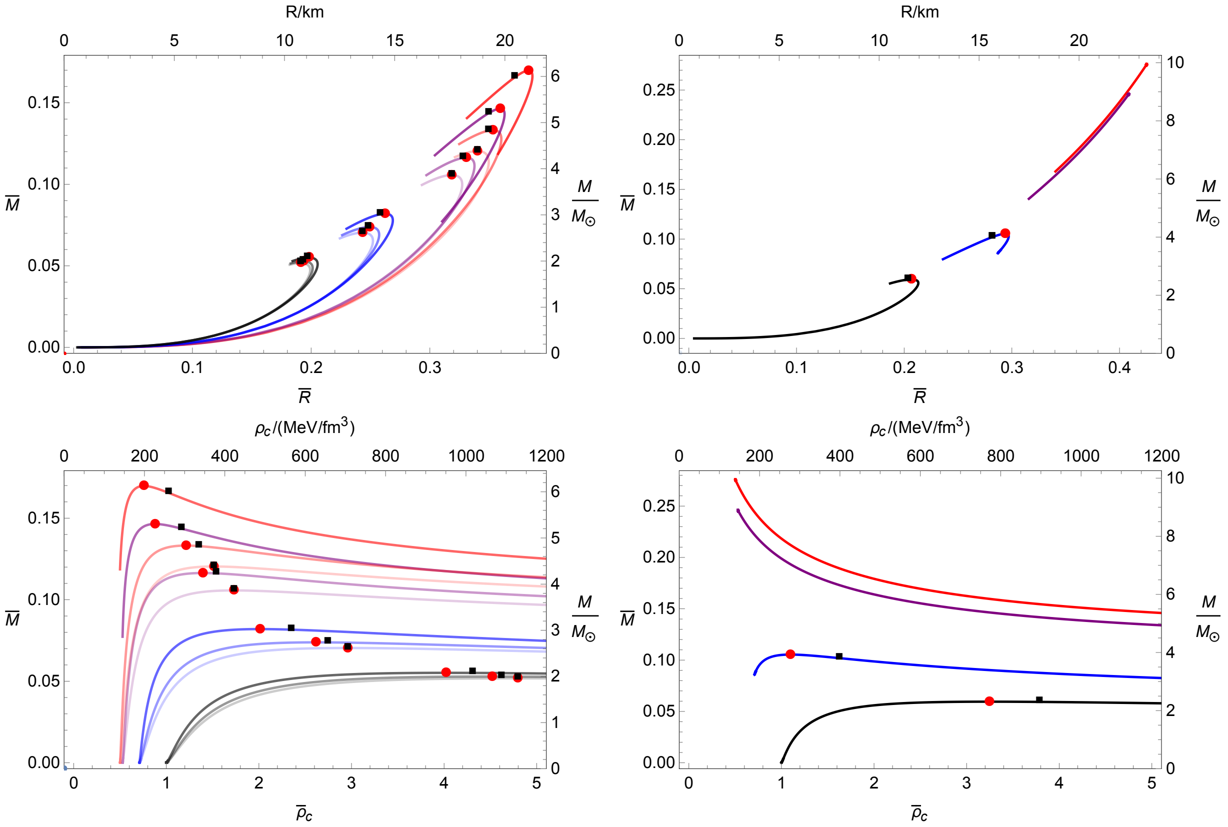

Figure 2.2: Plots of $\bar{M}$ vs. $\bar{R}$ (upper graphs) and $\bar{\rho}_c$ (lower graphs) of charged interacting quark stars in model B for (left) $\bar{\beta} = (0, 1.5, 2.5)$ and (right) $\bar{\beta} = 3.5$. The right and top axes in each plot are the corresponding dimensional parameters with $B_{\text{eff}} = 60\,\text{MeV/fm}^3$ for illustration. The black, blue, purple, and red curves respectively denote $\bar{\lambda} = (0, 0.5, 10, \infty)$ with the sign of λ being positive. Darker shades correspond to increasing values of $\bar{\beta}$. The solid dots denote the maximum mass configurations, with the filled squares denoting where $\bar{\omega}_0^2 = 0$. In the right diagrams, the configurations denoted by the purple and red curves are radially unstable for all central densities.

Another interesting feature for large $\bar{\beta}$ and large $\bar{\lambda}$ configurations is that stellar structures with nearly zero central pressure have non-zero radii and masses (i.e., $\bar{M}$-$\bar{R}$ curves do not start from the origin). This can be seen from the pressure profile plots shown in Fig. 2.3. In contrast to normal cases where $\bar{P}(\bar{r})$ decreases with increasing $\bar{r}$ monotonically as shown in Fig. 2.3a, we see in Fig. 2.3b that for some large $(\bar{\lambda}, \bar{\beta})$ sets, $\bar{P}(\bar{r})$ grows first before it decreases with r, resulting in a finite radius even at a tiny central pressure.

This is because the mass density or the corresponding pressure profile has to grow (over $\bar{r}$) first to counterbalance the effect of a rapidly growing charge density when $\bar{\beta}$ is large enough.

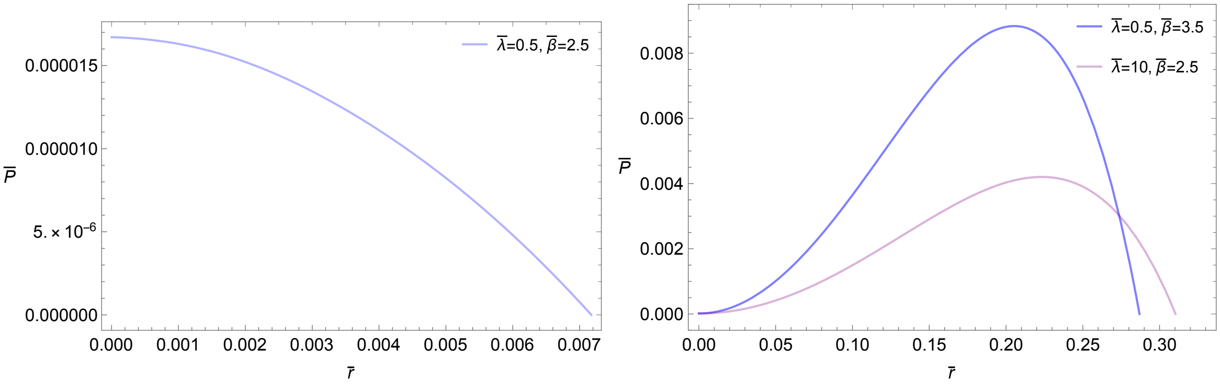

Figure 2.3: $\bar{P}$-$\bar{r}$ plots of charged interacting quark stars in model B for (a) $(\bar{\lambda}, \bar{\beta}) = (0.5, 2.5)$ and (b) $(\bar{\lambda}, \bar{\beta}) = (0.5, 3.5), (10, 2.5)$ with a tiny rescaled central pressure $\bar{P} = 0.00001671$.

Therefore, the critical value of β for which such a transition at near-zero central pressure takes place is a result of the competition between gravitational and electrostatic forces at the origin. This can be described as

$$M_{r\to 0} = Q_{r\to 0} \Rightarrow \rho_0 \frac{4\pi}{3} r^3 = \beta_c r^3 \Rightarrow \beta_c = \frac{4\pi}{3}\rho_0 \tag{2.7}$$

where $\rho_0 = \rho(r = 0)$. Rescaling this into dimensionless form using (1.49) and ((2.5)) and inserting it into the rescaled EOS eq (1.56), we obtain

$$\bar{\beta}_c = \frac{4\pi}{3}\left(3\bar{P}_0 + 1 - \frac{4}{\pi^2}\bar{\lambda}\left(-1 + \sqrt{1 + \frac{\pi^2}{\bar{\lambda}}(\bar{P}_0 + \frac{1}{4})}\right)\right). \tag{2.8}$$

As the central pressure $\bar{P}_0 \to 0$ we have

$$\bar{\beta}_{c0} = \frac{4\pi}{3}\left(1 - \frac{1}{1 + \sqrt{1 + \pi^2/(4\bar{\lambda})}}\right) \tag{2.9}$$

and we see that larger $\bar{\lambda}$ results in a smaller $\bar{\beta}_{c0}$, with the smallest value $\bar{\beta}_{c0} = 2\pi/3 \approx 2.094$ achieved for $\bar{\lambda} \to \infty$, and the largest value $\bar{\beta}_{c0} = 4\pi/3 \approx 4.189$ achieved for $\bar{\lambda} = 0$.

This explains the finite $(\bar{M},\bar{R})$ values at zero central pressure for large $\bar{\beta}$ and large $\bar{\lambda}$ shown in figures 2.2 and 2.3.

For very large $\bar{\beta}$ and $\bar{\lambda}$ values, we find configurations radially unstable for all central densities, as denoted by the purple and red curves in the graphs on the right column of figure 2.2.

2.3.3 Model C

In this case we fix the total charge, whose actual values are chosen to be commensurate with the previous two charge configurations. The corresponding results are obtained by enumerating the charge configurations (like model B[1]) and central densities that yield the chosen fixed charge value for a given $\bar{\lambda}$. We illustrate the results in Fig. 2.4, where we successively chose $\bar{Q} = (0, 1.538, 3.076) \times 10^{-2}$, corresponding to $Q = (0, 1, 2) \times 10^{20} C$ for a typical bag constant value $B_{\text{eff}} = 60\,\text{MeV/fm}^3$.

As before, both increasing $\bar{\lambda}$ and increasing charge enlarges the mass and radius of the star, and leads to a stiffer slope for the $\bar{M}$-$\bar{\rho}_c$ curves, yielding a smaller central density at the maximum mass point. Interestingly, similar to model B, the stellar structure with nearly zero central pressure has non-zero radii and masses (i.e., $\bar{M}$-$\bar{R}$ curves do not start from the origin). This can be understood in the sense that, for a fixed $\bar{Q}$, a small radius requires a very large $\bar{\beta}$ since $\bar{Q} = \bar{\beta}\bar{r}^3$, yet our previous discussion of model B has shown both numerically and analytically that very large $\bar{\beta}$ cases can not have radii close to the origin.

We can see that a larger charge pushes the $\bar{\omega}_0^2 = 0$ point to smaller central densities than that of the maximum mass point, in contrast to an earlier investigation for charged strange quark stars in the context of the MIT bag model [102], but in accord with a more recent investigation of these objects with an interacting EOS [101]. Interestingly, we observe that a larger $\bar{\lambda}$ tends to move the $\bar{\omega}_0^2 = 0$ point closer to the maximum mass point. This means that for a fixed total charge, strong interaction effects tend to offset charge destabilization effects on radial stability (as expected from the confining nature of the strong interaction).

---

[1] We find for the same fixed charges, that the results for $(\bar{M},\bar{R})$ derived from model A differ from those of model B on the order of 0.1%-1%, with the former having slightly larger maximum masses.

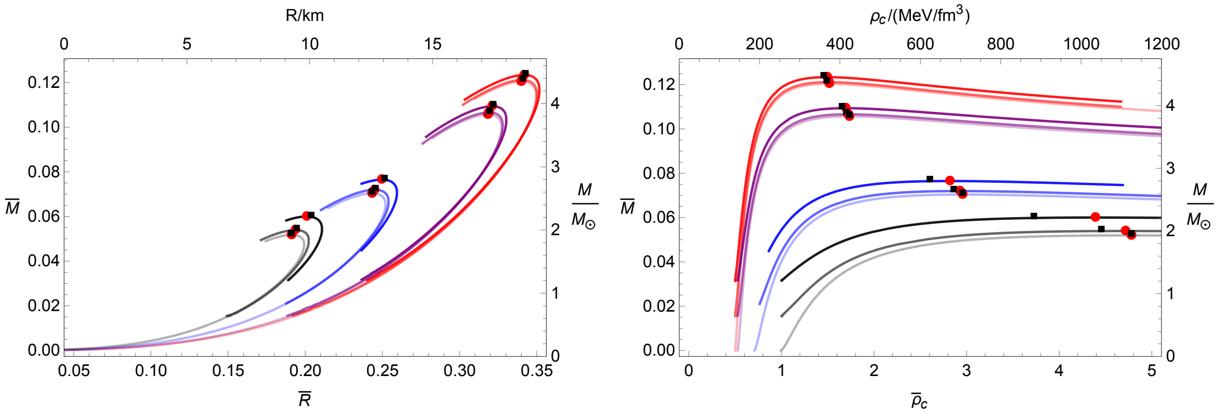

Figure 2.4: $\bar{M}$-$\bar{R}$ (left) and $\bar{M}$-$\bar{\rho}_c$ (right) plots of charged interacting quark stars for $\bar{Q} = (0, 1.538, 3.076) \times 10^{-2}$. The right and top axes in each plot are the corresponding dimensional parameters with $B_{\text{eff}} = 60\,\text{MeV/fm}^3$ for illustration. The black, blue, and purple curves respectively denote $\bar{\lambda} = (0, 0.5, 10)$ with the sign of λ being positive. Red curves are with $\bar{\lambda} = \infty$. Darker shades correspond to increasing values of $\bar{Q}$. The solid dots denote the maximum mass configurations, with filled squares denoting where $\bar{\omega}_0^2 = 0$.

2.4 Results for Negative λ

In this section we present the results of the stellar structure and radial stability equations for charged interacting quark stars with a negative interaction coefficient λ. This condition corresponds to $\Delta^2/m_s^2 < \xi_{2b}/\xi_{2a}$, where again Δ is the gap parameter, m_s is the strange quark mass, and ξ_{2a}/ξ_{2b} are the constants from equation (1.55), characterizing the phases of colour superconductivity - an increasingly negative λ softens the equation of state. Figure 2.5, figure 2.6, and figure 2.7 are associated with charge configurations of models A, B, and C, respectively.

First, in all of these figures, we observe that the effect of charge is still to lift the mass and radius. However, in contrast to the positive λ cases, here a larger $\bar{\lambda}$ results in a smaller mass and radius, and leads to a softer slope for the $\bar{M}$-$\bar{\rho}_c$ curves, resulting in a larger central density at the maximum mass point. This is as expected, considering a larger $\bar{\lambda}$ corresponds to a softer EOS when λ is negative. We also note that for the model B here, $\bar{M} - \bar{R}$ and $\bar{M} - \bar{\rho}_c$ curves with different $\bar{\beta}$ tend to overlap for a larger $\bar{\lambda}$, which explains why we only observe only one purple curve in figure 2.6.

Comparing figure 2.6 to fig. 2.2 for the same model B-type charge configurations, we can see another obvious difference to the positive λ cases - now all of the curves for model B *do* start from the origin $(\bar{M}, \bar{R}) = (0, 0)$. This is because when the sign of λ turns negative, the sampled $\bar{\beta}$ now (≤ 3.5) is not large enough to exceed the critical beta $\bar{\beta}_{c0}$ in (2.8). To be more explicit, restoring the $\mathrm{sgn}(\lambda)$ factor in front of the square root term in equation (2.8), equation (2.9) from the positive λ cases then converts to

$$\bar{\beta}_{c0} = \frac{4\pi}{3}\left(1 - \frac{1}{1 - \sqrt{1 + \pi^2/(4\bar{\lambda})}}\right) \tag{2.10}$$

for the negative λ cases. Then for $\bar{\lambda} = (0.5, 10)$ we obtain respectively $\bar{\beta}_{c0} \approx (7.11, 40.12)$, which are well above the sampled $\bar{\beta}$ values used in figure 2.6. We also see that now a larger $\bar{\lambda}$ maps to a larger $\bar{\beta}_{c0}$, in contrast to the positive λ cases discussed under equation (2.9).

Finally, from the results of radial stability, we see that the relative positions of the $\bar{\omega}_0^2 = 0$ and the maximum mass points are similar to those in the positive λ cases, i.e., the $\bar{\omega}_0^2 = 0$ point can occur at a larger density than that of the maximum mass point for model B, while the opposite is true for model A and model C. Similar to the positive λ cases, a larger charge configuration results in a larger separation between the two points. In opposition to the positive λ case, for model A and model C, a larger $\bar{\lambda}$ shifts the relative position of the $\bar{\omega}_0^2 = 0$ point to be further from the maximum mass point, whereas these two points are closer for model B.

We find that less negative values of λ map to a decreased density separation size of the two points for models A and C, and an enlarged separation size for model B, which decreases once λ becomes sufficiently large.

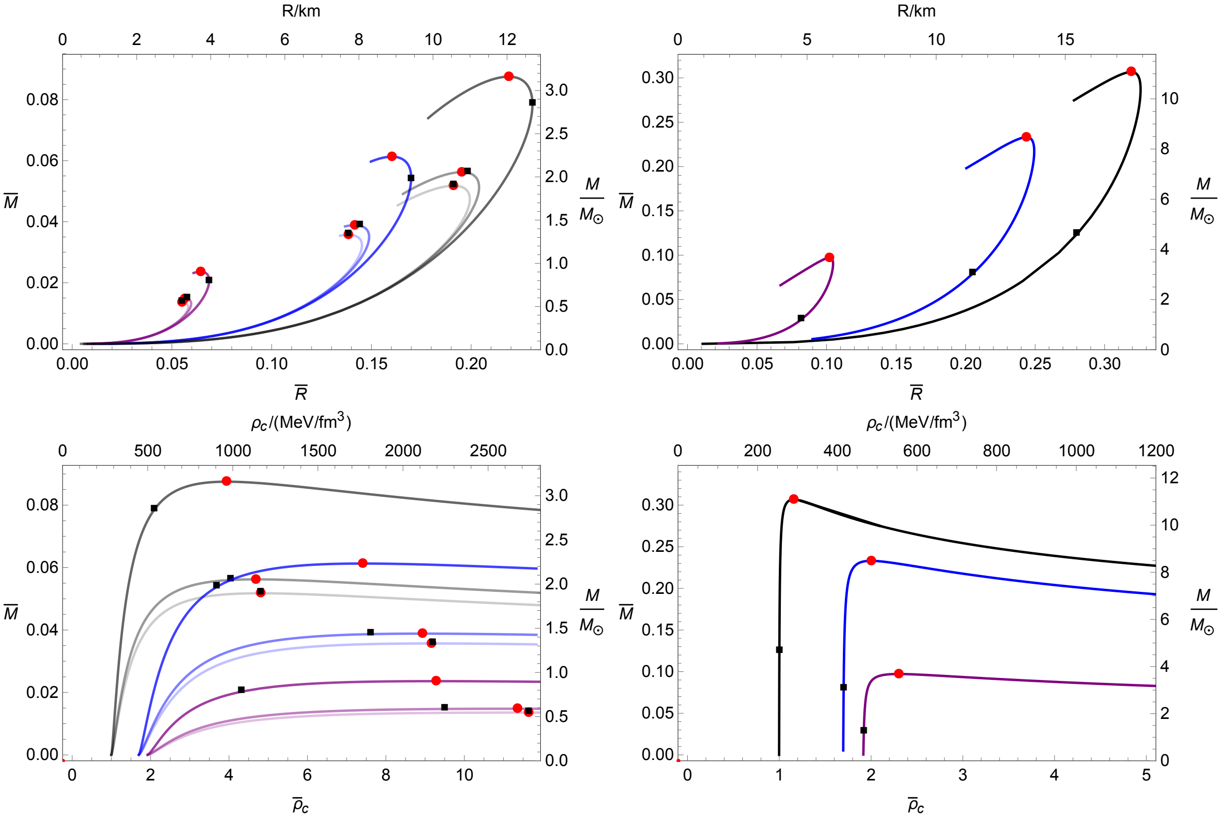

Figure 2.5: Plots of $\bar{M}$ vs. $\bar{R}$ (upper graphs) and $\bar{\rho}_c$ (lower graphs) of charged interacting quark stars in model A for (left) $\alpha = (0, 0.3, 0.7)$ and (right) $\alpha = 0.999$. The right and top axes in each plot are the corresponding dimensional parameters with $B_{\rm eff} = 60\,{\rm MeV/fm^3}$ for illustration. The black, blue, and purple curves respectively denote $\bar{\lambda} = (0, 0.5, 10)$ with the sign of λ being negative. Darker shades correspond to increasing values of α. The solid dots denote the maximum mass configurations, with the filled squares representing where $\bar{\omega}_0^2 = 0$. Note that for the purple curves in the $\bar{M} - \bar{\rho}_c$ plots, we rescaled the axis as $\bar{\rho}_c \to \bar{\rho}_c/5$ for a clear illustration.

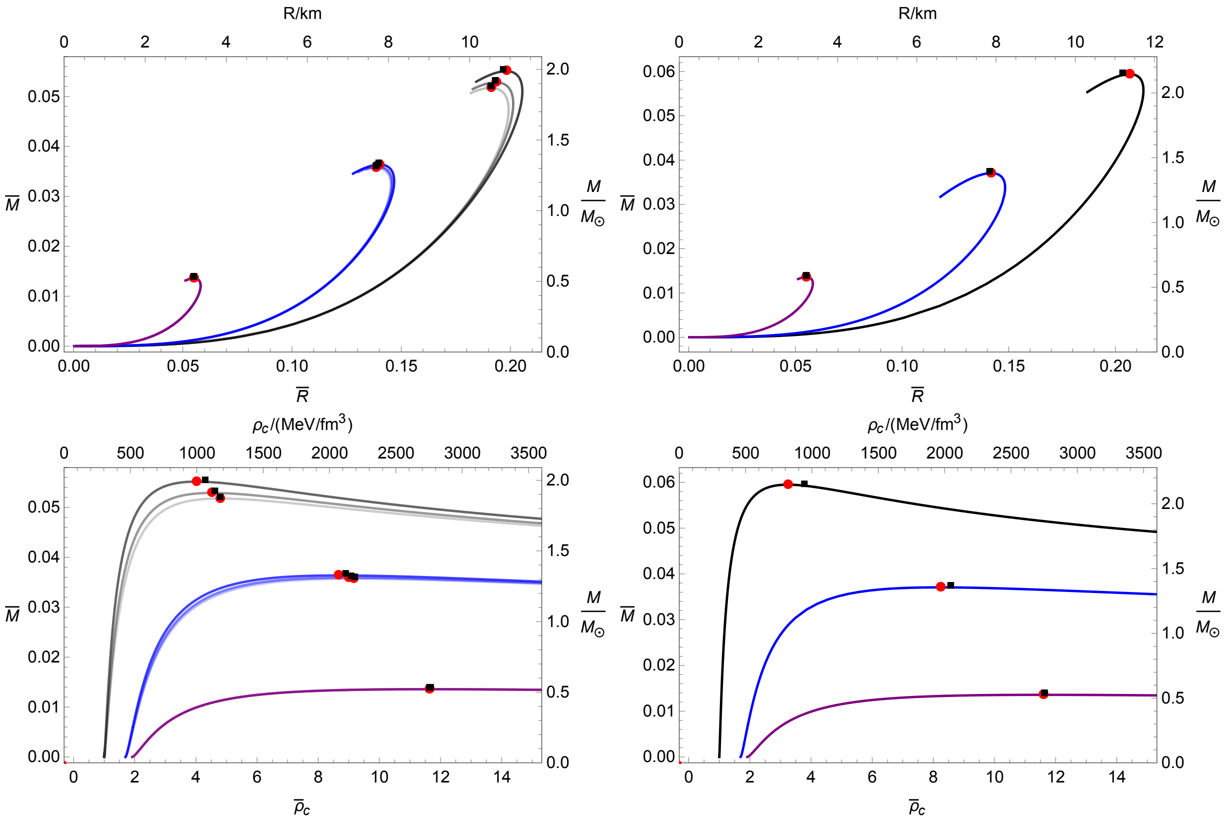

Figure 2.6: Plots of $\bar{M}$ vs. $\bar{R}$ (upper graphs) and $\bar{\rho}_c$ (lower graphs) of charged interacting quark stars in model B for (left) $\bar{\beta} = (0, 1.5, 2.5)$ and (right) $\bar{\beta} = 3.5$. The right and top axes in each plot are the corresponding dimensional parameters with $B_{\text{eff}} = 60\,\text{MeV/fm}^3$ for illustration. The black, blue, and purple curves respectively denote $\bar{\lambda} = (0, 0.5, 10)$ with the sign of λ being negative. Darker shades correspond to increasing values of $\bar{\beta}$. The solid dots denote the maximum mass configurations, with the filled squares representing where $\bar{\omega}_0^2 = 0$. Note that for the purple curves in the $\bar{M} - \bar{\rho}_c$ plots, we rescaled the axis as $\bar{\rho}_c \to \bar{\rho}_c/5$ for a clear illustration.

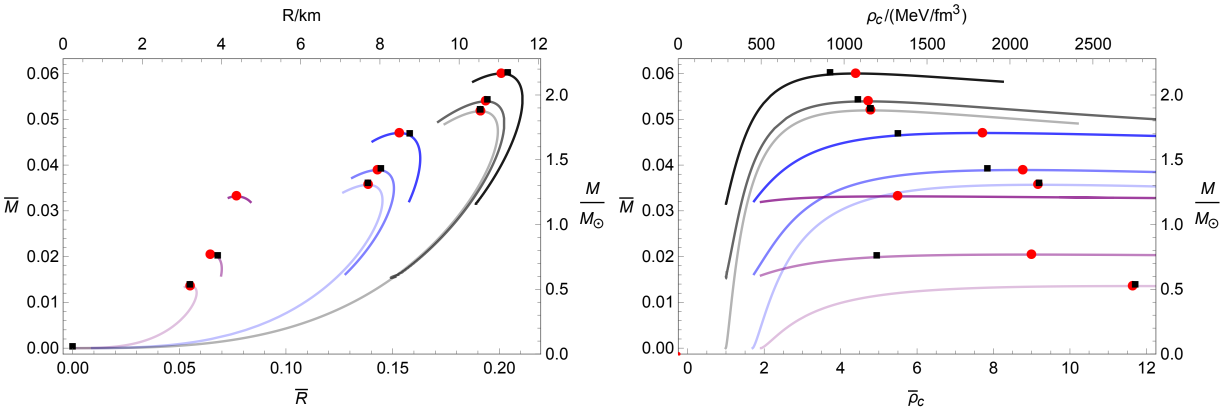

Figure 2.7: $\bar{M}$-$\bar{R}$ (left) and $\bar{M}$-$\bar{\rho}_c$ (right) of charged interacting quark stars for $\bar{Q} = (0, 1.538, 3.076) \times 10^{-2}$. The right and top axes in each plot are the corresponding dimensional parameters with $B_{\text{eff}} = 60\,\text{MeV/fm}^3$ for illustration. The black, blue, and purple curves respectively denote $\bar{\lambda} = (0, 0.5, 10)$ with the sign of λ being negative. Darker shades correspond to increasing values of $\bar{Q}$. The solid dots denote the maximum mass configurations, with filled squares denoting where $\bar{\omega}_0^2 = 0$. Note that for the purple curves in the $\bar{M} - \bar{\rho}_c$ plots, we rescaled the axis as $\bar{\rho}_c \to \bar{\rho}_c/5$ for a clear illustration.

2.5 Summary

In this chapter we examined the stellar structure and the radial stability of charged quark stars with different charge configurations and a unified interacting quark matter EOS, depending only on $(B_{\text{eff}},\, \lambda = (\xi_{2a}\Delta^2 - \xi_{2b}m_s^2)/\sqrt{\xi_4 a_4})$ or $\bar{\lambda} = \lambda^2/4B_{\text{eff}}$. In general, a larger charge profile tends to increase the stellar masses and radii. A larger $\bar{\lambda}$ also increases the mass and radius when λ is positive, with the opposite holding for negative λ. For the charge model with $q = \beta r^3$, we have numerically and analytically identified a new stellar structure with a finite radius at zero center pressure. This exotic structure is more prominent for larger charge and larger (smaller) $\bar{\lambda}$ for positive (negative) λ. Model C (fixed charge Q) shows a similar exotic structure since otherwise the results will be inconsistent with those of model B.

Determining the radial stability by identifying the zero eigenfrequencies of the fundamental oscillation mode ($\bar{\omega}_0^2 = 0$), we observe that stable structures can occur beyond the maximum mass point for model B, while the opposite is true for models A and C, with a larger mass separation size (between the maximum mass point and the $\bar{\omega}_0^2 = 0$ point) for a larger charge configuration.

We find that an increasingly positive λ tends to decrease the density separation size of the two critical points for models A and C, whereas this separation for model B becomes larger, until λ becomes sufficiently large, after which it decreases. This indicates that a large λ, which maps to a large Δ or small m_s for a given a_4, tends to offset the opposite effects of charge on the star's radial stability.

Chapter 3

Slowly Rotating Black Holes in 4D Gauss-Bonnet Gravity

3.1 Introduction

Since the recent derivation of a well-defined $D \to 4$ limit for 4D Gauss-Bonnet (4DGB) gravity, there has been considerable interest in testing it as an alternative to Einstein's general theory of relativity. In this chapter, we construct slowly rotating black hole solutions of 4DGB gravity in asymptotically flat, de Sitter, and anti-de Sitter spacetimes. At leading order in the rotation parameter, exact solutions of the metric functions are derived and studied for all three of these cases. We compare how physical properties (innermost stable circular orbits, photon rings, black hole shadow, etc.) of the solutions are modified by varying coupling strengths of the 4DGB theory relative to standard Einstein gravity results. We find that a vanishing or negative cosmological constant in the 4DGB theory enforces a minimum mass on the black hole solutions, whereas a positive cosmological constant enforces both a minimum *and* maximum mass with a horizon root structure directly analogous to the Reissner-Nordström de Sitter spacetime. Besides this, many of the physical properties are similar to General Relativity, with the greatest deviations being found in the low mass regime.

3.1.1 Metric Functions

To construct slowly rotating solutions for the new 4DGB theory, we begin by substituting $x = \cos\theta$ into equation (1.20), yielding:

$$ds^2 = -f(r)dt^2 + \frac{dr^2}{h(r)} + 2ar^2 p(r)(1-x^2)dt d\phi + r^2\left[\frac{dx^2}{1-x^2} + (1-x^2)d\phi^2\right] \tag{3.1}$$

where a is a small parameter governing the rate of rotation. Of particular interest are Schwarzschild-like solutions where $h(r) = f(r)$. Inserting this into the equations of motion eqs. (1.81) and (1.82) and considering the combination $\mathcal{E}_0^0 - \mathcal{E}_1^1$, we derive the following equation for the scalar field

$$(\phi'^2 + \phi'')(1 - (r\phi' - 1)^2 f) = 0 \tag{3.2}$$

which admits either the solution $\phi = \ln(\frac{r-r_0}{l})$ (with r_0, l integration constants), or the solutions

$$\phi_\pm = \int \frac{\sqrt{f} \pm 1}{\sqrt{f} r} dr, \tag{3.3}$$

where we choose the latter solution with a minus sign, which reproduces Glavan & Lin's [29] metric function, and falls off as $1/r$ when $\Lambda = 0$. Using (3.2) we can solve for the metric function $f(r)$ from the geometric expression (1.83). It can easily be shown that

$$r^2(1 - f(r)) - \frac{\Lambda r^4}{3} + \alpha f(r)^2 - 2\alpha f(r) - \alpha C_2 r + C_1 = 0. \tag{3.4}$$

As we wish to recover the Schwarzschild-AdS solution when $\alpha = 0$, we set $C_1 = \alpha$ and $C_2 = \frac{2M}{\alpha}$ yielding

$$f_\pm = 1 + \frac{r^2}{2\alpha}\left(1 \pm \sqrt{1 + \frac{8\alpha M}{r^3} + \frac{4}{3}\alpha\Lambda}\right) \tag{3.5}$$

where the f_- (or Einstein) branch is yields the Schwarzschild AdS solution in the limit $\alpha \to 0$. From here it is straightforward to show that ϕ_- falls of as $1/r$ when $\Lambda = 0$, whereas all other solutions for ϕ diverge logarithmically at large r.

Remarkably the solution (3.5) is still valid to leading order in a. The only remaining independent equation from (1.82) to this order is given by $\mathcal{E}_{03}$:

$$rp''\left(24\alpha M + r^3(4\alpha\Lambda + 3)\right) + 4p'\left(15\alpha M + r^3(4\alpha\Lambda + 3)\right) = 0 \tag{3.6}$$

and admits the exact solution

$$p = C_2 - C_1 \frac{\sqrt{1 + \frac{4\alpha M}{r^3} + \frac{4}{3}\alpha\Lambda}}{12\alpha M}. \tag{3.7}$$

Requiring that this match the Kerr-AdS metric function p in the large r limit, we set $C_1 = 2\sqrt{3}M\sqrt{4\alpha\Lambda + 3}$ and $C_2 = \frac{10\alpha\Lambda+3}{6\alpha}$. This leaves us with the final expression

$$p(r) = \frac{5}{3}\Lambda + \frac{1}{2\alpha}\left[1 - \sqrt{1 + \frac{4\alpha\Lambda}{3}}\sqrt{1 + \frac{4\alpha}{3}\left(\Lambda + \frac{6M}{r^3}\right)}\right] \tag{3.8}$$

which, in the $\Lambda = 0$ limit, matches[1] the result found in [37] for asymptotically flat spacetime.

3.1.2 Analytic Properties

The slowly rotating 4DGB metric (3.1), with p given by (3.8) and $f = h$ given by (3.5), is singular near $r = 0$, which can be seen by computing the Ricci scalar to lowest order in r. In doing so we find that

$$R(r)_{r\to 0} \sim \frac{15}{4}\sqrt{\frac{2M}{\alpha r^3}} \tag{3.9}$$

regardless of the value of Λ. In this work, we only consider solutions where this singularity is obscured behind a horizon. The only other condition leading to a divergence in R is

$$4\alpha\Lambda + \frac{24\alpha M}{r^3} + 3 = 0 \tag{3.10}$$

which is never true in the allowed region of α/Λ parameter space (see section 3.2). Therefore the 4DGB metric is regular everywhere but the black hole singularity. Computed explicitly to leading order in the rotation parameter, the Kretschmann scalar is

$$K = f''(r)^2 + \frac{4f'(r)^2}{r^2} + \frac{4(f(r) - 1)^2}{r^4}. \tag{3.11}$$

For black hole solutions, the scalar field (3.3) is ill-defined inside the horizon where $f(r) < 0$. Such solutions can be made regular across the horizon as was shown in [37],

---

[1] up to an errant factor of the rotation parameter included in their metric function

although we focus on exterior solutions for the remainder of this work.

The structure of the field equations is such that everything can be rescaled into a unitless form, relative to some length scale. Writing

$$\Lambda = \pm \frac{3}{L^2} \tag{3.12}$$

where the positive and negative branches correspond to de Sitter and anti-de Sitter space respectively, and L is the Hubble length. With this, we perform the rescalings:

$$\alpha \to \bar{\alpha} L^2 \qquad M \to \bar{M} L \qquad r \to \bar{r} L \qquad a \to \bar{a} L \tag{3.13}$$

in terms of the Hubble length L.

For a non-vanishing cosmological constant, the 4DGB metric functions become

$$\bar{f}(\bar{r}) = 1 + \frac{\bar{r}^2}{2\bar{\alpha}} \left(1 - \sqrt{1 \pm 4\bar{\alpha} + \frac{8\bar{\alpha}\bar{M}}{\bar{r}^3}} \right) \tag{3.14}$$

and $r^2 p(r) \to \bar{r}^2 \bar{p}(\bar{r})$, where

$$\bar{p}(\bar{r}) = \pm 5 + \frac{1}{2\bar{\alpha}} \left(1 - \sqrt{1 \pm 4\bar{\alpha}} \sqrt{1 \pm 4\bar{\alpha} + \frac{8\bar{\alpha}\bar{M}}{\bar{r}^3}} \right). \tag{3.15}$$

If instead we are working in an asymptotically flat spacetime, one can directly set $\Lambda = 0$ in eqs. (3.5) and (3.8).

3.2 Properties of the Solution

In this section we study physical properties of the solutions derived above. We discuss the location and angular velocity of the black hole horizons, the equatorial geodesics (innermost stable circular orbit, photon rings, and associated Lyapunov exponents), and the black hole shadow. In each case we compare the properties of the 4DGB solution for multiple values of the coupling constant to the analogous GR result, and discuss how the higher order contributions affect these properties.

3.2.1 Location and Angular Velocity of the Black Hole Horizons

The angular velocity of the black hole horizon is defined as

$$\Omega_h = -\frac{g_{t\phi}}{g_{\phi\phi}}|_{r=r_h} = -ap(r_h) \tag{3.16}$$

where r_h is the radius at which g_{rr} diverges (ie. $f(r_h) = 0$).

To determine the locations of the horizons, it is convenient to rewrite the metric function $f_-(r)$ as

$$f_-(r) = \frac{r^2}{\alpha}\frac{F(r)}{f_+(r)} \tag{3.17}$$

where $F(r) = 1 - \frac{2M}{r} + \frac{\alpha}{r^2} - \frac{1}{3}\Lambda r^2$. The denominator does not vanish, and the horizons are given by the roots of the numerator, which obey the equation

$$\Lambda r_h^4 - 3r_h^2 + 6Mr_h - 3\alpha = 0. \tag{3.18}$$

This equation has exact solutions for all values of Λ.

$\mathbf{\Lambda = 0}$

In asymptotically flat space, (3.18) admits the following simple solutions:

$$r_h = M \pm \sqrt{M^2 - \alpha} \tag{3.19}$$

with r_+ (the outer horizon) recovering the Schwarzschild value as $\alpha \to 0$. Assuming $\alpha > 0$, this equation sets a minimum value for black hole mass in the theory, namely

$$M_{min} = \sqrt{\alpha} \tag{3.20}$$

when $\Lambda = 0$. For smaller masses, the metric function $f(r)$ does not vanish anywhere and thus no horizon exists. These solutions have naked singularities.

Since we have an exact solution for $p(r)$ from (3.8) and a simple analytic form for r_h, the angular velocity of the horizon

$$\Omega_h = a\frac{1 - \sqrt{1 + \frac{8\alpha M}{\left(M+\sqrt{M^2-\alpha}\right)^3}}}{2\alpha} \tag{3.21}$$

is straightforward to compute. In figure 3.1 we plot $\frac{\Omega}{\chi}$ where ($\chi = a/M$) for a variety of values of α alongside the GR solution for comparison. The main new feature introduced by the 4DGB theory is the existence of a maximal angular velocity, indicted by the termination points of the blue curves at any given α, due to the presence of a minimum mass. As α increases, this maximal value decreases.

For a fixed α we observe that the 4DGB theory predicts a significantly larger angular velocity at a given (small) mass than does GR, but quickly converges to the GR result when the mass is large.

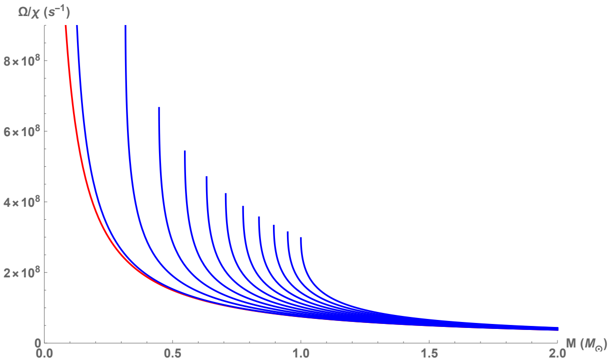

Figure 3.1: Angular velocity of the black hole horizon as a function of mass when $\Lambda = 0$ for $\alpha/M_{\odot}^2 = 0.01, 0.1, 0.2, 0.3, 0.4, 0.5, 0.6, 0.7, 0.8, 0.9, 1$ (in blue from left to right) plotted against the Einstein ($\alpha = 0$) solution $\Omega = \chi/4M$ (in red).

AdS ($\Lambda < 0$)

Solutions to (3.18) yield rather cumbersome expressions for the two different positive values of r_h. For this reason, we solve numerically for the horizon as a function of black hole mass, illustrating the results in figure 3.2a. As in the asymptotically flat case, a minimum mass black hole exists at which the inner and outer horizons merge, given by

$$M_{min} = \frac{\sqrt{1 + 12\alpha\Lambda - \sqrt{(1 - 4\alpha\Lambda)^3}}}{3\sqrt{2\Lambda}} \tag{3.22}$$

which yields (3.20) in the limit $\Lambda \to 0$.

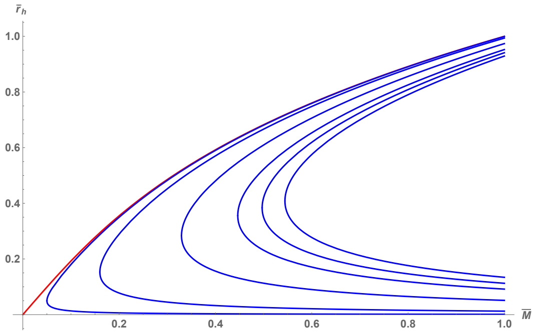

(a) The locations of the anti-de Sitter black hole horizon plotted as a function of mass. The red line represents the solution from GR (ie. when $\alpha = 0$), and the blue lines represent the 4DGB solutions for $\frac{\alpha}{\alpha_C} = 0.01,\ 0.1,\ 0.4,\ 0.7,\ 0.85,\ 1$ from left to right. We see that as soon as a nonzero coupling constant is introduced, the horizon structure includes an inner horizon and a minimum mass point.

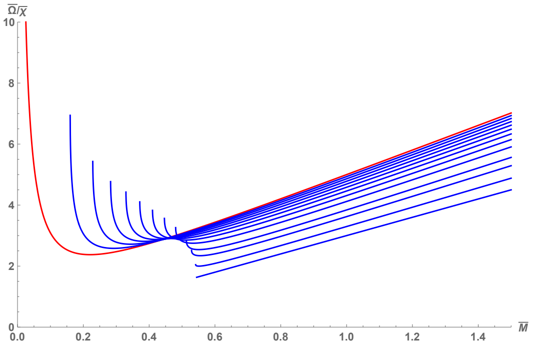

(b) Angular velocity of the black hole horizon in the AdS case as a function of mass for $\frac{\alpha}{\alpha_C} = 0.1,\ 0.2,\ 0.3,\ 0.4,\ 0.5,\ 0.6,\ 0.7,$ $0.8,\ 0.9,\ 0.95,\ 0.99,\ 1$ in blue from left to right, plotted against the Einstein ($\alpha = 0$) solution $\Omega = \chi/4M$ (in red).

There are also upper and lower bounds on the Gauss-Bonnet coupling constant α for any fixed Λ. These are given by the two conditions $4\alpha\Lambda + 3 > 0$ (so that $p(r)$ is real) and $1 - 4\alpha\Lambda > 0$ (so that M_{min} is real). This corresponds to

$$-\frac{3}{4} \leq \alpha\Lambda \leq \frac{1}{4}. \tag{3.23}$$

Since we restrict ourselves to positive values of the 4DGB coupling constant, only one of these inequalities is relevant when Λ is non-zero, depending on its sign. In asymptotically anti-de Sitter space, $\Lambda = -|\Lambda|$ and these inequalities reverse. We can then define a critical value for the coupling constant at its upper limit:

$$\alpha_C = \frac{3}{4|\Lambda|}. \tag{3.24}$$

In figure 3.2b we plot the horizon angular velocity for the AdS case for various allowed values of the coupling constant α. We again observe the existence of a locally maximal angular velocity for $\alpha < \alpha_C$, indicted by the termination points of the blue curves at any given α, due to the presence of a minimum mass. Note that for $\alpha \leq \alpha_C$ the angular velocity also has a global minimum. This occurs at a relatively small value of the mass, and the angular velocity slowly increases again as M increases. When $\alpha = \alpha_C$, this global minima for angular momentum occurs exactly at the minimum allowed mass value.

Another interesting feature is the existence of a crossover mass ($\bar{M}_{\mathrm{x}}$) at which the small α 4DGB solutions become less than the GR solutions. We can find this crossover point analytically for solutions where $\bar{\alpha} << 1$. We begin by fixing a black hole mass, and describe it using both the GR black hole horizon radius ($\bar{r}_{h(GR)}$), and the 4DGB horizon radius ($\bar{r}_{h(GB)}$):

$$2\bar{M} = \bar{r}_{h(\mathrm{GR})} + \bar{r}^3_{h(\mathrm{GR})} = \bar{r}_{h(\mathrm{GB})} + \bar{r}^3_{h(\mathrm{GB})} + \frac{\alpha}{\bar{r}_{h(\mathrm{GB})}}. \tag{3.25}$$

The horizon angular velocity of an Einsteinian black hole can then be written as

$$\frac{\bar{\Omega}_{GR}}{\bar{\chi}} = \frac{\bar{M}(8\bar{M} - 3\bar{r}_{h(\mathrm{GR})})}{2\bar{M} - \bar{r}_{h(\mathrm{GR})}}. \tag{3.26}$$

Similarly, this quantity for a 4DGB black hole can be expanded in a power series in $\bar{\alpha}$:

$$\frac{\bar{\Omega}_{GB}}{\bar{\chi}} = \frac{\bar{M}(8\bar{M} - 3\bar{r}_{h(\mathrm{GB})})}{2\bar{M} - \bar{r}_{h(\mathrm{GB})}} - \frac{2\left(\bar{M}^2(2\bar{M}\bar{r}_{h(\mathrm{GB})} - 1)\right)}{\bar{r}_{h(\mathrm{GB})}(2\bar{M} - \bar{r}_{h(\mathrm{GB})})^2}\bar{\alpha} + \mathcal{O}\left(\bar{\alpha}^2\right). \tag{3.27}$$

Via a quick inspection of figs. 3.2a and 3.2b, it is clear that at at the crossover mass $\bar{M}_{\mathrm{x}}$, $\bar{r}_{h(\mathrm{GB})} \approx \bar{r}_{h(\mathrm{GR})}$, so to 0th order in $\bar{\alpha}$, $\frac{\bar{\Omega}_{GR}}{\bar{\chi}} \approx \frac{\bar{\Omega}_{GB}}{\bar{\chi}}$. The crossover point should then occur when the leading order contribution in (3.27) vanishes, ie. when $2\bar{M}\bar{r}_{h(\mathrm{GB})} - 1 = 0$. As stated above we can replace $\bar{r}_{h(\mathrm{GB})}$ with $\bar{r}_{h(\mathrm{GB})}$ trivially (based on our choice of fixed mass), and can likewise we can use (3.25) to write our fixed mass in terms of $\bar{r}_{h(\mathrm{GR})}$. Finally, we rearrange and solve, yielding a crossover point at:

$$\bar{r}_{h(\mathrm{GR})} = \sqrt{\frac{1}{2}\left(\sqrt{3} - 1\right)} = 0.605 \tag{3.28}$$

which corresponds to a crossover mass of

$$\bar{M}_{\mathrm{x}}^{\bar{\Omega}} \approx 0.413223. \tag{3.29}$$

dS ($\Lambda > 0$)

If $\Lambda > 0$, the 4DGB theory returns three positive solutions to (3.18): r_i (inner), r_o (outer), and r_c (cosmological). The horizon structure is identical to that of the so-called "charged Nariai" solutions in the Reissner-Nordstrom de Sitter metric [127, 128, 129], with the 4DGB coupling parameter α playing a role analogous to that of Q^2, where Q is the total charge. Indeed, upon replacing α with Q, the function $F(r)$ in (3.17) is equivalent to the charged Nariai metric, and asymptotes to [129]

$$F(r) \to 1 - \frac{1}{3}\Lambda r^2 \tag{3.30}$$

as $r \to \infty$.

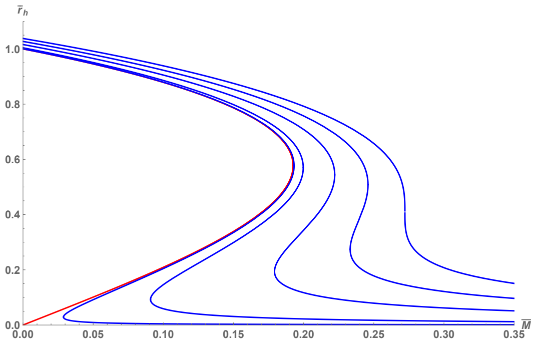

(a) The locations of the de Sitter black hole horizons plotted as a function of mass. In all cases the red line represents the solution from GR (ie. when $\alpha = 0$), and the blue lines represent the 4DGB solutions for $\frac{\alpha}{\alpha_C} = 0.01$, 0.1, 0.4, 0.7, 1 from left to right. We see that as soon as a nonzero coupling constant is introduced the horizon structure includes an inner horizon and a minimum mass point. Once α passes criticality, no physical black hole solutions can exist.

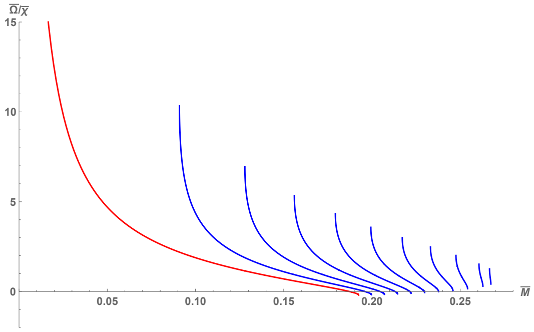

(b) Angular velocity of the black hole horizon as a function of mass in an asymptotically de Sitter spacetime for $\frac{\alpha}{\alpha_C} = 0.1$, 0.2, 0.3, 0.4, 0.5, 0.6, 0.7, 0.8, 0.9, 0.95 in blue from left to right, plotted against the Einstein ($\alpha = 0$) solution $\bar{\Omega} = \bar{\chi}/4\bar{M}$ (in red).

Unlike the asymptotically flat and AdS cases, the de Sitter 4DGB theory enforces both a minimum mass black hole (below which only a naked singularity surrounded by a cosmological horizon exists), and a maximum mass black hole, corresponding to the merging of the outer and cosmological horizons, which is the Nariai solution. We find the location of these extremal mass points to be

$$M_{max/min} = \frac{\sqrt{1+12\alpha\Lambda \pm \sqrt{(1-4\alpha\Lambda)^3}}}{3\sqrt{2\Lambda}} \tag{3.31}$$

which for M_{min} (the minus value) is identical in form to that of the limiting mass for the Reissner–Nordström-de Sitter black hole [129].

From (3.31) we can again set an upper and lower bound on the α parameter for a given Λ:

$$-\frac{3}{4} < \alpha\Lambda < \frac{1}{4}, \tag{3.32}$$

using the same reality criteria as in the AdS case. When α is outside this allowed range we find solution sets that lie in a region of parameter space with no black hole event horizon. Since we restrict ourselves to $\alpha > 0$, we can then define a critical value for the coupling constant in de Sitter from the upper bound

$$\alpha_C = \frac{1}{4|\Lambda|}. \tag{3.33}$$

Armed with an understanding of the de Sitter horizon structure and the allowed regions of parameter space, we solve numerically for the black hole horizon radius and angular velocity, the results of which are plotted in figures 3.3a and 3.3b respectively. Once again we observe that the presence of a minimum mass yields a maximal angular velocity, indicted by the termination points of the blue curves at any given α. Unlike AdS, this extrema at the minimum mass point is a *globally* maximal value for a given coupling constant. In all cases the angular velocity reaches its global minimum at the maximal mass, where for small enough α the angular velocity changes signs near this point. As M increases the allowed range of angular velocity increasingly diminishes, vanishing when $\alpha = \alpha_C$.

3.2.2 Geodesics in the Equatorial Plane

We begin the treatment of equatorial geodesics by setting $x = 0$ ($\theta = \pi/2$) in the metric ansatz (3.1) and multiplying both sides of the line element by $\frac{1}{2}f(r)$, yielding

$$-\frac{\xi f(r)}{2} = -\frac{f(r)^2}{2}\dot{t}^2 + \frac{1}{2}\dot{r}^2 + \frac{1}{2}r^2 f(r)\dot{\phi}^2 + af(r)P(r)\dot{t}\dot{\phi} \tag{3.34}$$

where the overdot refers to a derivative with respect to the affine parameter s, $P(r) = r^2 p(r)$, and ξ is a constant which takes the value 0 or 1, for null and timelike geodesics respectively. Using the static and rotational Killing fields, we know that $E = f(r)\dot{t} - aP(r)\dot{\phi}$ and $j = r^2\dot{\phi} + aP(r)\dot{t}$ are constants of motion along the geodesic, and thus

$$-\frac{1}{2}\xi f(r) = -\frac{1}{2}E^2 + \frac{1}{2}\dot{r}^2 + \frac{j^2 f(r)}{2r^2} - \frac{EP(r)j}{r^2} \tag{3.35}$$

Asymptotically, j^2 represents the total orbital angular momentum of the body following the geodesic. Since we are confined to the equatorial plane, clearly $j^2 = \ell_z^2$ for non-spinning particles. If we rewrite equation (3.35) in the following form

$$\frac{1}{2}\dot{r}^2 + V_{\text{eff}} = 0 \tag{3.36}$$

it becomes clear that

$$V_{\text{eff}} = \frac{f(r)}{2}\left(\frac{\ell_z^2}{r^2} + \xi\right) - \frac{1}{2}E^2 - a\frac{P(r)\ell_z E}{r^2} \tag{3.37}$$

to leading order in the rotation parameter. Note that the rescaled version of this equation is unchanged besides swapping parameters with their barred counterparts. In the following sections we further specialize this analysis by considering the innermost stable circular orbit (or ISCO) for timelike geodesics, and the photon ring for null geodesics.

3.2.3 Timelike Geodesics: Innermost Stable Circular Orbits

For timelike geodesics we set $\xi = 1$ in 3.37. The two conditions for the existence of circular geodesics are

$$V_{\text{eff}}(r) = 0 \qquad V'_{\text{eff}}(r) = 0 \tag{3.38}$$

while the sign of $V''_{\text{eff}}(r)$ dictates the stability of such orbits. Stable orbits are described by $V''_{\text{eff}}(r) > 0$, while $V''_{\text{eff}}(r) < 0$ indicates instability. Since we are interested specifically in the *innermost* stable circular orbit, we shall require $V''_{\text{eff}}(r) = 0$.

Next, we solve these three equations to leading order in the rotation parameter by making the following perturbative expansions

$$\begin{aligned} r_{\text{ISCO}} &= r^{(0)}_{\text{ISCO}} + a r^{(1)}_{\text{ISCO}} \\ j_{\text{ISCO}} &= j^{(0)}_{\text{ISCO}} + a j^{(1)}_{\text{ISCO}} \\ E_{\text{ISCO}} &= E^{(0)}_{\text{ISCO}} + a E^{(1)}_{\text{ISCO}} \,. \end{aligned} \tag{3.39}$$

Substituting these into (3.38) and expanding to leading order in a yields a system of six equations for the six unknowns on the right-hand side of (3.39), which can be solved for numerically.

$\mathbf{\Lambda = 0}$

In this section the numerical results of the aforementioned six equations are plotted as a function of mass for five different values of the coupling constant α, and are compared to the GR solution where $\alpha = 0$. Note that these results correspond with the prograde solutions (namely $j^{(0)}_{ISCO} > 0$), and that an analogous retrograde solution set exists. In all cases we find results similar in form to those from GR, with the greatest deviation from occurring as $M \rightarrow M_{min}$ for any given α. As with the horizons, the 4DGB theory induces a minimum mass black hole for a non-zero coupling constant. One finds that a static black hole described by the 4DGB theory should a have slightly smaller innermost orbital radius, corresponding to a particle with slightly lower angular momentum and energy. The effect of prograde slow rotation in the Einstein case is to subtract slightly from these otherwise positive parameters. The 4DGB rotation corrections act similarly to the GR corrections, but with slightly larger magnitudes (with this difference again being more pronounced near minimum mass).

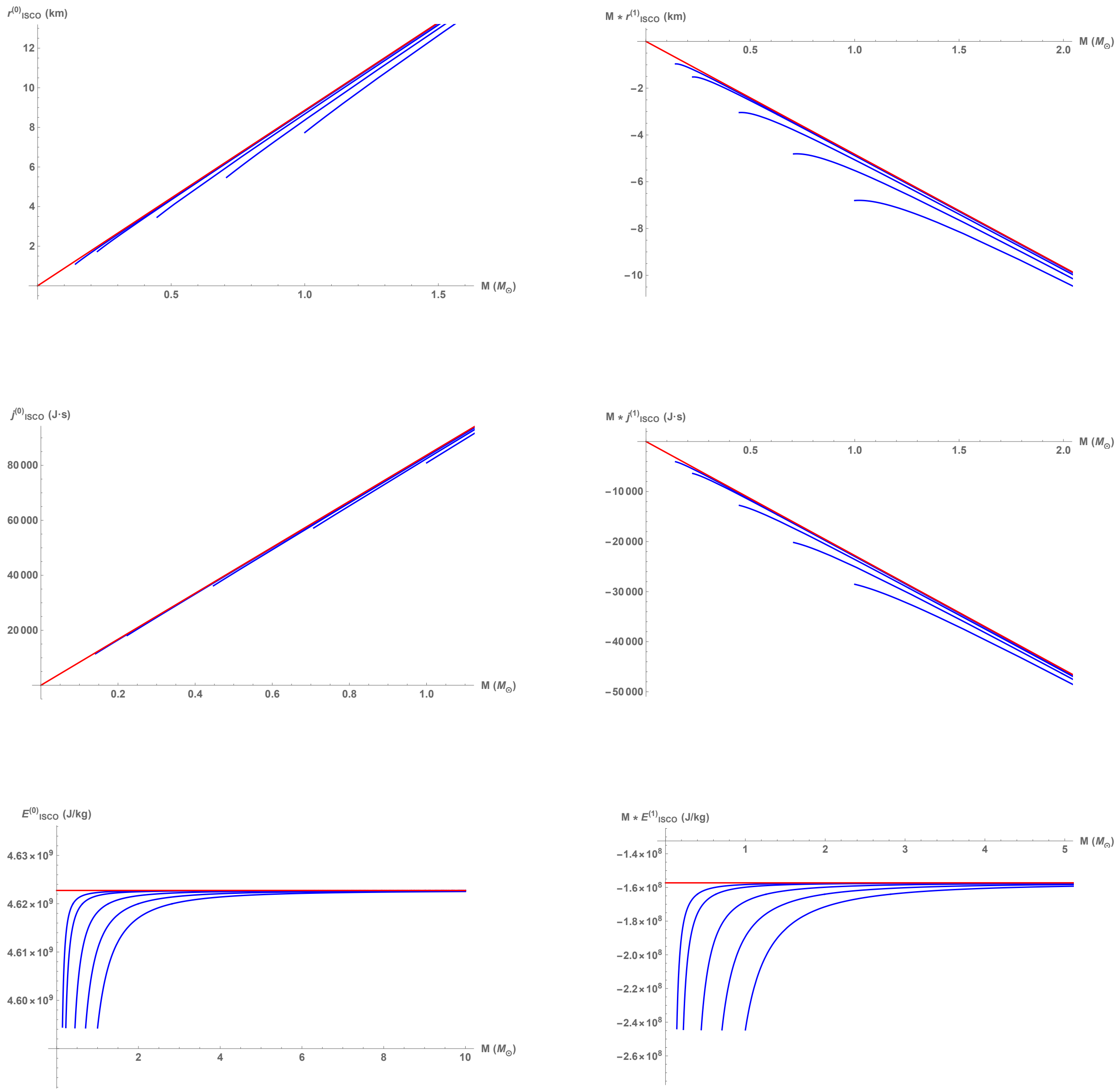

Figure 3.4: Plots of the ISCO parameters when $\Lambda = 0$. The leftmost column contains the 0th order (static) terms, whereas the rightmost column contains the leading order corrections due to rotational effects. In all cases the red line represents the solution from GR (ie. when $\alpha = 0$), and the blue lines represent the 4DGB solutions for $\alpha/M_\odot^2 = 0.02$, 0.05, 0.02, 0.50, 1.0 from left to right.

AdS ($\Lambda < 0$)

In figures 3.5 and 3.6 we plot the results for the ISCO parameters for $\Lambda = -\frac{3}{L^2}$. Recalling the AdS criticality condition (3.24), we cover a range from $\alpha = 0$ (GR) to $\alpha \to \alpha_C$. When α is outside this allowed range we find solution sets for the ISCO which lie in the region of parameter space with no physical event horizon.

When α is small, all 0th order ISCO parameters (figure 3.5) start below the GR solution and become larger at some constant critical mass. We can find this crossover point for $\bar{r}^{(0)}_{ISCO}$ by expanding the nontrivial contribution to ${V''_{\text{eff}}}^{(0)}(r)$ as a power series in α (where $V''_{\text{eff}}(r) = {V''_{\text{eff}}}^{(0)}(r) + a{V''_{\text{eff}}}^{(1)}(r)$), since $\bar{r}^{(0)}_{ISCO}$ is uniquely decided by this parameter. In doing so we find

$$\begin{aligned} {V''_{\text{eff}}}^{(0)}(r) = &- 2\left[6\bar{M}^2(\bar{r}^{(0)}_{ISCO})^3 + 15\bar{M}(\bar{r}^{(0)}_{ISCO})^6 - \bar{M}(\bar{r}^{(0)}_{ISCO})^4 - 4(\bar{r}^{(0)}_{ISCO})^7\right] \\ &- 2\left[60\bar{M}^3 + 120\bar{M}^2(\bar{r}^{(0)}_{ISCO})^3 - 32\bar{M}^2(\bar{r}^{(0)}_{ISCO}) - 75\bar{M}(\bar{r}^{(0)}_{ISCO})^6\right. \\ &\left. - 58\bar{M}(\bar{r}^{(0)}_{ISCO})^4 + 28(\bar{r}^{(0)}_{ISCO})^7\right]\bar{\alpha} + \mathcal{O}\left(\bar{\alpha}^2\right). \end{aligned} \tag{3.40}$$

The crossover point should occur when the leading order α contribution vanishes and the equation reduces to its GR equivalent. This is done by first fixing the mass in terms of the GR ISCO radius (since, at the crossover point, $\bar{r}^{(0)}_{ISCO} = \bar{r}^{(0)GR}_{ISCO}$). This relation can be found by solving the 0th order coefficient of equation 3.40:

$$\bar{M} = \frac{1}{12}\left(\bar{r}^{(0)GR}_{ISCO} - 15(\bar{r}^{(0)GR}_{ISCO})^3 + \sqrt{(\bar{r}^{(0)GR}_{ISCO})^2 + 66(\bar{r}^{(0)GR}_{ISCO})^4 + 225(\bar{r}^{(0)GR}_{ISCO})^6}\right). \tag{3.41}$$

This fixed mass is then substituted into the leading order term in equation (3.40). Setting this equal to 0 and solving, we find the crossover occurs at $\bar{r}^{(0)GR}_{ISCO} = 0.965679$ which corresponds to a crossover mass of

$$\bar{M}_{\text{x}}^{\bar{r}^{(0)}_{ISCO}} = 0.247935. \tag{3.42}$$

For $\bar{j}^{(0)}_{ISCO}$ we have an analytic expression which is not too complicated, and can be directly expanded in a small α power series as follows:

$$\begin{aligned}\bar{j}^{(0)}_{ISCO} = {} & \frac{\sqrt{-(\bar{r}^{(0)GR}_{ISCO})^2\left(\bar{M}+(\bar{r}^{(0)GR}_{ISCO})^3\right)}}{\sqrt{3\bar{M}-\bar{r}^{(0)GR}_{ISCO}}} - \frac{\left(2\bar{M}-(\bar{r}^{(0)GR}_{ISCO})^3\right)\sqrt{-(\bar{r}^{(0)GR}_{ISCO})^2\left(\bar{M}+(\bar{r}^{(0)GR}_{ISCO})^3\right)}}{2\left((\bar{r}^{(0)GR}_{ISCO})^3(3\bar{M}-\bar{r}^{(0)GR}_{ISCO})^{3/2}\left(\bar{M}+(\bar{r}^{(0)GR}_{ISCO})^3\right)\right)} \\ & \times\left(6\bar{M}^2-3\bar{M}(\bar{r}^{(0)GR}_{ISCO})^3-4\bar{M}\bar{r}^{(0)GR}_{ISCO}-(\bar{r}^{(0)GR}_{ISCO})^4\right)\bar{\alpha}+\mathcal{O}\left(\bar{\alpha}^2\right)\end{aligned} \tag{3.43}$$

suggesting that the results will cross over when $\left(2\bar{M}-(\bar{r}^{(0)GR}_{ISCO})^3\right)=0$. We can solve this by replacing $\bar{M}$ with equation (3.41) yielding a crossover point of $\bar{r}^{(0)GR}_{ISCO}=\frac{1}{\sqrt{2}}$, or equivalently

$$\bar{M}_{\mathrm{x}}^{\bar{j}^{(0)}_{ISCO}}=\frac{1}{4\sqrt{2}}\approx 0.1768. \tag{3.44}$$

For $\bar{E}^{(0)}_{ISCO}$, the crossover condition is identical to that for $\bar{j}^{(0)}_{ISCO}$: $\left(2\bar{M}-(\bar{r}^{(0)GR}_{ISCO})^3\right)=0$. Because of this is is clear that

$$\bar{M}_{\mathrm{x}}^{\bar{E}^{(0)}_{ISCO}}=\bar{M}_{\mathrm{x}}^{\bar{j}^{(0)}_{ISCO}}=\frac{1}{4\sqrt{2}}\approx 0.1768. \tag{3.45}$$

The above values for $\bar{M}_{\mathrm{x}}$ all agree with the expected values from a visual inspection of figure 3.5. It is also interesting to note the turnaround behaviour of $E^{(1)}_{ISCO}$ in this region of parameter space as α increases.

As α approaches criticality (figure 3.6), we see an extreme departure from the GR results for almost all of the AdS ISCO solutions. No crossover behaviour is observed, and the equations become very sensitive to changes in α in this region of parameter space (however, the value of $\bar{M}_{min}$ is nearly constant). When $\alpha/\alpha_C\sim 0.90$ we start to see this extreme sensitivity, with $\bar{M}_{min}=0.544$ when $\bar{\alpha}=\bar{\alpha}_c$.

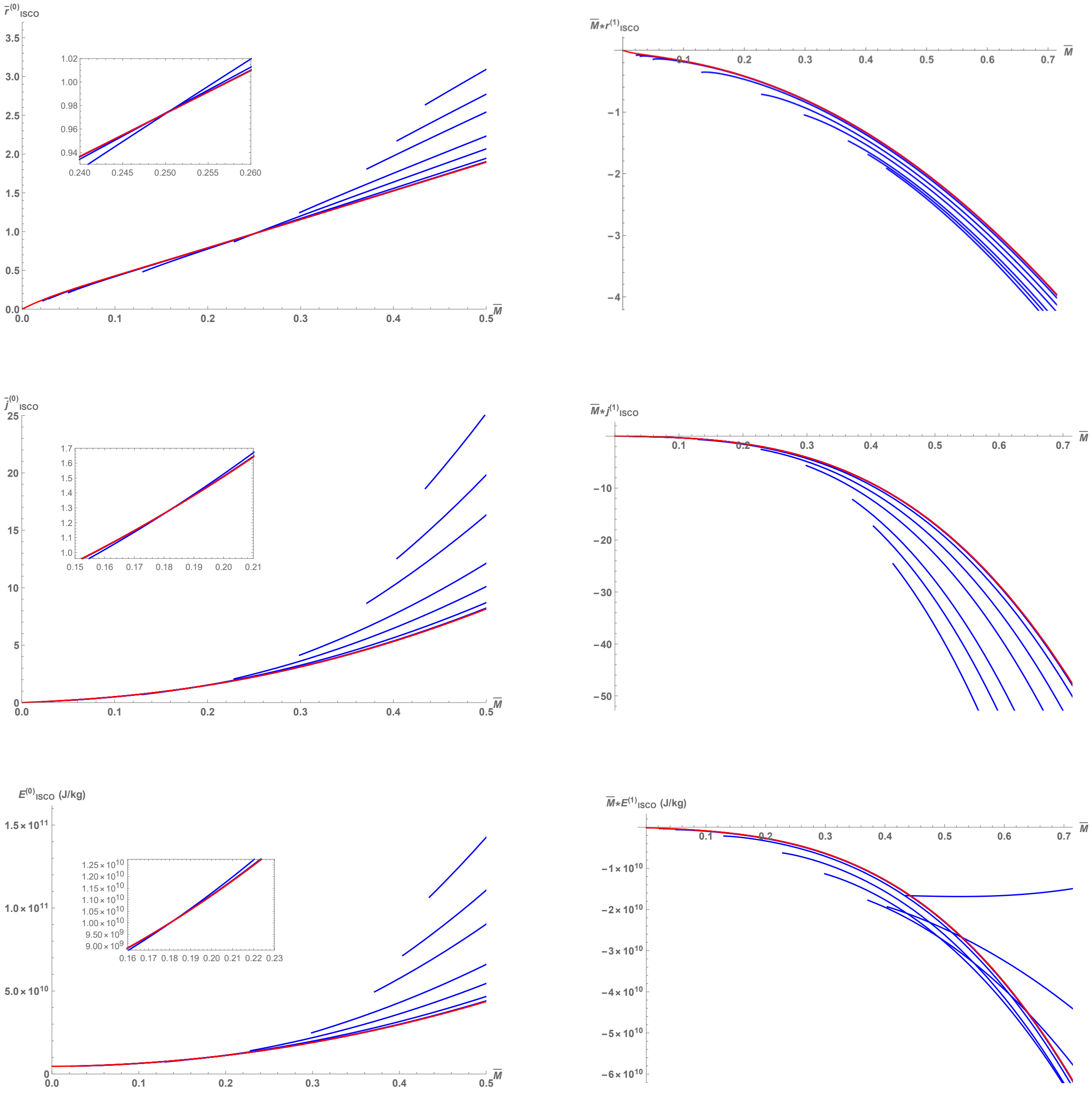

Figure 3.5: In the regime $\alpha \sim \frac{\alpha_C}{100}$ we see the 4DGB solution cross over the GR solution (in red) as mass increases for the 0th order ISCO parameters, shown in the left column. In the above plots we plot this behaviour in an asymptotically anti-de Sitter spacetime whith $\frac{\alpha}{\alpha_C} = 0.002, 0.0033, 0.01, 0.066, 0.2, 0.33, 0.5, 0.5833, 0.66$ from left to right (in blue).

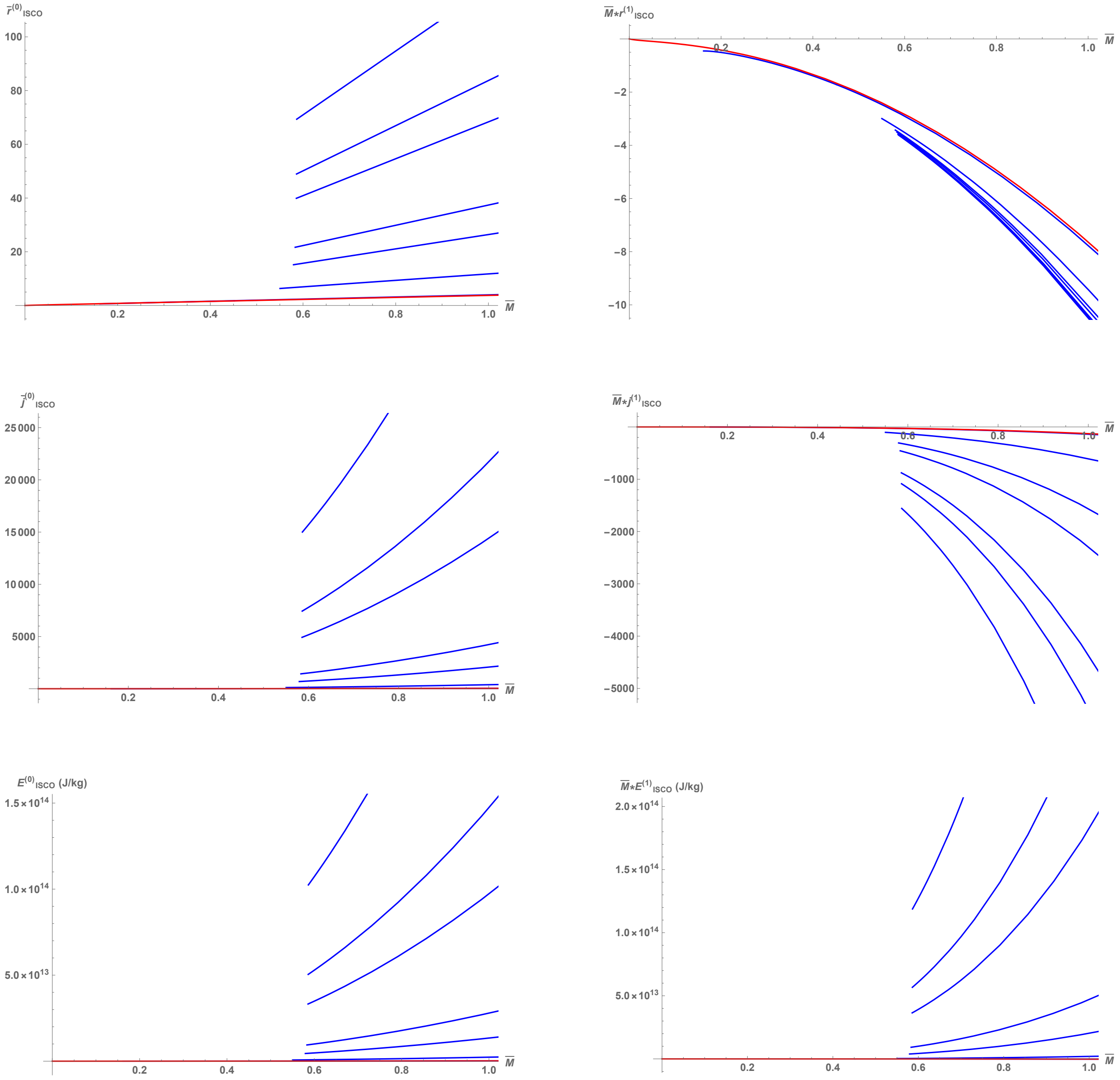

Figure 3.6: Plots of the ISCO parameters in an asymptotically andi-de Sitter spacetime. The leftmost column contains the 0th order (static) terms, whereas the rightmost column contains the leading order corrections due to rotational effects. In all cases the red line represents the solution from GR (ie. when $\alpha = 0$), and the blue lines represent the 4DGB solutions for $\frac{\alpha}{\alpha_C} = 0.1, 0.9, 0.98, 0.99, 0.997, 0.998, 0.999$ from left to right.

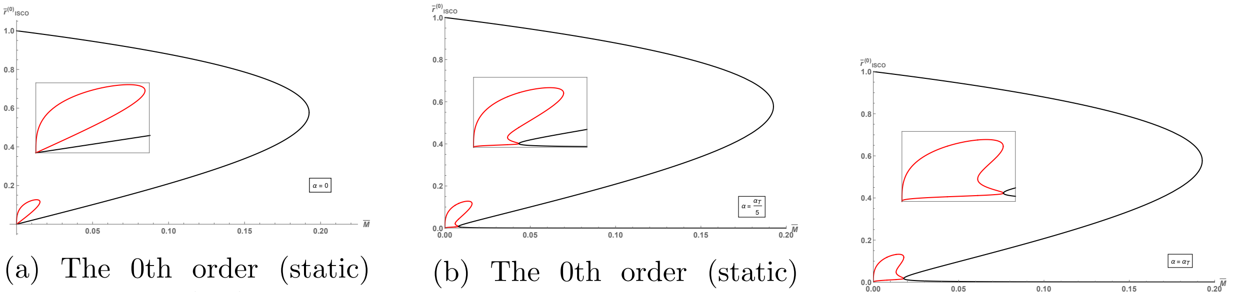

(a) The 0th order (static) ISCO radius (red) and the black hole horizons (black) for GR ($\alpha = 0$) plotted as a function of mass in an asymptotically de Sitter spacetime. A non-zero, positive Λ forces the ISCO solution to curl back into a loop which has two stable radii for each fixed mass (and also has a maximum mass for which an ISCO is defined).

(b) The 0th order (static) ISCO radius (red) and the black hole horizons (black) for $\alpha = \frac{\alpha_T}{5}$) plotted as a function of mass when in an asymptotically de Sitter spacetime. The introduction of a non-zero Gauss-Bonnet coupling constant introduces an inner black hole horizon, enforcing a minimum mass as well as the maximum mass from the de Sitter GR case.

(c) The 0th order (static) ISCO radius (red) and the black hole horizons (black) for $\alpha = \alpha_T$) plotted as a function of mass in an asymptotically de Sitter spacetime. By this point the entire ISCO solution set lies in the region of parameter space which describes a naked singularity.

Figure 3.7: Depiction of the 0th order ISCO radius for $\alpha = 0$ (left), $\alpha = \frac{\alpha_T}{5}$ (middle), and $\alpha = \alpha_T$ (right).

dS ($\Lambda > 0$)

The ISCO solutions in de Sitter space are particularly nuanced. We begin with a thorough investigation of the non-rotating ISCO solutions in GR ($\alpha = 0$) before moving forward with the 4DGB solutions.

The Einstein de Sitter ISCO solutions are plotted in figure 3.7a alongside the corresponding black hole horizons for a positive cosmological constant. We immediately observe that for non-zero positive Λ, a turning point appears for $M = \frac{2}{75\sqrt{\Lambda}}$. There are two possible ISCOs at any given mass less than this value, and no ISCOs for $\frac{2}{75\sqrt{\Lambda}} < M < \frac{1}{3\sqrt{\Lambda}}$, the latter value being the Nariai upper mass limit $\frac{1}{3\sqrt{\Lambda}}$, obtained by setting $\alpha = 0$ in (3.31). In other words, this turning point always occurs at $M < M_{max}$ and thus the ISCO solutions within the allowed mass range are physical.

When a non-zero Gauss-Bonnet coupling constant is introduced, many ISCO solutions are no longer physical due to the presence of a minimum mass. This is clear from the middle diagram in figure 3.7, which plots $r^{(0)}_{\text{ISCO}}$ (red curve) as a function of M for different values of α. We see for $\alpha = 0$ that all points on the double-valued ISCO curve are physically allowed, whereas for $\alpha > 0$, all points to the left of $M = M_{min}$ are unphysical. This is because the $M < M_{min}$ region of parameter space represents a naked singularity due to a change in horizon structure (see figures 3.3a and 3.7b). As α continues to get larger, the physically allowed ISCO region gets smaller.

Finally, at some transitory value ($\alpha = \alpha_T$), the turning point of the ISCO (which is also its maximum mass point) equals the minimum mass value, shown in the rightmost diagram 3.7c in figure 3.7. We find that $\alpha_T = \frac{\alpha_C}{260} = \frac{1}{1040\Lambda}$. For $\alpha > \alpha_T$ no physical ISCOs exist; all ISCO solutions correspond to spacetimes with naked singularities surrounded by a cosmological horizon. When $\alpha = \alpha_T$, there is a single ISCO, which occurs at the critical mass point

$$M_{crit}|_{\alpha=\alpha_T} = \frac{\sqrt{263 - 259\sqrt{\frac{259}{260}}}}{3\sqrt{520\Lambda}} \approx \frac{1}{\sqrt{1000\Lambda}} \tag{3.46}$$

from (3.31).

Armed with this knowledge, we solve numerically the ISCO equations once again for a positive cosmological constant with α varying from 0 to α_T. These results are shown in figure 3.8. The main feature of interest in asymptotically de Sitter space is the existence of two discrete stable orbits for a fixed black hole mass. All 0th order ISCO parameters are double-valued, with the 4DGB case having a cutoff at M_{min} as noted above, and turning around at M_{crit}. The 1st order ISCO parameters are also confined between M_{min} and M_{crit}, with the actual values depending on α. The smallest and largest allowed 0th order ISCO radii at any given mass in the 4DGB theory are respectively smaller and larger than their GR counterparts. As $\alpha \to \alpha_T$, the 4DGB ISCO parameters occur at values of the mass larger than the GR upper limit $M = \frac{2}{75\sqrt{\Lambda}}$, hence having no overlap in allowed mass with GR.

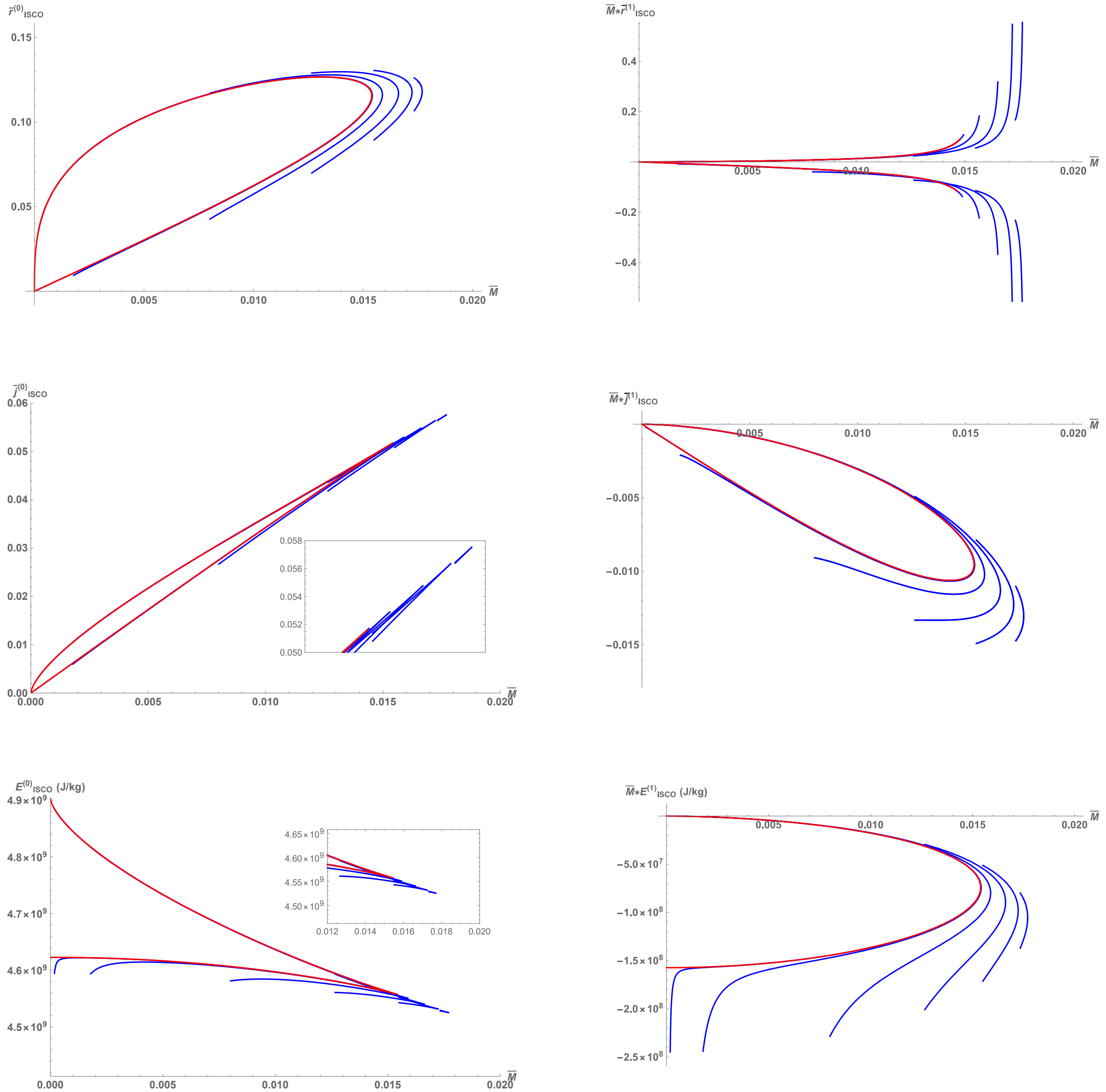

Figure 3.8: Plots of the ISCO parameters in an asymptotically de Sitter spacetime. The leftmost column contains the 0th order (static) terms, whereas the rightmost column contains the leading order corrections due to rotational effects. In all cases the red line represents the solution from GR (ie. when $\alpha = 0$), and the blue lines represent the 4DGB solutions for $\frac{\alpha}{\alpha_T} = 0.0001, 0.01, 0.2, 0.5, 0.75, 0.9375$ from left to right.

3.2.4 Null Geodesics: Photon Rings

Now we turn our attention to how slow rotation in the 4DGB theory deforms the photon rings of black holes. The photon ring is defined by null geoedsic orbits ($\xi = 0$) of constant r, which we take to lie in the equatorial plane (ie. $x = 0$) without loss of generality. Rather than work with conserved quantities E and j as in the previous section, we instead follow [68] and consider the problem in terms of angular velocity ($\omega = d\phi/dt$) which is conserved along the null trajectory. From equation 3.37 we know that a photon outside of our black hole will be subject to an effective potential

$$V_{\text{ph}} = \frac{f(r)\ell_z^2 - r^2E^2}{2r^2} - a\frac{P(r)\ell_z E}{r^2}. \tag{3.47}$$

For circular orbits (ie. $\dot{r} = 0$), the location of the photon ring is determined by

$$V_{\text{ph}}(r) = 0 \qquad V'_{\text{ph}}(r) = 0 \tag{3.48}$$

where $\omega = \frac{d\phi}{dt} = \frac{\dot{\phi}}{\dot{t}}$ is conserved along the photon trajectory, and we have let $E = 1$ without loss of generality by rescaling the affine parameter. These end up being equivalent to the following two conditions:

$$f(r_{pr}) - r_{pr}^2\omega^2 - 4aP(r_{pr})\omega = 0 \tag{3.49}$$

$$f'(r_{pr}) - 2r_{pr}\omega^2 - 4aP'(r_{pr})\omega = 0 \tag{3.50}$$

which can be solved analytically to leading order in a by writing

$$r_{pr} = r_{pr}^{(0)} + ar_{pr}^{(1)} \qquad \omega_{pr} = \omega_{pr}^{(0)} + a\omega_{pr}^{(1)}. \tag{3.51}$$

With this, we find that

$$f'(r_{pr}^{(0)}) = 2\frac{f(r_{pr}^{(0)})}{r_{pr}^{(0)}}, \quad \omega_{pr}^{(0)} = \pm\frac{\sqrt{f(r_{pr}^{(0)})}}{r_{pr}^{(0)}} \tag{3.52}$$

and

$$r_{pr}^{(1)} = \pm\frac{2r_{pr}^{(0)3}\sqrt{f(r_{pr}^{(0)})}p'(r_{pr}^{(0)})}{r_{pr}^{(0)2}f''(r_{pr}^{(0)}) - 2f(r_{pr}^{(0)})}, \quad \omega_{pr}^{(1)} = -p(r_{pr}^{(0)}). \tag{3.53}$$

where the plus/minus signs correspond to prograde/retrograde motion. The above expressions can easily be solved numerically for $r_{pr}^{(0)}$, $r_{pr}^{(1)}$, $\omega_{pr}^{(0)}$, and $\omega_{pr}^{(1)}$, which is done in the following subsections for $\Lambda = 0$ as well as dS/AdS space.

One interesting combination of quantities to consider is $\frac{\omega_+}{|\omega_-|}$. In GR it is known that this ratio is controlled by the black hole spin parameter alone [68, 130] in asymptotically flat space (or the spin parameter and black hole mass in asymptotically dS/AdS space), whereas in the 4DGB theory we also have dependence on the higher order coupling. In principle this feature could be useful in constraining the 4DGB coupling constant via an independent black hole spin/mass measurement.

We conclude this section by investigating the stability of the photon ring orbits. Of course they are unstable, although we can better understand this instability by calculating the associated Lyapunov exponent [68, 131], which provides a measure of the growth of the photon orbit instability as a function of time. More precisely, under the Eikonal approximation the Lyapunov exponent comes from the imaginary part of the quasi-normal mode frequencies of the photon orbit [131] (while the real part is related to the angular velocity off the unstable null orbits). It can be proven [132] that for any static, spherically symmetric spacetime

$$\omega_{QNM} = \omega_{pr}^{(0)}\ell - i(n + \frac{1}{2})|\lambda| \tag{3.54}$$

where ω_{QNM} is a quasi-normal mode frequency, and λ is the Lyapunov exponent associated with the orbit. We can extract its value by again following the work of [68, 131]. We begin with differentiating the geodesic equation (3.36) with respect to the affine parameter

$$\frac{d}{ds}\left(\frac{1}{2}\dot{r}^2 + V_{\mathrm{ph}}(r) = 0\right) \Rightarrow \frac{d^2 r}{ds^2} + \frac{dV_{\mathrm{ph}}(r)}{dr} = 0 \tag{3.55}$$

and then perturb (3.55) according to

$$r(t) = r_{pr}^{(0)}\left(1 + \epsilon F(t)\right),\ s(t) = \frac{t}{\beta} + \epsilon G(t),\ \phi(t) = |\omega_\pm|(1 + \epsilon H(t)) \tag{3.56}$$

where ϵ is a small parameter controlling the perturbation strength and $\beta = \frac{dt}{ds}|_{r\to r_{pr}}$ is a parameter relating coordinate time to s in the absence of a perturbation. We require the system to have vanishing perturbation at $t = 0$. Expanding (3.55) to first order in ϵ yields

$$\beta^2 F''(t) + F(t)V''_{\mathrm{ph}}(r_{pr}^{(0)}) = 0 \tag{3.57}$$

which has the solution

$$F(t) \propto \sinh\left(t\lambda\right) \tag{3.58}$$

where

$$\lambda^2 = -\frac{V''(r_{ps}^{(0)})}{\beta^2} := U \; .$$

As with everything else up to this point, we write the solution as a zeroth-order term plus a linear rotational correction:

$$\lambda = \lambda^{(0)} + a\lambda^{(1)}. \tag{3.59}$$

Since the perturbative and non-perturbative parts should hold true independently (and since $V''(r_{ps}^{(0)}) = V_0'' + aV_1''$), we can break the relation between λ and $V''(r_{ps}^{(0)})$ into two equations, namely:

$$\lambda_0 = \sqrt{U_0} \tag{3.60}$$

$$\lambda_1 = \frac{U_1}{2\lambda_0} \tag{3.61}$$

where U_0 and U_1 are the 0th and 1st order terms of a power series representation of U in the rotation parameter a.

$\mathbf{\Lambda = 0}$

In this section we solve for the photon ring in asymptotically flat space. The solutions to equation (3.51) are plotted in figure 3.9 alongside the results for GR. As the mass for a given 4DGB solution approaches its minimum allowed mass the results increasingly depart from those in GR, whereas they become virtually indistinguishable for larger masses. All curves are similar in form to the GR results, apart from this low mass behaviour. It is worth noting that the reason for the large values on the y-axes of figures 3.11a and 3.11b are due to the unit conversion from inverse solar masses to inverse seconds. If instead the quantity λ/Ω (see [132, 133]), results on the order of unity are observed.

In asymptotically flat spacetimes, the ratio $\Omega := \frac{\omega_+}{|\omega_-|}$ ends up being a function of $\bar{M}$, $\bar{\alpha}$, and χ. The numerical solutions of this ratio for $\Lambda = 0$ are plotted in figure 3.10 alongside the corresponding quantity from GR. We see that the GR results are constant with respect to mass, whereas the 4DGB results change rapidly as mass gets small. Note that the greatest departure from the GR results occurs again in the low mass region near the minimum, and convergence with the GR solution is observed as mass gets large.

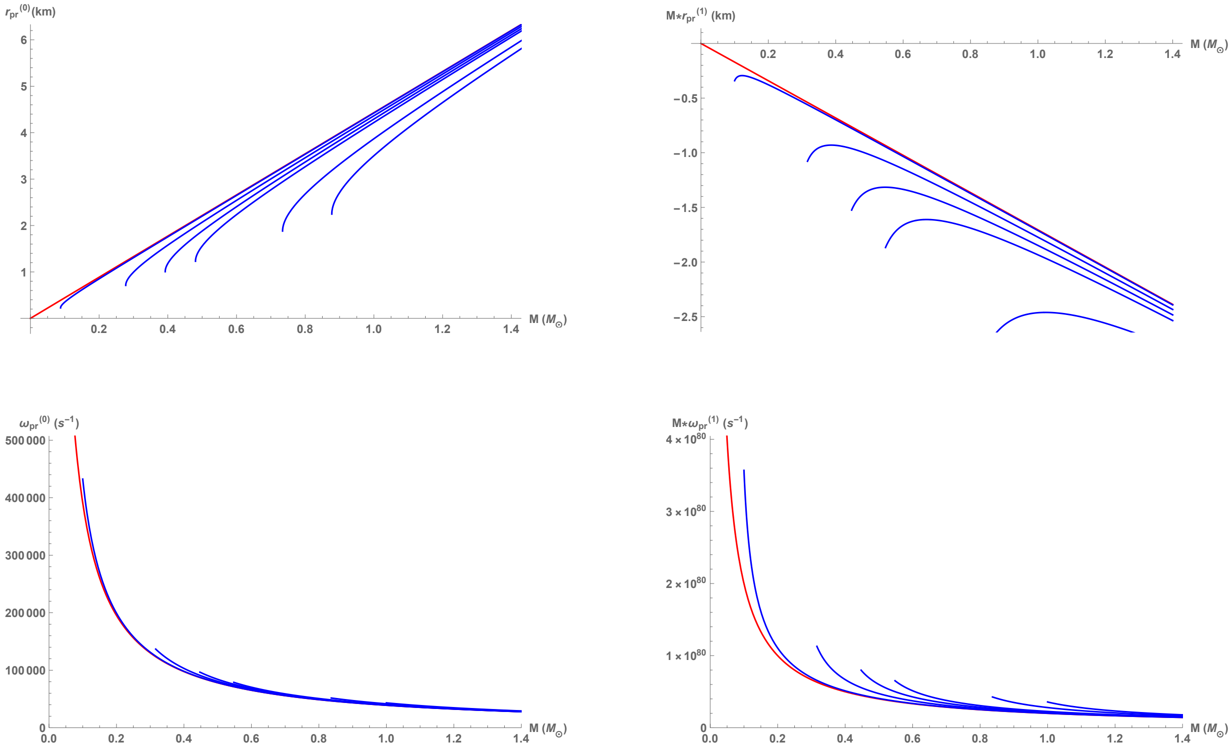

Figure 3.9: Photon ring solutions when $\Lambda = 0$. In all cases the red line represents the GR solution ($\alpha = 0$), and the blue lines represent the 4DGB solutions for $\frac{\alpha}{M_\odot^2} = 0.01, 0.1, 0.2, 0.3, 0.7, 1$ (from left to right).

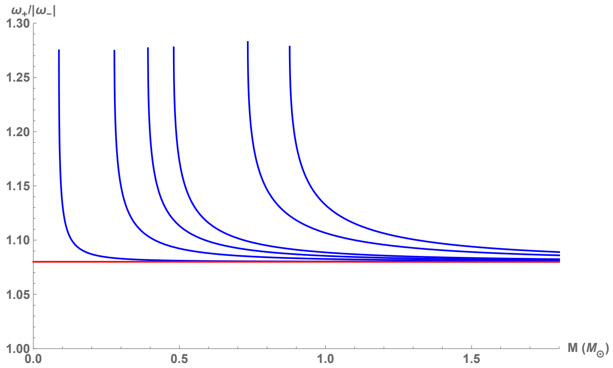

Figure 3.10: Ratio of $\frac{\omega_+}{|\omega_-|}$ in GR (red) plotted against the same ratio in the 4DGB theory (blue) when $\Lambda = 0$ for $\frac{\alpha}{M_\odot^2} = 0.01, 0.1, 0.2, 0.3, 0.7, 1$ (from left to right). In this figure we have fixed $\chi = 0.1$.

Similarly, in figures 3.11a and 3.11b, we find that the stability of the photon ring in the 4DGB theory is very similar to GR unless the mass in near its minimum value, in which case the value of λ drops considerably. While the leading order corrections to the Lyapunov exponent vanish in Einstein's theory, we find a nonzero negative value which converges with GR in the large mass limit. Since both the 0th and leading order contributions to λ in the 4DGB theory are large and negative near M_{min}, near-minimal mass objects should have significantly less unstable photon rings than the values predicted by GR.

AdS ($\Lambda < 0$)

Here we solve for the photon ring parameters again, this time in asymptotically AdS space. The relevant solutions to (3.51) are plotted in figures 3.12 and 3.13 alongside the analogous results from GR. In the small alpha regime one again notices a "crossover" behaviour at some critical mass for three of the four photon ring parameters. The location of the photon sphere is uniquely determined by the equation

$$f'(\bar{r}^{(0)}_{ISCO}) - 2\frac{f(\bar{r}^{(0)GR}_{ISCO})}{\bar{r}^{(0)GR}_{ISCO}} = 0. \tag{3.62}$$

As in the previous sections we expand this equation to leading order in α:

$$\left(\frac{3M}{\bar{r}^{(0)GR}_{ISCO}} - 1\right) - \frac{6M\left(2M - (\bar{r}^{(0)GR}_{ISCO})^3\right)}{(\bar{r}^{(0)GR}_{ISCO})^4}\bar{\alpha} + \mathcal{O}\left(\bar{\alpha}^2\right) = 0 \tag{3.63}$$

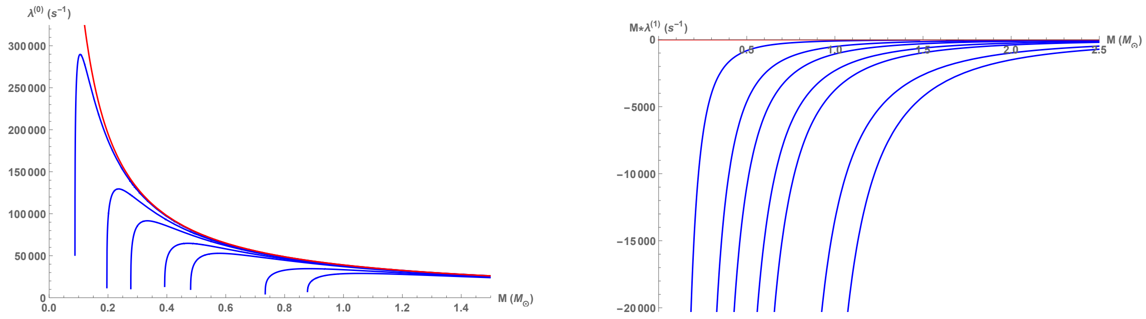

(a) 0th order Lyapunov exponent correction for the photon ring when $\Lambda = 0$. The red curve shows the GR ($\alpha = 0$) result, whereas the blue curves represent the 4DGB results for $\frac{\alpha}{M_\odot^2} = 0.01,\ 0.05,\ 0.1,\ 0.2,\ 0.3,\ 0.7,\ 1$.

(b) Leading order Lyapunov exponent correction for the photon ring when $\Lambda = 0$. The red curve shows the GR ($\alpha = 0$) result, whereas the blue curves represent the 4DGB results for $\frac{\alpha}{M_\odot^2} = 0.01, 0.05, 0.1, 0.2, 0.3, 0.7, 1$.

Figure 3.11: Lyapunov exponents when $\Lambda = 0$.

and then fix black hole mass in terms of its GR definition (by solving the 0th order coefficient):

$$\bar{M} = \frac{1}{3}\bar{r}_{pr}^{(0)GR}. \tag{3.64}$$

We can then substitute this fixed mass into the leading order coefficient to find the point of interest, yielding a crossover at $\bar{r}_{pr}^{(0)} = \sqrt{\frac{2}{3}}$, or equivalently

$$\bar{M}_{\mathrm{x}}^{\bar{r}_{pr}^{(0)}} = \sqrt{\frac{2}{27}} \tag{3.65}$$

which matches what is expected from figure 3.12. For $\bar{\omega}_{pr}^{(0)}$, rather than a crossover we have a point at which the solution touches the GR curve before increasing again. For this point the analysis is identical, and we find

$$\bar{M}_{\mathrm{x}}^{\bar{\omega}_{pr}^{(0)}} = \bar{M}_{\mathrm{x}}^{\bar{r}_{pr}^{(0)}} = \sqrt{\frac{2}{27}}. \tag{3.66}$$

In the regime of large α (ie. $\frac{\alpha}{\alpha_C} \sim \frac{9}{10}$) the solutions become very sensitive to small changes in the 4DGB coupling, and again we see non-rotating radius results that depart dramatically from GR at all mass scales in this regime (similar to what was discussed for

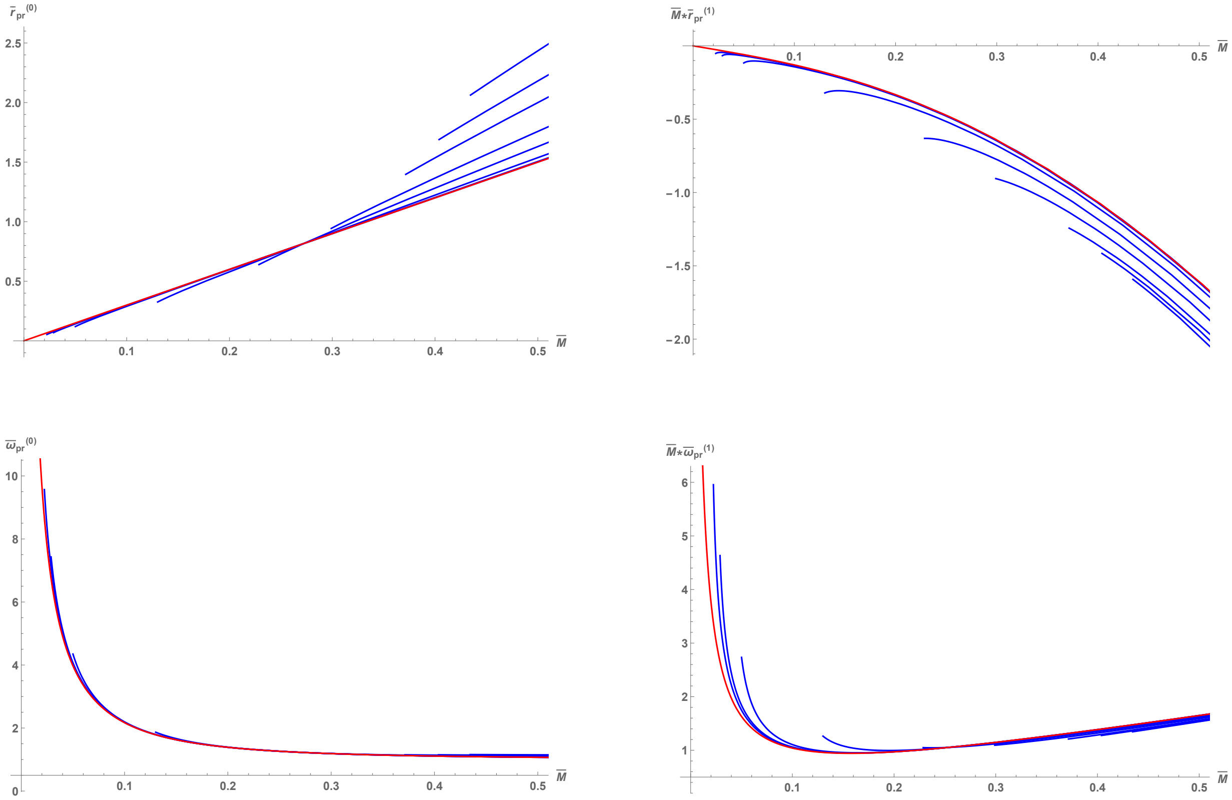

Figure 3.12: Photon ring solutions in an asymptotically anti-de Sitter spacetime for $\frac{\alpha}{\alpha_C} =$ 0.002, 0.0033, 0.01, 0.066, 0.2, 0.33, 0.5, 0.5833, 0.66 (from left to right in blue) against the GR ($\alpha = 0$) solution in red.

the AdS ISCO). The other three parameters are bounded in this large α limit, and change very little with respect to varying α.

In spacetimes with a nonzero cosmological constant, the ratio $\Omega \coloneqq \frac{\omega_+}{|\omega_-|}$ again ends up being a function of $\bar{M}$, $\bar{\alpha}$, and χ. The numerical solutions of this ratio for AdS space are plotted in Figure 3.14 where we hold $\chi = 0.01$ constant. When $\bar{M}$ is small, this ratio is larger for the 4DGB theory than it is for GR. As the fixed mass increases, the curves cross and $\Omega_{GR} > \Omega_{4DGB}$. Since the 4DGB theory has a minimum mass that depends on α, only the black holes corresponding to $\alpha/\alpha_C \lessapprox \frac{1}{5}$ will start above the GR curve, whereas

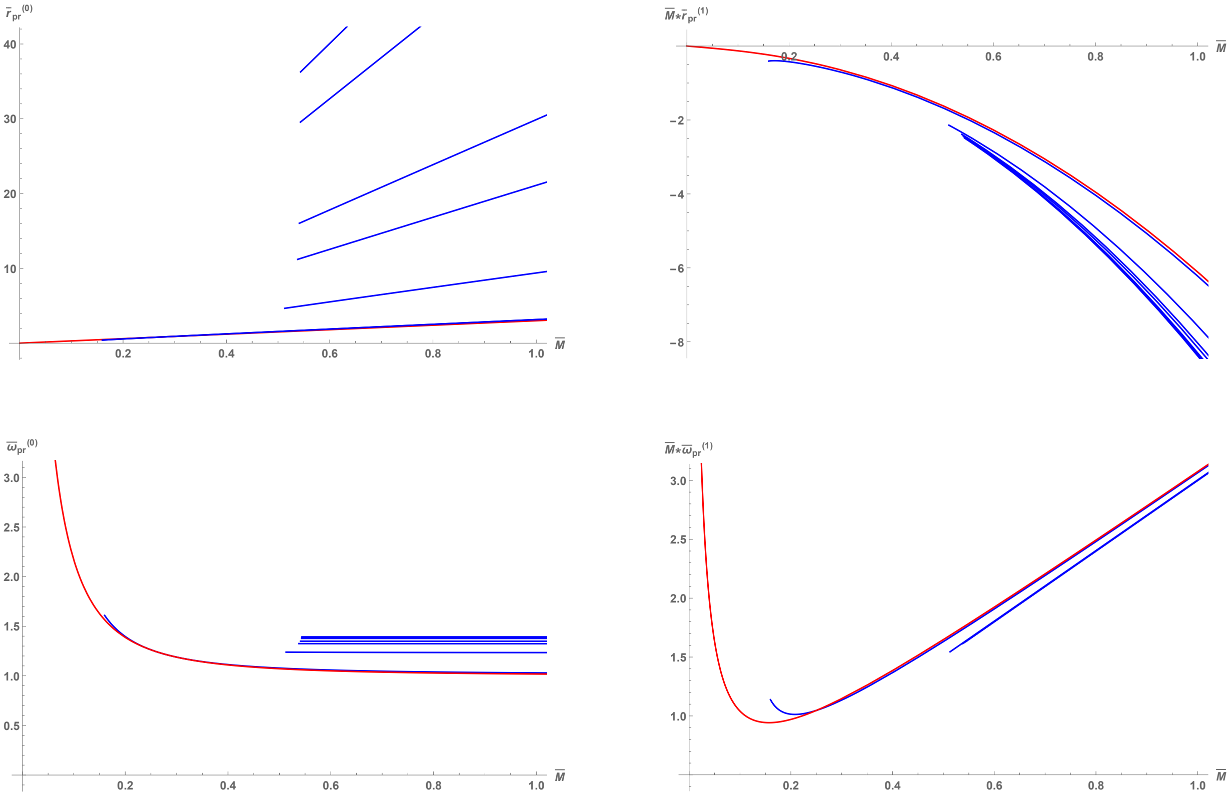

Figure 3.13: Photon ring solutions in an asymptotically anti-de Sitter when α is near its critical value (ie. $\frac{\alpha}{\alpha_C} = 0.1,\ 0.9,\ 0.98,\ 0.99,\ 0.997,\ 0.998,\ 0.999$) from left to right in blue against the GR ($\bar{\alpha} = 0$) solution in red.

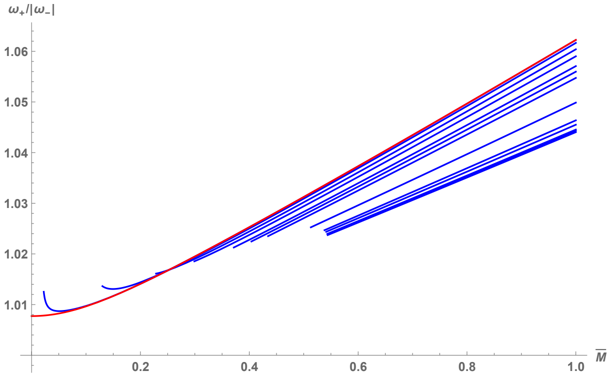

Figure 3.14: Ratio of $\frac{\omega_+}{|\omega_-|}$ in an asymptotically anti-de Sitter spactime. The GR solution (red) is plotted against the same ratio in the 4DGB theory (blue) for $\frac{\alpha}{\alpha_C} = 0.002$, 0.066, 0.2, 0.33, 0.5, 0.5833, 0.66, 0.9, 0.98, 0.99, 0.997, 0.998, 0.999. In this figure we have fixed $\chi = 0.01$.

solutions with a larger coupling constant are not defined in the small mass regime. In order to find which combinations of $\bar{M}$ and χ in the 4DGB theory will give a ratio that agrees with GR (ie. the crossing point), we expand the numerator of Ω_{4DGB} to 1st order in α:

$$\Omega_{4DGB}^{num} = \Omega_{GR}^{num} + \frac{\left(32\left(5 - 81\bar{M}^2\right)\chi + \frac{12\sqrt{3}\left(2-27\bar{M}^2\right)^2}{\sqrt{27\bar{M}^2+1}}\right)}{5832\bar{M}^3}\bar{\alpha} + \mathcal{O}(\bar{\alpha}^2). \tag{3.67}$$

and similarly with the denominator:

$$\Omega_{4DGB}^{denom} = \Omega_{GR}^{denom} + \frac{\left(32\left(5 - 81\bar{M}^2\right)\chi - \frac{12\sqrt{3}\left(2-27\bar{M}^2\right)^2}{\sqrt{27\bar{M}^2+1}}\right)}{5832\bar{M}^3}\bar{\alpha} + \mathcal{O}(\bar{\alpha}^2). \tag{3.68}$$

By setting the α^2 terms equal to 0 in both cases we find two equations in $\bar{M}$ and χ, namely:

$$\chi = \frac{-\frac{2187\sqrt{3}\bar{M}}{\sqrt{27\bar{M}^2+1}} + \frac{324\sqrt{3}}{\bar{M}\sqrt{27\bar{M}^2+1}} - \frac{12\sqrt{3}}{\bar{M}^3\sqrt{27\bar{M}^2+1}}}{\frac{40}{\bar{M}^3} - \frac{648}{\bar{M}}} \tag{3.69}$$

$$\chi = \frac{\frac{2187\sqrt{3}\bar{M}}{\sqrt{27\bar{M}^2+1}} - \frac{324\sqrt{3}}{\bar{M}\sqrt{27\bar{M}^2+1}} + \frac{12\sqrt{3}}{\bar{M}^3\sqrt{27\bar{M}^2+1}}}{\frac{40}{\bar{M}^3} - \frac{648}{\bar{M}}} \tag{3.70}$$

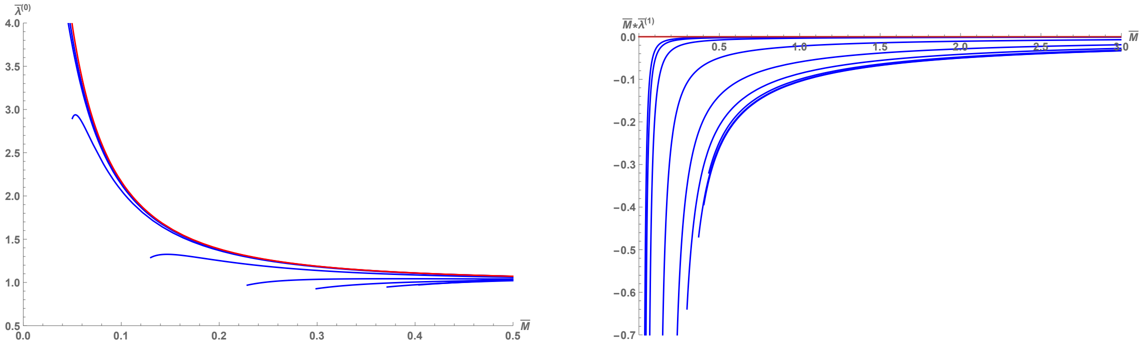

(a) 0th order Lyapunov exponent correction for the photon ring in an asymptotically anti-de Sitter spacetime when α is small. The red curve shows the GR ($\alpha = 0$) result, whereas the blue curves represent the 4DGB results for $\frac{\alpha}{\alpha_C} = 0.002$, 0.0033, 0.01, 0.066, 0.2, 0.33, 0.5, 0.5833, 0.66.

(b) Leading order Lyapunov exponent correction for the photon ring when α is small and $\Lambda < 0$. The red curve shows the GR ($\alpha = 0$) result, whereas the blue curves represent the 4DGB results for $\frac{\alpha}{\alpha_C} = 0.002$, 0.0033, 0.01, 0.066, 0.2, 0.33, 0.5, 0.5833, 0.66.

Figure 3.15: Lyapunov exponents when $\Lambda < 0$ and α is small.

The above expressions both hold only at the divergence point $\bar{M} = \frac{1}{3}\sqrt{\frac{2}{3}}$, and thus at this mass the crossover point is defined (ie. $\Omega_{4DGB} \approx \Omega_{GR}$ for all χ) when $\bar{\alpha}$ is small.

When α is small we again see values for the Lyapunov exponent which are similar in form to GR until minimum mass is approached (see figures 3.15a and 3.15b). One notices that the departure in this regime is less dramatic than what was seen in the asymptotically flat case. However, as α approaches criticality (figures 3.16a and 3.16b), we notice a change in direction in these results with respect to increasing α. The 0th order contribution for large enough α will either cross over or start above the GR results (ie. more unstable), and the leading order corrections end up converging back to GR near α_C, with even the point at $M_{\min}$ not diverging too far from the red curve.

dS ($\boldsymbol{\Lambda > 0}$)

Finally, we solve for the photon ring parameters one last time in asymptotically de Sitter space. The relevant solutions to (3.51) are plotted in figure 3.17. Again we see the largest departure from the GR case for small masses, and convergence as mass becomes large. The

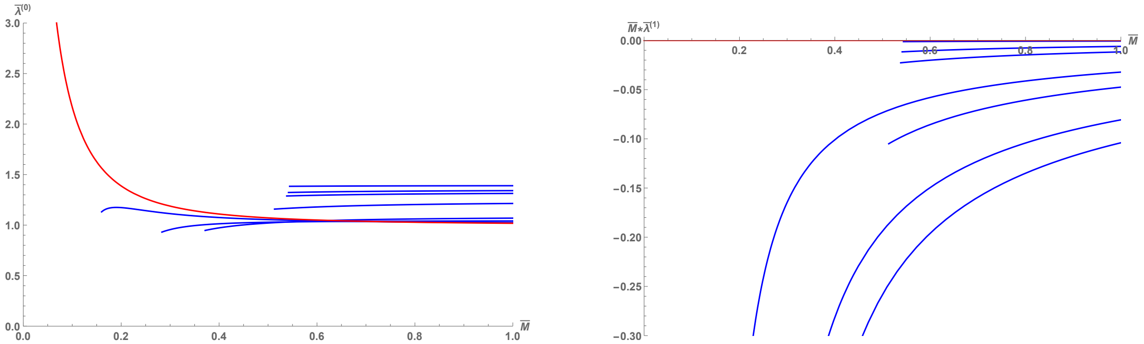

(a) 0th order Lyapunov exponent for the photon ring in an asymptotically anti-de Sitter spacetime as α approaches criticality. The red curve shows the GR ($\alpha = 0$) result, whereas the blue curves represent the 4DGB results for $\frac{\alpha}{\alpha_C} = 0.1,\ 0.3,\ 0.5,\ 0.9,\ 0.98,\ 0.99,\ 0.999$.

(b) Leading order Lyapunov exponent correction for the photon ring in an asymptotically anti-de Sitter spacetime as α approaches criticality. The red curve shows the GR ($\alpha = 0$) result, whereas the blue curves represent the 4DGB results for $\frac{\alpha}{\alpha_C} = 0.1,\ 0.3,\ 0.5,\ 0.9,\ 0.98,\ 0.99,\ 0.999$.

Figure 3.16: Lyapunov exponents when $\Lambda < 0$ and α is near criticality.

general forms of these curves are all reminiscent of the Einstein result when sufficiently far from the minimum mass.

The ratio $\Omega := \frac{\omega_+}{|\omega_-|}$ is a function of $\bar{M}$, $\bar{\alpha}$, and χ in the 4DGB theory whereas the GR solution of course has no α dependence. The numerical solution for this ratio in asymptotically dS space is plotted in figure 3.17. When $\bar{\alpha}$ is small we find that the 4DGB solution diverges most from GR in the small mass regime, whereas in the large mass regime the result converges exactly with that from GR. For larger $\bar{\alpha}$ the allowed mass region shrinks and shifts to the right until eventually there is no overlap between the allowed masses of the 4DGB theory with GR.

In order to better understand the small $\bar{\alpha}$ behaviour, we expand the numerator and denominator of this ratio to first order in $\bar{\alpha}$:

$$\Omega^{num}_{4DGB} = \Omega^{num}_{GR} - \frac{\left(-\frac{9\left(27\bar{M}^2+2\right)^2}{\sqrt{3-81\bar{M}^2}} - 8\left(81\bar{M}^2+5\right)\chi\right)}{1458\bar{M}^3}\bar{\alpha} + \mathcal{O}(\bar{\alpha}^2), \tag{3.71}$$

and similarly with the denominator:

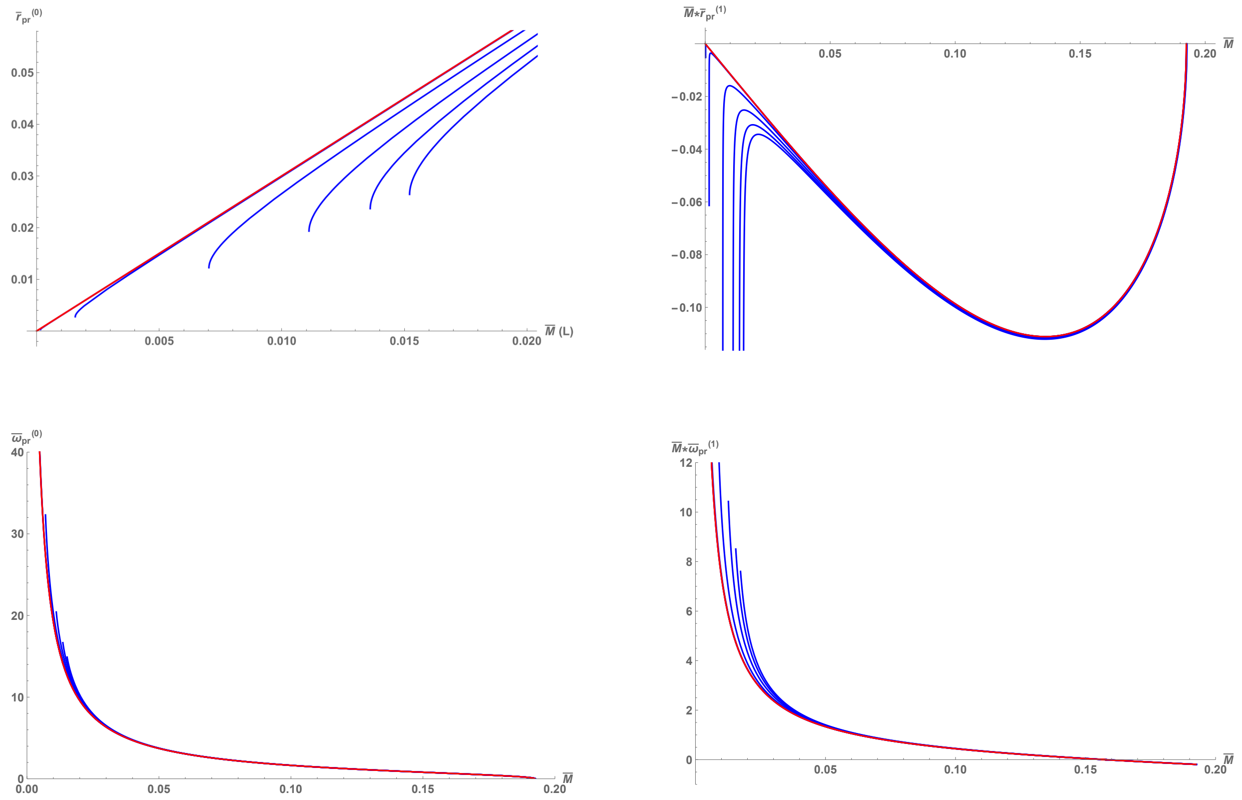

Figure 3.17: Photon ring solutions in an asymptotically de Sitter spacetime for $\frac{\alpha}{\alpha_T} = 0.0001,\ 0.01,\ 0.2,\ 0.5,\ 0.75,\ 0.9375$ (from left to right in blue) against the GR ($\alpha = 0$) solution in red.

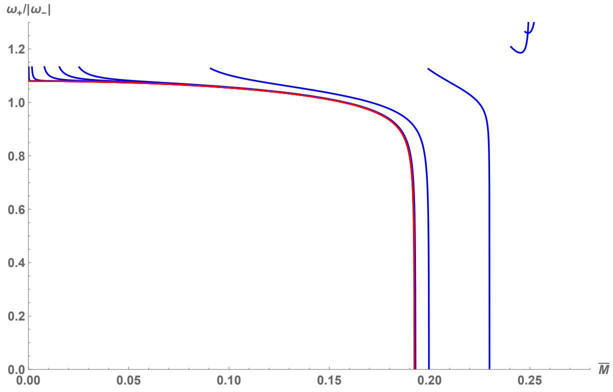

Figure 3.18: Ratio of $\frac{\omega_+}{|\omega_-|}$ in GR (red) plotted against the same ratio in the 4DGB theory (blue) for $\alpha = 0.0001\alpha_T$, $0.01\alpha_T$, $0.2\alpha_T$, $0.75\alpha_T$, $2\alpha_T$, $0.1\alpha_C$, $0.5\alpha_C$, $0.75\alpha_C$, $0.8\alpha_C$ in an asymptotically de Sitter spacetime. In this figure we have fixed $\chi = 0.1$.

$$\Omega^{denom}_{4DGB} = \Omega^{denom}_{GR} - \frac{\left(\frac{9\left(27\bar{M}^2+2\right)^2}{\sqrt{3-81\bar{M}^2}} - 8\left(81\bar{M}^2+5\right)\chi\right)}{1458\bar{M}^3}\bar{\alpha} + \mathcal{O}(\bar{\alpha}^2). \tag{3.72}$$

From here it is straightforward to show that $\Omega_{4DGB} \to \Omega_{GR}$ when $M = \frac{1}{3\sqrt{3}}$. More simply this implies that black holes with a small 4DGB coupling constant have effectively the same upper limit on mass as the GR solution, and Ω converges to the GR value in this regime so long as $\bar{M}$ doesn't approach its minimum. As $\bar{\alpha}$ becomes larger, $M^{4DGB}_{max} > M^{GR}_{max}$.

The Lyapunov exponents for asymptotically de Sitter space are plotted in figures 3.19a and 3.19b alongside the GR results. Again we find curves for $\lambda^{(0)}$ which are very similar to GR in form, diverging most near the minimum mass limit. $\lambda^{(1)}$ similarly diverges most from GR near $\bar{M}_{\text{min}}$, and converges for large mass. The low-mass reduction of instability in the 0th order exponent is comparable the the asymptotically flat case, though less dramatic. The leading order corrections seem to care less about α near M_{min}, as the stability increases significantly for all curves near this point.

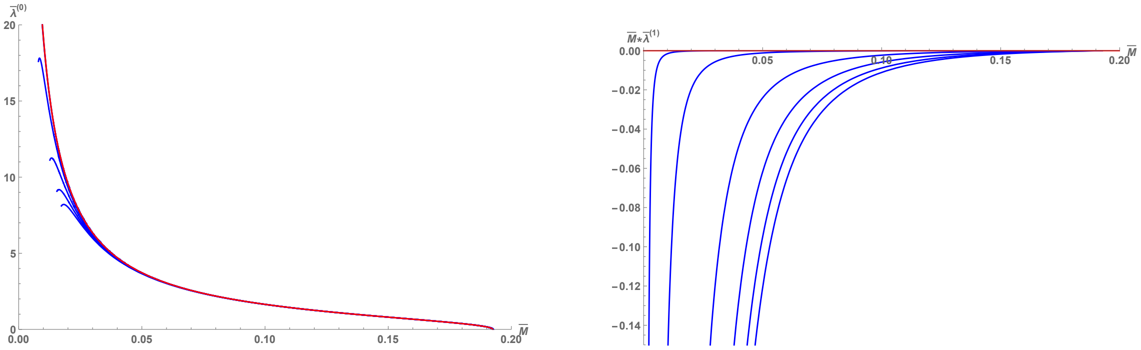

(a) 0th order Lyapunov exponent correction for the photon ring in an asymptotically de Sitter spacetime. The red curve shows the GR ($\alpha = 0$) result, whereas the blue curves represent the 4DGB results for $\frac{\alpha}{\alpha_T} = 0.0001$, 0.01, 0.2, 0.5, 0.75, 0.9375.

(b) Leading order Lyapunov exponent correction for the photon ring when in an asymptotically de Sitter spacetime. The red curve shows the GR ($\alpha = 0$) result, whereas the blue curves represent the 4DGB results for $\frac{\alpha}{\alpha_T} = 0.0001$, 0.01, 0.2, 0.5, 0.75, 0.9375.

Figure 3.19: Lyapunov exponents when $\Lambda > 0$.

3.2.5 Black Hole Shadow

A detailed, general study of non-equatorial null geodesics for a slowly rotating metric ansatz was carried out in [68], from which we obtain the following relations:

$$r^2\dot{\phi} = \frac{\ell_z}{\sin^2\theta} - \frac{aP(r)E}{f(r)}, \quad r^2\dot{\theta} = \pm\sqrt{j^2 - \frac{\ell_z^2}{\sin^2\theta}} \tag{3.73}$$

$$r_{\rm ps} = r_{\rm ps}^{(0)} + ar_{\rm ps}^{(1)}, \quad j_{\rm ps}^2 = \left(j_{\rm ps}^{(0)}\right)^2 + a\left(j_{\rm ps}^{(1)}\right)^2 \tag{3.74}$$

$$r_{\rm ps} = r_{\rm ps}^{(0)} + \left.\frac{2a\ell_z f\left(rP' - 2P\right)}{r\left(r^2 f'' - 2f\right)}\right|_{r=r_{\rm ps}^{(0)}}, \tag{3.75}$$

$$j_{\rm ps}^2 = \frac{\left(r_{\rm ps}^{(0)}\right)^2}{f\left(r_{\rm ps}^{(0)}\right)} + \frac{2a\ell_z P\left(r_{\rm ps}^{(0)}\right)}{f\left(r_{\rm ps}^{(0)}\right)}, \tag{3.76}$$

where

$$r_{\rm ps}^{(0)} f'\left(r_{\rm ps}^{(0)}\right) - 2f\left(r_{\rm ps}^{(0)}\right) = 0. \tag{3.77}$$

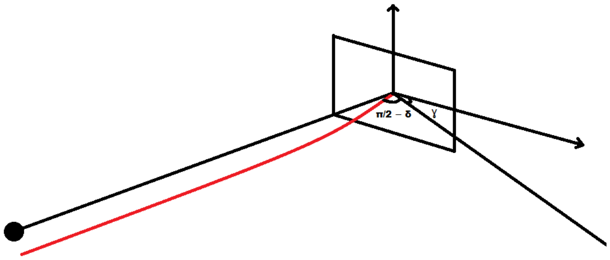

Figure 3.20: Geometry used in the black hole shadow derivation.

With this, similar to the procedure in [68], we consider an observer placed far away from a black hole, with the spherical coordinates ($r = r_0, \theta = \theta_0, \phi = 0$) (without loss of generality). One can imagine this observer receiving a photon moving in the direction $dr/dt > 0$, defined by the angular momentum parameters j^2 and ℓ_z. Unlike our analysis in section 3.2.4, j is no longer necessarily aligned with the z-direction, and instead the two are related via (3.76). From here, we would like to find the angle between the photon's velocity vector and the plane perpendicular to the r-direction at the observer's location. At this point we write the velocity tangent vector as

$$u = -\dot{r}e_r + r_0\dot{\theta}e_\theta + r_0 \sin\theta_0\dot{\phi}e_\phi \tag{3.78}$$

where we use the following orthonormal coordinate system for the observer facing the black hole:

$$e_r = -\partial_r, \quad e_\theta = \frac{\partial_\theta}{r_0}, \quad e_\phi = \frac{\partial_\phi}{r_0 \sin\theta_0}. \tag{3.79}$$

We define $\frac{\pi}{2} - \delta$ to be the angle between the tangent vector and the observer's plane (see figure 3.20), which in general has a component below the x-y plane. γ is then defined to be the angle the projected vector forms with the direction e_ϕ. In doing so it is straightforward to show that

$$\sin\delta = r_0\sqrt{\dot{\theta}^2 + \sin^2\theta_0\dot{\phi}^2}, \quad \cos\gamma = \frac{\sin\theta_0\dot{\phi}}{\sqrt{\dot{\theta}^2 + \sin^2\theta_0\dot{\phi}^2}} \tag{3.80}$$

where we have made the assumption that $\dot{r} << r_0\sqrt{\dot{\theta}^2 + \sin^2\theta_0\dot{\phi}^2}$ since the observer is placed at the limit $r_0 \to \infty$. With this, the tangent vector is effectively re-parameterized:

$$u = -\dot{r}e_r + \sin\delta\left(e_\theta \sin\gamma + e_\phi\cos\gamma\right). \tag{3.81}$$

Invoking equations (3.73) furthermore allows us to express our angular momentum parameters in terms of these angles and the constants describing our observer's location:

$$j = r_0 \sin\delta, \quad \ell_z = r_0 \sin\theta_0 \cos\gamma \sin\delta. \tag{3.82}$$

We know that the black hole shadow is determined by those photons passing arbitrarily close to the photon sphere. We take this into account by using relation (3.76) with (3.82), yielding

$$r_0^2 \sin^2\delta = \frac{\left(r_{\rm ps}^{(0)}\right)^2}{f\left(r_{\rm ps}^{(0)}\right)} + \frac{2a\sin\theta_0 P\left(r_{\rm ps}^{(0)}\right)}{f\left(r_{\rm ps}^{(0)}\right)} \cos\gamma \; r_0 \sin\delta \tag{3.83}$$

which determines the contour $\delta(\gamma)$ of the black hole shadow. Expanding linearly in a, the solution reads

$$r_0 \sin\delta = \frac{r_{\rm ps}^{(0)}}{\sqrt{f\left(r_{\rm ps}^{(0)}\right)}} + \frac{a\sin\theta_0 P\left(r_{\rm ps}^{(0)}\right)}{f\left(r_{\rm ps}^{(0)}\right)} \cos\gamma. \tag{3.84}$$

Finally, since $\delta << 1$ in the large r_0 limit, we can set $sin(\delta) \approx \delta$. Since in the large r_0 limit $R \approx r_0\delta$, we can say

$$R_{sh} \approx \frac{r_{\rm ps}^{(0)}}{\sqrt{f\left(r_{\rm ps}^{(0)}\right)}} + \frac{a\sin\theta_0 P\left(r_{\rm ps}^{(0)}\right)}{f\left(r_{\rm ps}^{(0)}\right)} \cos\gamma. \tag{3.85}$$

Here the re-scaled equation is obtained simply by replacing unbarred symbols with their barred counterparts. When rotational effects vanish the above expression simply describes a circle of radius

$$R_{sh}^{(0)} = \frac{r_{\rm ps}^{(0)}}{\sqrt{f\left(r_{\rm ps}^{(0)}\right)}}. \tag{3.86}$$

The effect of rotation is to offset this image in the x-direction of the observer's plane. The center of the circumference is offset by the amount corresponding to $\gamma = 0$, ie:

$$D_{sh} = a\frac{\sin(\theta_0)P(r_{ps}^{(0)})}{f(r_{ps}^{(0)})}. \tag{3.87}$$

With this it is trivial to plot the contour of the black hole shadow (parameterized by $\gamma : 0 \to 2\pi$), keeping in mind that $x = R_{sh}\text{cos}\gamma$, $y = R_{sh}\text{sin}\gamma$. This is done in the following sections for asymptotically flat, anti-de Sitter, and de Sitter spacetimes.

Asymptotically Flat ($\Lambda = 0$)

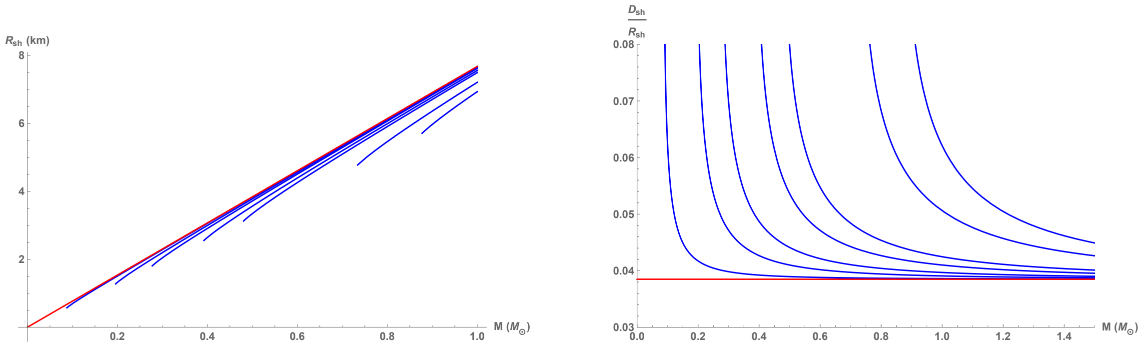

(a) Black hole shadow radius plotted as a function of mass for $\alpha/M_\odot^2 = 0.01$, 0.05, 0.1, 0.2, 0.3, 0.7, 1 (in blue from left to right) against the GR results (red) when $\Lambda = 0$. Here we have fixed $\chi = -0.1$ for comparison with [68], and have also fixed $\theta_0 = \pi/2$.

(b) Ratio D_{sh}/R_{sh} for $\alpha/M_\odot^2 = 0.01$, 0.05, 0.1, 0.2, 0.3, 0.7, 1 (in blue from left to right) against the GR results (red) when $\Lambda = 0$. Here we have fixed $\chi = -0.1$ for comparison with [68], and have also fixed $\theta_0 = \pi/2$.

Figure 3.21: Properties of the black hole shadow when $\Lambda = 0$.

The plots characterizing the properties of the black hole shadow for $\Lambda = 0$ can be seen in figures 3.21a and 3.21b. As we have come to expect by this point in the thesis we see the greatest disagreement with GR near M_{min}, and we see convergence with GR as mass gets large. The contours representing the black hole shadow geometry in this case can be seen in figure 3.22. We notice that as the coupling constant becomes large, the radius of the shadow shrinks and its center is offset as the equations suggest.

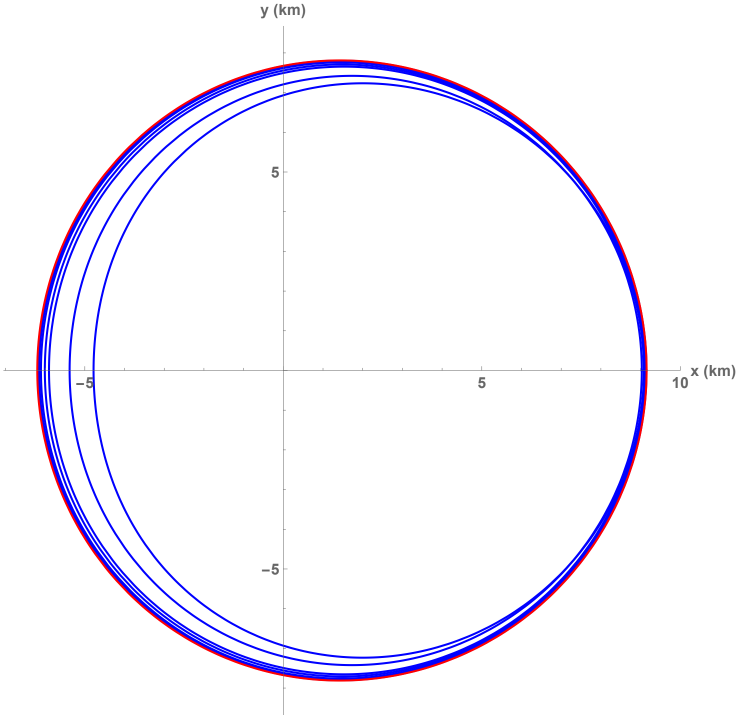

Figure 3.22: Contour of the black hole shadow for $\alpha/M_\odot^2 = 0.01, 0.05, 0.1, 0.2, 0.3, 0.7, 1$ (in blue from left to right) against the GR results (red) when $\Lambda = 0$. Here we have fixed $\chi = -0.5$ for comparison with [68], and have also fixed $\bar{M} = 1$, $\theta_0 = \pi/2$.

AdS ($\Lambda < 0$)

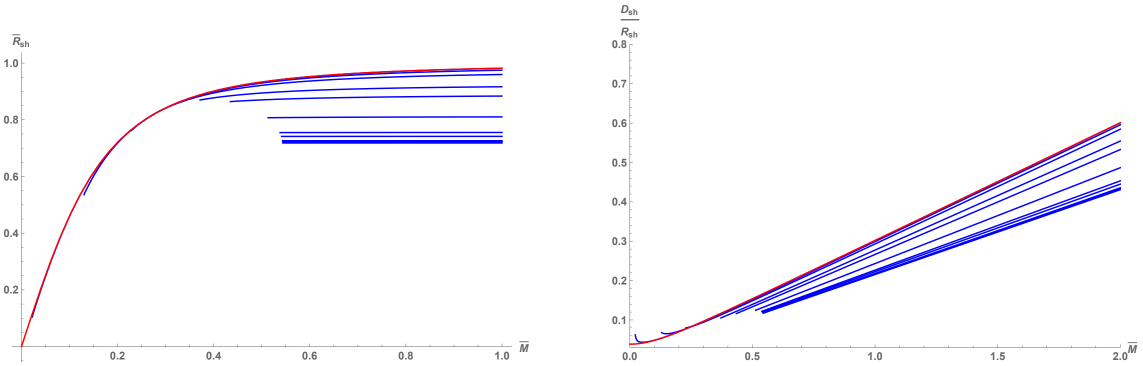

(a) Black hole shadow radius plotted as a function of mass for $\alpha/\alpha_C = 0.002$, 0.066, 0.2, 0.5, 0.666, 0.9, 0.98 0.99, 0.997, 0.998, 0.999 (in blue from left to right) against the GR results (red) in an asymptotically anti-de Sitter spacetime. Here we have fixed $\chi = -0.1$ for comparison with [68], and have also fixed $\theta_0 = \pi/2$.

(b) Ratio D_{sh}/R_{sh} for $\alpha/\alpha_C = 0.002$, 0.066, 0.2, 0.5, 0.666, 0.9, 0.98 0.99, 0.997, 0.998, 0.999 (in blue from left to right) against the GR results (red) in an asymptotically anti-de Sitter spacetime. Here we have fixed $\chi = -0.1$ for comparison with [68], and have also fixed $\theta_0 = \pi/2$.

Figure 3.23: Properties of the black hole shadow when $\Lambda < 0$.

In asymptotically anti-de Sitter space, we once again see very tight agreement with GR for small α, which in the case of the ratio D_{sh}/R_{sh} crosses over the GR result again in the small mass regime. The shadow radius instead touches the GR result before decreasing again. As alpha approaches criticality, the shadow approaches a constant defined only up to the expected minimum mass found in previous sections ($\bar{M}_{min} = 0.544$).

The effect of increasing the 4DGB coupling constant in a universe with a negative cosmological constant is to push the non-looped side of figure 3.24 inwards, toward the origin (ie. shrinking the radius), as in the asymptotically flat case.

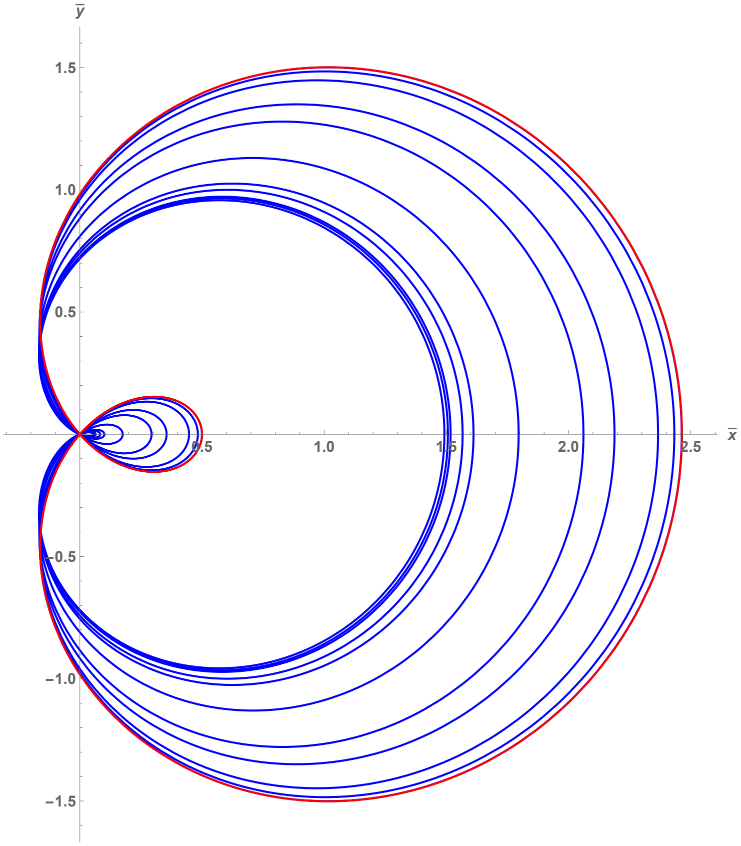

Figure 3.24: Contour of the black hole shadow for $\alpha/\alpha_C = 0.002$, 0.066, 0.2, 0.5, 0.666, 0.9, 0.98 0.99, 0.997, 0.998, 0.999 (in blue from right to left) against the GR results (red) in an asymptotically anti-de Sitter spacetime. Here we have fixed $\chi = -0.5$ for comparison with [68], and have also fixed $\bar{M} = 1$, $\theta_0 = \pi/2$.

dS ($\Lambda > 0$)

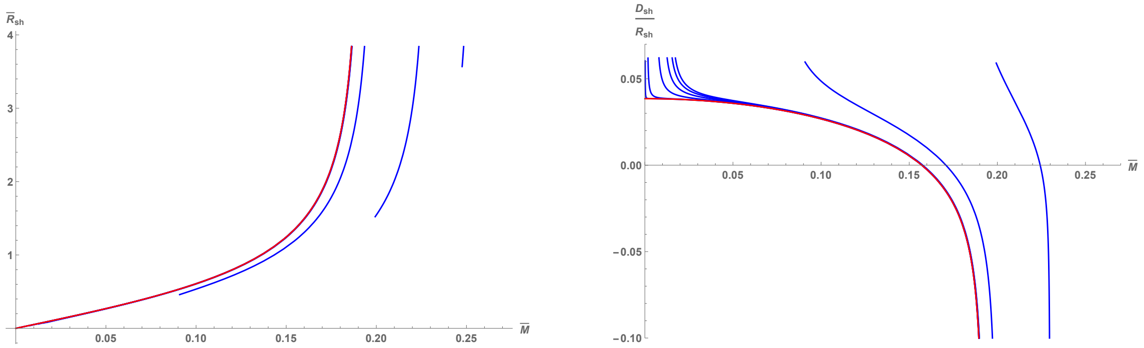

(a) Black hole shadow radius plotted as a function of mass for $\alpha = 0.0001\alpha_T$, $0.01\alpha_T$, $0.2\alpha_T$, $0.5\alpha_T$, $0.75\alpha_T$, $0.9375\alpha_T$, $0.1\alpha_C$, $0.5\alpha_C$, $0.8\alpha_C$ (in blue from left to right) against the GR results (red) in an asymptotically de Sitter spacetime. Here we have fixed $\chi = -0.1$ for comparison with [68], and have also fixed $\theta_0 = \pi/2$.

(b) Ratio D_{sh}/R_{sh} for $\alpha = 0.0001\alpha_T$, $0.01\alpha_T$, $0.2\alpha_T$, $0.5\alpha_T$, $0.75\alpha_T$, $0.9375\alpha_T$, $0.1\alpha_C$, $0.5\alpha_C$, $0.8\alpha_C$ (in blue from left to right) against the GR results (red) in an asymptotically de Sitter spacetime. Here we have fixed $\chi = -0.1$ for comparison with [68], and have also fixed $\theta_0 = \pi/2$.

Figure 3.25: Properties of the black hole shadow when $\Lambda > 0$.

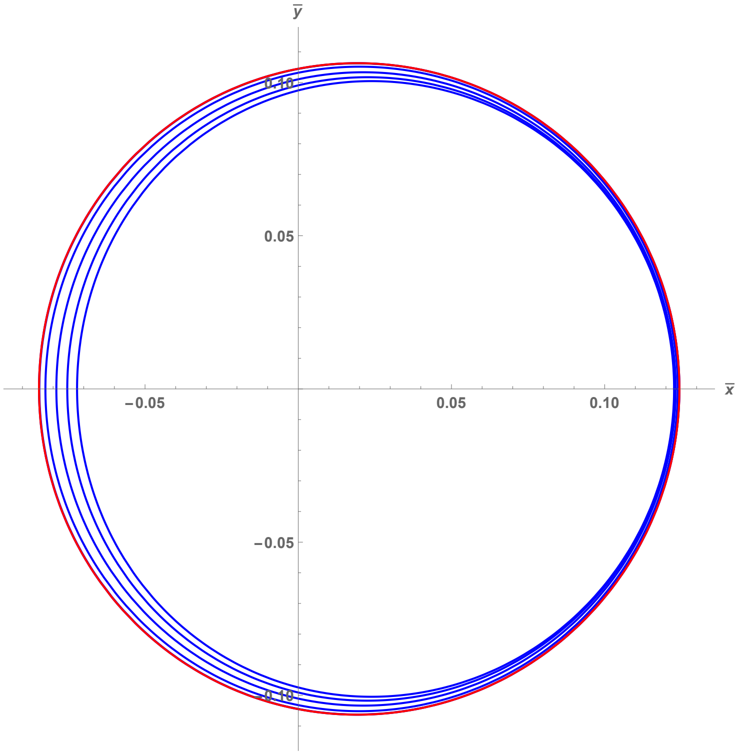

Figure 3.26: Contour of the black hole shadow for $\alpha/\alpha_T = 0.0001$, 0.01, 0.2, 0.5, 0.75, 0.9375 (in blue from left to right) against the GR results (red) in an asymptotically de Sitter spacetime. Here we have fixed $\chi = -0.5$ for comparison with [68], and have also fixed $\bar{M} = 0.02$, $\theta_0 = \pi/2$.

In an asymptotically de Sitter spacetime, as expected, we see strong agreement with the GR curves when α is small, only diverging near $\bar{M}_{\text{min}}$. As $\alpha \to \alpha_C$, we again see the behaviour of the allowed mass region diverging completely (ie. masses which correspond to physical black holes in GR represent naked singularities in 4DGB with large enough α). The effect of increased coupling strength in asymptotically de Sitter spacetimes is very similar to the analogous case when $\Lambda = 0$.

3.3 Summary

In this chapter we investigated slowly rotating solutions to the novel scalar-tensor 4D Gauss-Bonnet theory of gravity for asymptotically flat, de Sitter, and anti-de Sitter spacetimes. These solutions include exact analytical forms for the metric functions $f(r)$ and $p(r)$, black hole horizon structures and angular velocities, radial location/angular momenta of innermost stable circular orbits for massive particles, the location/angular velocities/stabilities associated with the photon spheres, and the geometry of the shadows that characterize black holes in the 4DGB theory of gravity. In most cases, we found solutions that were similar in form to the corresponding GR results, but with the inclusion of enforced minimum mass points (and in the dS case, maximum mass points). Most results tend to converge with general relativity in the large mass regime, although in AdS we instead sometimes see "crossover behaviour" where the 4DGB curves intersect the GR curves before diverging as mass gets larger.

Analytic properties of the solution were also investigated, and it was found that the slowly rotating black hole metric in 4DGB gravity is regular everywhere except $r = 0$ so long as we enforce $\alpha > 0$. Solutions are only considered if they conceal this singular point behind a horizon (further investigation into interior solutions is also required). In de Sitter spacetimes we found that the black hole horizon structure is directly analogous to the charged Nariai solutions from the Reissner-Nordström de Sitter metric. We also found that, given a large enough 4DGB coupling constant, the de Sitter results have no overlap in allowed mass with the GR results. In principle this feature (among others) could be used to set an upper limit on α, using empirical evidence of black holes existing within the allowed GR regime. In practice, since asymptotic flatness is a good approximation in our universe, detecting such deviations from GR is a daunting task with how little the ISCO solutions differ in this case. Slightly more dramatic differences were found for the size of the photon ring in asymptotically flat space, in that we expect them to be appreciably smaller in the 4DGB theory provided the coupling constant is large enough.

A thorough study of black hole shadow geometry suggests that the 4DGB theory will produce rotating black hole shadows very similar to those generated by an Einsteinian black hole, although slightly smaller in diameter. These similarities between the theories elicit mixed emotions. Since GR works so well, in principle any appropriate gravity theory should reproduce most or many of the same results. This feature is also what makes experimental verification difficult due to the extreme precision to measure differences of this order. However, since many of the models outlined here *do* predict unique features for certain small mass black holes, this motivates the search for minimal mass astrophysical black holes with which the 4DGB theory could really be put to the test as an observational competitor to GR.

Chapter 4

Discussion and Future Work

In this thesis we examined the stellar structure and radial stability of charged quark stars under a novel interacting equation of state, and examined slowly rotating black hole solutions in 4 dimensional Einstein-Gauss-Bonnet gravity, with a number of interesting results being uncovered. In the case of charged interacting quark stars, we found that in general a larger charge profile and/or interaction strength λ tends to increase stellar mass and radii. In the case where charge is distributed proportionally to spatial volume, a new exotic stellar structure has been identified with a finite radius and vanishing central pressure. Under this same charge model, stable stellar structures were found at central densities above that which corresponds to maximum mass. With this, a critical value on the charge parameter β was derived below which this structure is not seen. In the case of slowly rotating black hole solutions in the 4DGB theory, we found results for black hole horizons/angular velocity, innermost stable circular orbits, photon sphere parameters, and black hole shadow geometry. Most of these results are similar in form to GR (not predicting some extreme departure in gravitational dynamics), but have enforced minimum (and sometimes maximum) allowed masses, with results that differ most strongly near this critical point.

The outcome of this research can be used in confronting observations of compact stars and black hole structure in novel ways. New astrophysical phenomena related to quark stars and quark matter are likely to emerge in the coming years, which could in principle be used alongside work such as this to put constraints on parameters like the QM interaction strength and effective bag constant. Similarly, amidst a rejuvenated wave of black hole astronomy, independent spin/mass measurements of physical black holes in the slow rotation limit could be used to constrain the 4D Gauss-Bonnet coupling constant with observation.

On a broader scale, investigations into modified gravity theories like this one help us learn more about the properties of HCTs and the role they might play in our universe. While a full picture of quantum gravity remains outside of our reach, many physicists suspect that a more general 4D gravitational action than that derived by Einstein and Hilbert will be necessary in solving the problem of geodesic incompleteness.

Going forward, it would first of all be interesting to combine the two central themes of this thesis - seeing how 4DGB gravitation and/or the introduction of slow rotation could change the behaviour of our novel interacting quark star (particularly since vanishing angular momentum is not a realistic assumption). Furthermore, under general relativity, a number of upper limits have been derived for the rotation parameter a, such as the well-known Kerr limit $\chi \leq 1$ [67] above which the black hole is horizonless, or the limit derived by Dauser et al. [134] which takes X-ray reflection off the accretion disk into account. These limits should be re-derived in the 4D Gauss-Bonnet theory to see if the theoretically allowed spin range differs from that found for GR. Similarly, an upper limit on a for which the slow rotation approximation is valid in the theory would also be useful.

More generally, future work in this field continues to strive for the unification of physical theories from the smallest scales of nature at which we find quarks and electrons, to the grand cosmological scales on which large scale universal structure exists. Whether such a theory is even possible is still an open question, and as always, new results present more questions than they do answers. Future generations of scientists need these grand philosophical questions as a source of guiding light - thankfully, much work remains to be done.

References

[1] Chen Zhang, Michael Gammon, and Robert Mann. Stellar structure and stability of charged interacting quark stars and their scaling behaviour. *Phys. Rev. D.*, 104, 2021.

[2] Albert Einstein. Relativitätsprinzip und die aus demselben gezogenen folgerungen (on the relativity principle and the conclusions drawn from it). *Jahrbuch der Radioaktivität*, 4:411–462, 1907.

[3] Albert Einstein. Über den einfluß der schwerkraft auf die ausbreitung des lichtes. *Annalen der Physik*, 340(10):898–908, 1911.

[4] Albert Einstein. The Field Equations of Gravitation. *Sitzungsber. Preuss. Akad. Wiss. Berlin (Math. Phys.)*, pages 844–847, 1915.

[5] Albert Einstein. Erklärung der Perihelbewegung des Merkur aus der allgemeinen Relativitätstheorie (Explanation of the Perihelion Motion of Mercury from the General Theory of Relativity) . *Preussische Akademie der Wissenschaften, Sitzungsberichte*, page 831–839, 1915.

[6] Albert Einstein. Näherungsweise Integration der Feldgleichungen der Gravitation. *Sitzungsberichte der Königlich Preußischen Akademie der Wissenschaften (Berlin*, pages 688–696, January 1916.

[7] W. W. Campbell and R. Trumpler. Observations on the deflection of light in passing through the sun's gravitational field, made during the total solar eclipse of september 21, 1923. *Publications of the Astronomical Society of the Pacific*, 35(205):158–163, 1923.

[8] F. W. Dyson, A. S. Eddington, and C. Davidson. A determination of the deflection of light by the sun's gravitational field, from observations made at the total eclipse

of may 29, 1919. *Philosophical Transactions of the Royal Society of London. Series A, Containing Papers of a Mathematical or Physical Character*, 220:291–333, 1920.

[9] B. P. Abbott et al. Observation of gravitational waves from a binary black hole merger. *Physical Review Letters*, 116(6), Feb 2016.

[10] Robert M. Wald. *General Relativity.* The University of Chicago Press, 1984.

[11] W. Baade and F. Zwicky. Remarks on super-novae and cosmic rays. *Phys. Rev.*, 46:76–77, Jul 1934.

[12] J. R. Oppenheimer and G. M. Volkoff. On massive neutron cores. *Phys. Rev.*, 55:374–381, Feb 1939.

[13] Richard C. Tolman. Static solutions of einstein's field equations for spheres of fluid. *Phys. Rev.*, 55:364–373, Feb 1939.

[14] A Sissakian, Alexander Sorin, V. Kekelidze, Igor Meshkov, Alexander Kovalenko, G. Trubnikov, N.N. Agapov, Vladimir Aleksandrov, Oleg Brovko, Andrey Butenko, E Donets, Evgeny Donets, Alexey Eliseev, A Govorov, I Issinsky, V Kalagin, G Khodzhibagiyan, V Karpinsky, V Kobets, and Vyacheslav Zhabitsky. Progress of the nica project. *Proceedings of Science*, 07 2009.

[15] James M. Lattimer. Introduction to neutron stars. In *Exotic Nuclei and Nuclear/Particle Astrophysics (V) From Nuclei to Stars: Carpathian Summer School of Physics 2014*, volume 1645 of *American Institute of Physics Conference Series*, pages 61–78, February 2015.

[16] Norman K. Glendenning. *Compact Stars.* 1996.

[17] Feryal Özel, Dimitrios Psaltis, Ramesh Narayan, and Antonio Santos Villarreal. On the Mass Distribution and Birth Masses of Neutron Stars. *APJ*, 757(1):55, 2012.

[18] N Chamel, P Haensel, J Zdunik, and A Fantina. On the maximum mass of neutron stars. *Int. J. Mod. Phys.*

[19] T Jayasinghe, K Z Stanek, Todd A Thompson, C S Kochanek, D M Rowan, P J Vallely, K G Strassmeier, M Weber, J T Hinkle, F-J Hambsch, D V Martin, J L Prieto, T Pessi, D Huber, K Auchettl, L A Lopez, I Ilyin, C Badenes, A W Howard, H Isaacson, and S J Murphy. A unicorn in monoceros: the 3 Msolar dark companion to the bright, nearby red giant V723 Mon is a non-interacting, mass-gap black hole

candidate. *Monthly Notices of the Royal Astronomical Society*, 504(2):2577–2602, 05 2021.

[20] Roman Pasechnik and Michal Šumbera. Phenomenological review on quark–gluon plasma: Concepts vs. observations. *Universe*, 3(1), 2017.

[21] Jes Madsen. Physics and astrophysics of strange quark matter. In Jean Cleymans, Hendrik B. Geyer, and Frederik G. Scholtz, editors, *Hadrons in Dense Matter and Hadrosynthesis*, pages 162–203, Berlin, Heidelberg, 1999. Springer Berlin Heidelberg.

[22] H WEYL. Electricity and gravitation. *Nature (London)*, 106(2677):800–802, 1921.

[23] A. S. Eddington. A generalisation of weyl's theory of the electromagnetic and gravitational fields. *Proceedings of the Royal Society of London. Series A, Containing Papers of a Mathematical and Physical Character*, 99(697):104–122, 1921.

[24] J. Ahmed et al. *Quintessential Quartic Quasi-topological Quartet*, volume 134. 2017.

[25] P. Bueno P. Cano. Einsteinian cubic gravity. *Phys. Rev. D*, 94, 2016.

[26] D. Lovelock. The einstein tensor and its generalizations. *Journal of Mathematical Physics*, 12, 1971.

[27] P. Bueno et al. (generalized) quasi-topological gravities at all orders. *Classical and Quantum Gravity*, 37, 2019.

[28] M. Poshteh R. Mann. Gravitational lensing by black holes in einsteinian cubic gravity. *Phys. Rev. D*, 99, 2019.

[29] Drazen Glavan and Chunshan Lin. Einstein-gauss-bonnet gravity in four-dimensional spacetime. *Physical Review Letters*, 124(8), Feb 2020.

[30] Arun Kumar, Rahul Kumar Walia, and Sushant G. Ghosh. Bardeen black holes in the regularized 4d einstein gauss bonnet gravity. *Universe*, 8(4):232, apr 2022.

[31] Pedro G.S. Fernandes. Charged black holes in AdS spaces in 4d einstein gauss-bonnet gravity. *Physics Letters B*, 805:135468, jun 2020.

[32] Rahul Kumar and Sushant G. Ghosh. Rotating black holes in 4d einstein-gauss-bonnet gravity and its shadow. *Journal of Cosmology and Astroparticle Physics*, 2020(07):053–053, jul 2020.

[33] Arun Kumar, Dharmanand Baboolal, and Sushant G. Ghosh. Nonsingular black holes in 4d einstein–gauss–bonnet gravity. *Universe*, 8(4):244, apr 2022.

[34] Shou-Long Li, Puxun Wu, and Hongwei Yu. Stability of the einstein static universe in $4d$ gauss-bonnet gravity, 2020.

[35] Tsutomu Kobayashi. Effective scalar-tensor description of regularized lovelock gravity in four dimensions. *Journal of Cosmology and Astroparticle Physics*, 2020(07):013–013, jul 2020.

[36] Daniela D. Doneva and Stoytcho S. Yazadjiev. Relativistic stars in 4d einstein-gauss-bonnet gravity. *Journal of Cosmology and Astroparticle Physics*, 2021(05):024, may 2021.

[37] C. Charmousis, A. Lehébel, E. Smyrniotis, and N. Stergioulas. Astrophysical constraints on compact objects in 4d einstein-gauss-bonnet gravity. *Journal of Cosmology and Astroparticle Physics*, 2022(02):033, Feb 2022.

[38] Sushant G. Ghosh and Sunil D. Maharaj. Radiating black holes in the novel 4d einstein-gauss-bonnet gravity. 2020.

[39] Daniele Malafarina, Bobir Toshmatov, and Naresh Dadhich. Dust collapse in 4d einstein–gauss–bonnet gravity. *Physics of the Dark Universe*, 30:100598, dec 2020.

[40] Metin Gürses, Tahsin Çağrı Şişman, and Bayram Tekin. Is there a novel einstein–gauss–bonnet theory in four dimensions? *The European Physical Journal C*, 80(7), jul 2020.

[41] Wen-Yuan Ai. A note on the novel 4d einstein–gauss–bonnet gravity. *Communications in Theoretical Physics*, 72(9):095402, aug 2020.

[42] Fu-Wen Shu. Vacua in novel 4d einstein-gauss-bonnet gravity: Pathology and instability? *Physics Letters B*, 811:135907, dec 2020.

[43] R. Hennigar et al. On taking the d → 4 limit of gauss -bonnet gravity: Theory and solutions. *Journal of High Energy Physics*, 27, 2020.

[44] Pedro G. S. Fernandes, Pedro Carrilho, Timothy Clifton, and David J. Mulryne. Derivation of Regularized Field Equations for the Einstein-Gauss-Bonnet Theory in Four Dimensions. *Phys. Rev. D*, 102(2):024025, 2020.

[45] Robert B. Mann and S. F. Ross. The D —> 2 limit of general relativity. *Class. Quant. Grav.*, 10:1405–1408, 1993.

[46] H. Lu and Yi Pang. Horndeski gravity as $D \to 4$ limit of Gauss-Bonnet. *Phys. Lett. B*, 809:135717, 2020.

[47] Gregory Walter Horndeski. Second-order scalar-tensor field equations in a four-dimensional space. *Int. J. Theor. Phys.*, 10:363–384, 1974.

[48] Timothy Clifton, Pedro Carrilho, Pedro G. S. Fernandes, and David J. Mulryne. Observational Constraints on the Regularized 4D Einstein-Gauss-Bonnet Theory of Gravity. *Phys. Rev. D*, 102(8):084005, 2020.

[49] Pedro G. S. Fernandes, Pedro Carrilho, Timothy Clifton, and David J. Mulryne. The 4D Einstein–Gauss–Bonnet theory of gravity: a review. *Class. Quant. Grav.*, 39(6):063001, 2022.

[50] Uma Papnoi and Farruh Atamurotov. Rotating charged black hole in $4d$ einstein-gauss-bonnet gravity: Photon motion and its shadow. 2021.

[51] Mohaddese Heydari-Fard, Malihe Heydari-Fard, and Hamid Reza Sepangi. Thin accretion disks around rotating black holes in 4d einstein–gauss–bonnet gravity. *The European Physical Journal C*, 81(5), may 2021.

[52] Shao-Wen Wei and Yu-Xiao Liu. Testing the nature of gauss-bonnet gravity by four-dimensional rotating black hole shadow, 2020.

[53] Sean Carroll. *Spacetime and Geometry: An Introduction to General Relativity.* Benjamin Cummings, 2003.

[54] Svend Erik Rugh and Henrik Zinkernagel. The quantum vacuum and the cosmological constant problem. 2000.

[55] Edwin Hubble. A relation between distance and radial velocity among extra-galactic nebulae. *Proceedings of the National Academy of Sciences*, 15(3):168–173, 1929.

[56] Adam G. Riess, Alexei V. Filippenko, Peter Challis, Alejandro Clocchiatti, Alan Diercks, Peter M. Garnavich, Ron L. Gilliland, Craig J. Hogan, Saurabh Jha, Robert P. Kirshner, B. Leibundgut, M. M. Phillips, David Reiss, Brian P. Schmidt, Robert A. Schommer, R. Chris Smith, J. Spyromilio, Christopher Stubbs, Nicholas B. Suntzeff, and John Tonry. Observational evidence from supernovae for an accelerating universe and a cosmological constant. *The Astronomical Journal*, 116(3):1009–1038, sep 1998.

[57] Ronald J. Adler, Brendan Casey, and Ovid C. Jacob. Vacuum catastrophe: An elementary exposition of the cosmological constant problem. *American Journal of Physics*, 63(7):620–626, 1995.

[58] M. P. Hobson, G. P. Efstathiou, and A. N. Lasenby. *General relativity: An introduction for physicists.* 2006.

[59] G. W. Gibbons and S. W. Hawking. Action integrals and partition functions in quantum gravity. *Phys. Rev. D*, 15:2752–2756, May 1977.

[60] K. Schwarzschild. On the gravitational field of a mass point according to einstein's theory. 1916.

[61] Johannes Droste. *Het zwaarterkrachtsveld van een of meer lichamen volgens de theorie van Einstein.* EJ Brill, 1916.

[62] George David Birkhoff and Rudolph Ernest Langer. *Relativity and modern physics.* 1923.

[63] H. Reissner. Über die Eigengravitation des elektrischen Feldes nach der Einsteinschen Theorie, January 1916.

[64] G. Nordström. On the Energy of the Gravitation field in Einstein's Theory. *Koninklijke Nederlandse Akademie van Wetenschappen Proceedings Series B Physical Sciences*, 20:1238–1245, January 1918.

[65] Hermann Weyl. Zur gravitationstheorie, January 1917.

[66] George Barker Jeffery and Louis Napoleon George Filon. The field of an electron on einstein’s theory of gravitation. *Proceedings of the Royal Society of London. Series A, Containing Papers of a Mathematical and Physical Character*, 99(697):123–134, 1921.

[67] Roy P. Kerr. Gravitational field of a spinning mass as an example of algebraically special metrics. *Phys. Rev. Lett.*, 11:237–238, Sep 1963.

[68] C. Adair et al. Slowly rotating black holes in einsteinian cubic gravity. *Phys. Rev. D*, 102, 2020.

[69] Subharthi Ray, Aquino L Espindola, Manuel Malheiro, José PS Lemos, and Vilson T Zanchin. Electrically charged compact stars and formation of charged black holes. *Physical Review D*, 68(8):084004, 2003.

[70] Subharthi et al Ray. Charged polytropic compact stars. *Brazilian Journal of Physics.*

[71] M Malheiro, S Ray, and Vilson T Zanchin. Electrically charged neutron stars. *Proceedings of the International Workshop on Strong Magnetic Fields and Neutron Stars*, pages 253–270, 2003.

[72] S Rosseland. Electrical state of a star. *Monthly Notices of the Royal Astronomical Society*, 84:720–728, 1924.

[73] David R. Williams. Sun fact sheet. `https://nssdc.gsfc.nasa.gov/planetary/factsheet/sunfact.html`.

[74] Subharthi Ray, Manuel Malheiro, Jose' P. S. Lemos, and Vilson T. Zanchin. Electrically charged compact stars, 2006.

[75] J Bally and ER Harrison. The electrically polarized universe. *The Astrophysical Journal*, 220:743, 1978.

[76] Maneul Malheiro, Rodrigo Picano, Subharthi Ray, JOSÉ P. S Lemos, and VILSON T Zanchin. Of charged stars and charged black holes. *International journal of modern physics. D, Gravitation, astrophysics, cosmology*, 13(7):1375–1379, 2004.

[77] Sakhile Ndebele. Charge distribution in neutron stars. Master's thesis, University of KwaZulu-Natal, 2017.

[78] Murray Gell-Mann. A Schematic Model of Baryons and Mesons. *Phys. Lett.*, 8:214–215, 1964.

[79] G. Zweig. *An SU(3) model for strong interaction symmetry and its breaking. Version 2*, pages 22–101. 2 1964.

[80] David J. Gross and Frank Wilczek. Ultraviolet behavior of non-abelian gauge theories. *Phys. Rev. Lett.*, 30:1343–1346, Jun 1973.

[81] Bob Holdom, Jing Ren, and Chen Zhang. Quark matter may not be strange. *Phys. Rev. Lett.*, 120:222001, May 2018.

[82] A. R. Bodmer. Collapsed nuclei. *Physical review. D, Particles and fields*, 4(6):1601–1606, 1971.

[83] E Witten. Cosmic separation of phases. *Physical review. D, Particles and fields*, 30(2):272–285, 1984.

[84] H. Terazawa, Y. Chikashige, and K. Akama. Temporary freedom and asymptotic catastrophe of lepton and quark interactions. *Progress of theoretical physics*, 61(5):1515–1520, 1979.

[85] F. Weber, O. Hamil, K. Mimura, and R. Negreiros. From crust to core: A brief review of quark matter in neutron stars. *Int. J. Mod. Phys. D*, 19:1427–1436, 2010.

[86] S. Schettler, M. T. Boeckel, and J. Schaffner-Bielich. Detecting quark matter in the early universe by gravitational waves. In *Exploring Fundamental Issues in Nuclear Physics*. World Scientific, Jan 2012.

[87] A. Chodos, R. L. Jaffe, K. Johnson, and C. B. Thorn. Baryon structure in the bag theory. *Phys. Rev. D*, 10:2599–2604, Oct 1974.

[88] Kenneth Johnson et al. The mit bag model. *Acta Phys. Pol. B*, 6(12):8, 1975.

[89] Tanushree Chowdhury and Dipankar Bhattacharya. Equation of state and the structure of compact stars.

[90] G. P. Horedt. *Polytropes : applications in astrophysics and related fields / by G.P. Horedt.* Astrophysics and Space Science Library, 306. Kluwer Academic, Dordrecht, Netherlands ;, 1st ed. 2004. edition, 2004.

[91] Chen Zhang and Robert B. Mann. Unified interacting quark matter and its astrophysical implications. *Phys. Rev. D*, 103:063018, Mar 2021.

[92] Edward Farhi and R. L. Jaffe. Strange matter. *Phys. Rev. D*, 30:2379–2390, Dec 1984.

[93] Eduardo S. Fraga, Robert D. Pisarski, and Jürgen Schaffner-Bielich. Small, dense quark stars from perturbative QCD. *Physical Review D*, 63(12), may 2001.

[94] Eduardo S. Fraga, Aleksi Kurkela, and Aleksi Vuorinen. INTERACTING QUARK MATTER EQUATION OF STATE FOR COMPACT STARS. *The Astrophysical Journal*, 781(2):L25, jan 2014.

[95] Mark Alford, Krishna Rajagopal, and Frank Wilczek. Color-flavor locking and chiral symmetry breaking in high density QCD. *Nuclear Physics B*, 537(1-3):443–458, jan 1999.

[96] Krishna Rajagopal and Frank Wilczek. Enforced electrical neutrality of the color-flavor locked phase. *Physical Review Letters*, 86(16):3492–3495, apr 2001.

[97] G. Lugones and J. E. Horvath. Color-flavor locked strange matter. *Physical Review D*, 66(7), oct 2002.

[98] S. Chandrasekhar. The Dynamical Instability of Gaseous Masses Approaching the Schwarzschild Limit in General Relativity. , 140:417, August 1964.

[99] A. Brillante and I. N. Mishustin. Radial oscillations of neutral and charged hybrid stars. *EPL (Europhysics Letters)*, 105(3):39001, Feb 2014.

[100] James M. Bardeen, Kip S. Thorne, and David W. Meltzer. A Catalogue of Methods for Studying the Normal Modes of Radial Pulsation of General-Relativistic Stellar Models. , 145:505, August 1966.

[101] V. P. Gonçalves and L. Lazzari. Electrically charged strange stars with an interacting quark matter equation of state. *Physical Review D*, 102(3), aug 2020.

[102] José D. V. Arbañil and M. Malheiro. Equilibrium and stability of charged strange quark stars. *Physical Review D*, 92(8), oct 2015.

[103] N. Andersson. A gravitational-wave perspective on neutron-star seismology, 2021.

[104] V. Sagun, G. Panotopoulos, and I. Lopes. Asteroseismology: Radial oscillations of neutron stars with realistic equation of state. *Physical Review D*, 101(6), mar 2020.

[105] Cecilia Chirenti, Roman Gold, and M. Coleman Miller. Gravitational waves from f-modes excited by the inspiral of highly eccentric neutron star binaries. *The Astrophysical Journal*, 837(1):67, mar 2017.

[106] Lucia M. Franco, Bennett Link, and Richard I. Epstein. Quaking neutron stars. *The Astrophysical Journal*, 543(2):987–994, nov 2000.

[107] Tanja Hinderer, Andrea Taracchini, Francois Foucart, Alessandra Buonanno, Jan Steinhoff, Matthew Duez, Lawrence E. Kidder, Harald P. Pfeiffer, Mark A. Scheel, Bela Szilagyi, Kenta Hotokezaka, Koutarou Kyutoku, Masaru Shibata, and Cory W. Carpenter. Effects of neutron-star dynamic tides on gravitational waveforms within the effective-one-body approach. *Phys. Rev. Lett.*, 116:181101, May 2016.

[108] David Tsang, Jocelyn S. Read, Tanja Hinderer, Anthony L. Piro, and Ruxandra Bondarescu. Resonant shattering of neutron star crusts. *Phys. Rev. Lett.*, 108:011102, Jan 2012.

[109] David Lovelock. Divergence-free tensorial concomitants. *aequationes mathematicae*, 2:394–395, 1969.

[110] Robert C. Myers and Brandon Robinson. Black holes in quasi-topological gravity. *Journal of High Energy Physics*, 2010(8), aug 2010.

[111] Julio Oliva and Sourya Ray. A new cubic theory of gravity in five dimensions: black hole, birkhoff's theorem and ic/i -function. *Classical and Quantum Gravity*, 27(22):225002, oct 2010.

[112] Pablo Bueno, Pablo A. Cano, Javier Moreno, and Ángel Murcia. All higher-curvature gravities as generalized quasi-topological gravities. *Journal of High Energy Physics*, 2019(11), nov 2019.

[113] E. Cartan. Sur les équations de la gravitation d'einstein. *Journal de Mathématiques Pures et Appliquées*, 1:141–204, 1922.

[114] A Mardones and J Zanelli. Lovelock-cartan theory of gravity. *Classical and Quantum Gravity*, 8(8):1545–1558, aug 1991.

[115] Takashi Torii and Hisa aki Shinkai. mml:math xmlns:mml="http://www.w3.org/1998/math/MathML" display="inline"mml:min/mml:mimml:mo/mml:momml:mn1/mml:mn/mml:mathformalism in einstein-gauss-bonnet gravity. *Physical Review D*, 78(8), oct 2008.

[116] Lowell S. Brown. Stress-tensor trace anomaly in a gravitational metric: Scalar fields. *Phys. Rev. D*, 15:1469–1483, Mar 1977.

[117] Cornelius Lanczos. A remarkable property of the riemann-christoffel tensor in four dimensions. *Annals of Mathematics*, 39:842–850, 1938.

[118] Rudolf Bach. Zur weylschen relativitätstheorie und der weylschen erweiterung des krümmungstensorbegriffs. *Mathematische Zeitschrift*, 9:110–135, 1921.

[119] Yu-Peng Zhang, Shao-Wen Wei, and Yu-Xiao Liu. Spinning test particle in four-dimensional einstein gauss bonnet black holes. *Universe*, 6(8):103, jul 2020.

[120] Jing Ren and Chen Zhang. Quantum nucleation of up-down quark matter and astrophysical implications. *Physical Review D*, 102(8), oct 2020.

[121] Chen Zhang. Gravitational wave echoes from interacting quark stars. *Physical Review D*, 104(8), oct 2021.

[122] Jacob D Bekenstein. Hydrostatic equilibrium and gravitational collapse of relativistic charged fluid balls. *Physical Review D*, 4(8):2185, 1971.

[123] Rodrigo Picanç o Negreiros, Fridolin Weber, Manuel Malheiro, and Vladimir Usov. Electrically charged strange quark stars. *Physical Review D*, 80(8), oct 2009.

[124] Grigoris Panotopoulos and Ángel Rincón. Electrically charged strange quark stars with a non-linear equation-of-state. *Eur. Phys. J. C*, 79(6):524, 2019.

[125] Grigoris Panotopoulos, Takol Tangphati, and Ayan Banerjee. Electrically charged compact stars with an interacting quark equation of state. *Chinese Journal of Physics*, 77:1682–1690, jun 2022.

[126] M. K. Jasim, Anirudh Pradhan, Ayan Banerjee, Takol Tangphati, and Grigoris Panotopoulos. Structural properties of charged compact stars with color-flavor-locked quarks matter. *Modern Physics Letters A*, 36(32), oct 2021.

[127] R. B. Mann and Simon F. Ross. Cosmological production of charged black hole pairs. *Physical Review D*, 52(4):2254–2265, aug 1995.

[128] S. W. Hawking and Simon F. Ross. Duality between electric and magnetic black holes. *Physical Review D*, 52(10):5865–5876, nov 1995.

[129] Raphael Bousso. Charged nariai black holes with a dilaton. *Rev. D*, 55:361–4, 1997.

[130] Pablo A. Cano and Alejandro Ruipérez. Leading higher-derivative corrections to kerr geometry. *Journal of High Energy Physics*, 2019(5), may 2019.

[131] Bahram Mashhoon. Stability of charged rotating black holes in the eikonal approximation. *Phys. Rev. D*, 31:290–293, Jan 1985.

[132] Vitor Cardoso, Alex S. Miranda, Emanuele Berti, Helvi Witek, and Vilson T. Zanchin. Geodesic stability, lyapunov exponents, and quasinormal modes. *Phys. Rev. D*, 79:064016, Mar 2009.

[133] Shobhit Giri, Hemwati Nandan, Lokesh Kumar Joshi, and Sunil D. Maharaj. Geodesic stability and quasinormal modes of non-commutative schwarzschild black hole employing lyapunov exponent. *The European Physical Journal Plus*, 137(2), jan 2022.

[134] T. Dauser, J. Garcia, M. L. Parker, A. C. Fabian, and J. Wilms. The role of the reflection fraction in constraining black hole spin. *Mon. Not. Roy. Astron. Soc.*, 444:100, 2014.